

Nano-photonic Light Trapping In Thin Film Solar Cells

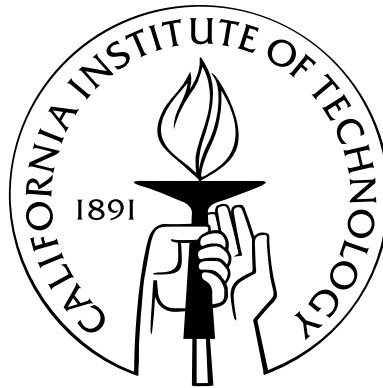
Thesis by

Dennis M. Callahan Jr.

In Partial Fulfillment of the Requirements

for the Degree of

Doctor of Philosophy



California Institute of Technology

Pasadena, California

2015

(Defended October 1, 2014)

© 2015

Dennis M. Callahan Jr.

All Rights Reserved

for Zhaoxia and little Dylan

Acknowledgements

I would first like to thank my thesis advisor, Harry Atwater, for taking a chance on a kid who took a chance on a school he never thought he could get into. Over the years, his mentorship and constant insight have been incredibly helpful and inspiring. I would like to thank him for creating an environment where an incoming student with limited scientific knowledge can quickly and efficiently learn and absorb so much about many different areas of research.

I would also like to thank Professors Oskar Painter, Julia Greer, Andrei Faraon and Bill Johnson for serving on my candidacy and thesis committees. I truly appreciate their time and it has been an honor to cross paths with them.

I would like to acknowledge and thank all of the students and post-docs that I have worked with, learned from, and become friends with over the years. I would like to thank Dr. Jeremy Munday for helping me get started on the thin-film GaAs project and for all the time we spent in front of the blackboard thinking about the light trapping limit. Jeremy was also a good friend and I am fortunate to have been assigned to work with him when I started full-time research in the group. I'd like to thank Dr. Jonathan Grandidier for working closely with me for a couple years on the nano sphere solar cell project and for letting me drive the Mustang to MRS in San Francisco. I'd like to thank Dr. Deirdre O'Carroll, the best "Good Cop, Bad Cop" partner one could ask for at MRS poster sessions. I would also like to thank Deirdre for humoring my ideas, trying to (unsuccessfully) make the world's first Ultrafast Deep Subwavelength Ultra-High Q-Switched Amplifying Nanorod Quantum

Generating Hetero-Metamaterial Lasing Spasing Plasmonic FORABISER, and for the coffee. I'd like to thank Ragip Pala for working on the thin-film GaAs project with me, helping with last-minute EQE measurements, and for always keeping a lighthearted atmosphere. I'd like to thank Dr. Marina Leite for sharing her expertise about semiconductor research with me. I'd like to thank Dr. Koray Aydin for humoring my ideas about metamaterials and for helping me get started with FDTD simulations. I'd like to thank Dr. Eyal Feigenbaum for teaching me about aspects of optics I had never thought about before. I'd like to thank Dr. Victor Brar for talking about physics, hanging out at the Rath, playing tennis, talking about basketball, and for the single-malt Scotch.

I'd like to thank Raymond Weitekamp for being a good friend, inviting me to his shows, and participating in the short-lived generative art club. Jim Fakonas for being a good friend, lunchtime philosophy discussions and for knowing how to play all my favorite Rolling Stones songs. Ryan Briggs for teaching me about photonics and Purcell Factor. Stan Burgos for cigarettes and deep discussions among wandering homeless men on the streets of San Francisco. I'd like to thank everyone who came to meetings of the short-lived spontaneous emission club. I'd like to thank the spontaneous emission group from my first group retreat that made it so much fun and for trying to (unsuccessfully) get the term Wanteca into the nano-photonics vernacular (that's a hybrid waveguide-antenna-cavity). I'd like to thank Colton Bukowsky for all the time and help he has recently given with electron beam lithography and reactive ion etching. For a period, I was working in collaboration with Albert Polman's group at AMOLF in the Netherlands and I thank them for their contributions, particularly Piero Spinelli.

I'd like to thank the talented undergraduate SURF students I had the privilege of mentoring over various summers including Reggie Wilcox, Clare Chen, Prateek Mantri and Kelsey Whitesell. Kelsey also returned to Caltech for a Masters degree

and I thank her for putting in so much time on the photonic crystal project and for being a good friend.

I'd especially like to thank the Atwater group bluegrass band, Muskrat Water. This includes Matt "Bayou" Escarra, Dan "Moonshine" Turner Evans, Amanda "Thunderbird" Shing, Ana "Appalachia" Brown, and Cris "Huckleberry" Flowers. I reckon jamming with these folks was some of the most fun I had at this here school.

I'd also like to thank Yulia Tolstova for introducing me to The Mountain Goats, The Tiger Lillies and for suggesting I watch The Double Life Of Vernonique by Krzysztof Kieslowski. I'd like to thank Raymond Wietekamp for introducing me to CocoRosie, Bibio and Flying Lotus. I'd like to thank Hal Emmer for introducing me to The Angus And Julia Stone, Carissa Eisler for suggesting I listen to glitch music, and all of Muskrat Water for introducing me to Old Crow Medicine Show.

I'd like to thank everyone who contributed to the LMI-EFRC video contest including Raymond Weitekamp, Jonathan Grandidier, Emily Kosten, Eyal Feigenbaum, Stanley Burgos and Koray Aydin. I'd like to thank Professor Michael Roukes, Mary Sikora and everyone involved in TEDxCaltech, Feynman's Vision: The Next 50 Years. I'd like to thank everyone involved in Caltech's Art of Science program for creating such a great program and for exhibiting my submissions.

I would like to thank all of my office mates over the years including Amir Safavi-Naeni, Lisa Mauger, Jeff Hill, Alex Krause, Mike Deceglie, Victor Brar, Emily Kosten, and Matt Sheldon. I'd also like to thank the group's administrative assistants April Neidholdt, Tiffany Kimoto, Jennifer Blankenship, and Lyra Haas.

I would also like to deeply acknowledge Bob Dylan, Tom Waits, David Bowie, Brian Eno, Neko Case and Ryan Adams for providing the bulk of the soundtrack to the last 6 years. I sincerely think I could not have done it without them.

I would like to thank my family for always believing in me and for letting me move 3,000 miles away from home without protest. Lastly and most importantly I would

like to thank my wife, Zhaoxia, for so much more than can be described with words at the end of a paragraph in a thesis. Closing out this chapter of my life, you are the only reason I've done any of this.

Dennis M. Callahan Jr.

September 2014

Los Angeles, CA

Abstract

Over the last several decades there have been significant advances in the study and understanding of light behavior in nanoscale geometries. Entire fields such as those based on photonic crystals, plasmonics and metamaterials have been developed, accelerating the growth of knowledge related to nanoscale light manipulation. Coupled with recent interest in cheap, reliable renewable energy, a new field has blossomed, that of nanophotonic solar cells.

In this thesis, we examine important properties of thin-film solar cells from a nanophotonics perspective. We identify key differences between nanophotonic devices and traditional, thick solar cells. We propose a new way of understanding and describing limits to light trapping and show that certain nanophotonic solar cell designs can have light trapping limits above the so called ray-optic or ergodic limit. We propose that a necessary requisite to exceed the traditional light trapping limit is that the active region of the solar cell must possess a local density of optical states (LDOS) higher than that of the corresponding, bulk material. Additionally, we show that in addition to having an increased density of states, the absorber must have an appropriate incoupling mechanism to transfer light from free space into the optical modes of the device. We outline a portfolio of new solar cell designs that have potential to exceed the traditional light trapping limit and numerically validate our predictions for select cases.

We emphasize the importance of thinking about light trapping in terms of maximizing the optical modes of the device and efficiently coupling light into them from

free space. To further explore these two concepts, we optimize patterns of superlattices of air holes in thin slabs of Si and show that by adding a roughened incoupling layer the total absorbed current can be increased synergistically. We suggest that addition of a random scattering surface to a periodic patterning can increase incoupling by lifting the constraint of selective mode occupation associated with periodic systems.

Lastly, through experiment and simulation, we investigate a potential high efficiency solar cell architecture that can be improved with the nanophotonic light trapping concepts described in this thesis. Optically thin GaAs solar cells are prepared by the epitaxial liftoff process by removal from their growth substrate and addition of a metallic back reflector. A process of depositing large area nano patterns on the surface of the cells is developed using nano imprint lithography and implemented on the thin GaAs cells.

Contents

Acknowledgements	iv
Abstract	viii
1 Introduction	5
1.1 Rise Of Nanophotonics	6
1.2 Solar Cell Fundamentals	6
1.3 Current State Of The Art Solar Cells	10
1.4 Why Thin Solar Cells?	10
2 Light Trapping In Thin Film Solar Cells	13
2.1 Single Pass Absorption	13
2.2 Modes Of A Slab	15
2.3 Accessing Trapped Modes	18
2.4 The Ray Optic Light Trapping Limit	20
3 Light Trapping Beyond The Ray Optic Limit	23
3.1 Condition for Exceeding The Ray Optic Limit	25
3.2 Recovering The Ray Optic Limit	28
3.3 Nanophotonic Solar Cell Designs For Exceeding The Ray Optic Light Trapping Limit	29
3.4 What Is The New Limit?	35
3.5 Numerical Demonstration Of Exceeding The Ray Optic Limit	38

3.6	Planar Waveguide Formulation for Exceeding The Ray Optic Limit . . .	41
4	Light Trapping With Dielectric Nanosphere Resonators	49
4.1	Dielectric Nanosphere Resonators for a-Si Absorption Enhancement . . .	50
4.2	Dielectric Nanosphere Resonators for GaAs Absorption Enhancement . . .	58
5	Light Trapping In Ultrathin Film Si With Photonic Crystal Superlattices	69
5.1	Introduction	69
5.2	Superlattices In A Square Photonic Crystal	73
5.3	Superlattices In An Optimized Hexagonal Photonic Crystal	80
5.4	Addition Of A Randomly Textured Dielectric Incoupler	82
5.5	Thicker Absorber Layers	84
5.6	Conclusions	85
6	Light Trapping In Thin Film GaAs	87
6.1	Introduction	87
6.2	Epitaxial Liftoff of Ultra-thin Film GaAs	90
6.3	Pattern Optimization and Electromagnetic Simulations	92
6.4	Light Trapping in Ultra-thin Film GaAs Using Nanoimprint Lithography . . .	98
7	Summary And Outlook	106
7.1	Exceeding The Ergodic Limit In Si	106
7.2	Purcell Enhanced Photovoltaics	108
7.3	Photonic Molecules For Light Trapping And Angular Response Engineering	112
7.4	Light Absorption Enhancement in Thin Film GaAs	114
	Appendices	116

A GaAs Epitaxial Liftoff Procedure	116
B Mesa Etching And Contacting Procedure	120
Bibliography	123

List of Figures

1.1	Current voltage curve for a p-n junction in the dark and under illumination.	8
1.2	Effects of thinning a solar cell on J_{sc} , V_{oc} , and efficiency.	12
2.1	Absorption depth for various photovoltaic materials	14
2.2	Modes of a slab in 3 different representations.	16
2.3	Coupling into a slab with a diffraction grating.	19
2.4	Shcematic showing modes of a slab accessed with planar and Lambertian surfaces.	21
3.1	Traditional limits to photogenerated current.	24
3.2	Potential solar cell architectures.	31
3.3	GaP and CdSe slot waveguide LDOS	33
3.4	Photonic Crystal LDOS	35
3.5	Ag nanoantenna LDOS	36
3.6	LDOS Enhancements needed to absorb the entire solar spectrum. . . .	37
3.7	Schematic of spectral reweighting needed to achieve density of states enhancements.	38
3.8	FDTD simulation of P3HT:PCBM absorber.	39
3.9	Angular behavior of the P3HT:PCBM structure that exceeds the ergodic limit.	40
3.10	FDTD simulation of P3HT:PCBM absorber with Ag resonators.	41
3.11	Waveguide dispersion relations.	44

3.12	Plasmonic waveguides that beat the $4n^2$ limit.	46
3.13	Slot waveguides that beat the $4n^2$ limit.	47
3.14	Absorption for a plasmonic waveguide cladded with a GaP top layer. .	48
4.1	Dielectric spheres on a-Si.	51
4.2	Electric field profiles for dielectric spheres on a-Si.	52
4.3	Angular behavior for dielectric spheres on a-Si.	55
4.4	Sphere diameter vs. wavelength vs. absorption on a-Si.	57
4.5	Current density of a flat GaAs solar cell as a function of thickness. . .	59
4.6	Schematic of a GaAs solar cell with hexagonally close packed SiO_2 nanospheres.	62
4.7	Behavior of GaAs solar cell with SiO_2 nanospheres.	63
4.8	Behavior of GaAs solar cell with SiO_2 nanospheres.	64
4.9	Behavior of GaAs solar cell with SiO_2 nanospheres.	68
5.1	Conceptual diagram illustrating different degrees of randomness and order.	69
5.2	Absorption spectra of a planar Si layer and photonic crystal.	71
5.3	Four different superlattice geometries and their spectral absorption. . .	72
5.4	Absorbed current as a function of superlattice air hole diameter.	74
5.5	Field profiles for photonic crystal superlattices.	75
5.6	Field profiles for photonic crystal superlattices.	76
5.7	TE-TM averaged angular absorption spectra for photonic crystal super- lattices.	77
5.8	Integrated angular absorption spectra for photonic crystal superlattices.	78
5.9	Density of states maps of photonic crystal superlattices.	79
5.10	Absorption of Suzuki lattice photonic crystals.	81
5.11	Integrated absorbed current of Suzuki lattice photonic crystals.	82

5.12	TE-TM averaged angular absorption spectra Suzuki lattice photonic crystals.	83
5.13	Schematic of superlattice photonic crystal with randomly textured incoupler.	83
5.14	Thicker superlattice photonic crystals with randomly textured incouplers.	85
6.1	GaAs solar cell device architecture.	88
6.2	Images and J-V curve of GaAs device after processing.	89
6.3	Sample to sample and cell to cell variation in thin-film GaAs J-V curves made via epitaxial liftoff.	90
6.4	Bilayer anti-reflection coating optimization for GaAs solar cell.	91
6.5	Hexagonal TiO ₂ cylinder FDTD optimization.	92
6.6	RCWA simulations of angular response of planar cell and cell with optimized square lattice.	93
6.7	AM1.5G spectrally integrated absorbed current for planar anti-reflection coated cell and TiO ₂ nanopatterned cell.	94
6.8	Electric field intensities for several resonant modes observed in the angular absorption spectrum.	95
6.9	Quantification of losses in each layer of the GaAs solar cell structure. .	96
6.10	Angular spectra of the GaAs solar cell with the rear contact removed with and without addition of an optimized nanopattern.	97
6.11	Integrated absorbed current for 4 different GaAs solar cell configurations.	98
6.12	1.5 cm x 1.5 cm master and resulting PDMS stamp.	99
6.13	Optical image of a hexagonal pattern of TiO ₂ nanoparticles on Si. . .	100
6.14	SEM images of a hexagonal pattern of TiO ₂ nanoparticles on Si. . . .	101
6.15	GaAs solar cells after TiO ₂ nanopatterning and SiO ₂ deposition. . . .	102

6.16	Current density-voltage curves for cells with and without a TiO ₂ nanoparticle coating.	103
6.17	External quantum efficiency measurements of different positions of single cells with and without nanopatterning.	103
6.18	Angle-dependent external quantum efficiency measurements of different positions of single cells with and without nanopatterning.	104
6.19	Short-circuit current as a function of angle as determined from EQE measurements for nanopatterned and AR coated areas of a single cell. .	105
7.1	Thicker superlattice photonic crystals with randomly textured incouplers.	107
7.2	Maximum attainable open circuit voltage vs. Purcell Factor.	110
7.3	Potential photonic molecule configurations.	112
7.4	Assembly of potential photonic molecules by colloidal self assembly. . .	113

Chapter 1

Introduction

World energy consumption is currently above 15 TW, and is expected to increase by 56% by 2040 [1]. The majority of this energy is extracted from a combination of coal, oil and natural gas. These non-renewable resources, while currently dominant, will eventually be depleted. Even before then, continued use of fossil fuels will only worsen the environmental impact of CO₂ emissions associated with burning of these energy resources. The earth intercepts about 3.4 million EJ of radiation from the sun each year, about 7,500 times the worlds current energy consumption. This annual solar energy is also an order of magnitude greater than the energy contained in all the worlds estimated fossil fuel reserves and nuclear energy resources combined [2]. However, as of 2010, only about 0.1% of the worlds consumed energy is generated from photovoltaics [3]. No matter how one looks at it, it is obvious that solar energy utilization will have to grow to meet the worlds increasing energy needs. Given these numbers, it also seems inevitable that renewable energy resources like solar will eventually displace fossil fuels as the worlds dominant energy source. In fact, a recent study [2] predicts solar energy (photovoltaic and solar thermal) to provide 70% of world energy generation by 2100. A different study predicts 11% of the worlds total energy needs to come from photovoltaics alone by 2050 [3]. These numbers are based on the sustained growth of the photovoltaics industry over the last decade. In 2012, the world surpassed 100 GW of globally installed PV, and has grown by about 30

GW in each of the last 2 years [4].

To fuel a growing industry such as PV, research and development is needed to reduce the cost per watt of electricity generation. For photovoltaics, this translates to a need for research that reduces the usage of raw materials, reduces the cost of manufacturing and, equally as important, increases energy conversion efficiency. This thesis will explore concepts aimed at achieving these goals using new approaches to light harvesting and device design.

1.1 Rise Of Nanophotonics

In parallel with the development of photovoltaic technology over recent years has been the development of the field of nanophotonics. The unprecedented ability to manipulate and study light on a nano scale has been fueled by recent advances in technology such as electron beam lithography, near field optics, as well as more advanced computer processing power and computation techniques such as finite difference time domain (FDTD) and rigorous coupled wave analysis (RCWA). Entire fields such as those based on photonic crystals [5], plasmonics [6] and metamaterials [7] have been developed, accelerating the growth of knowledge related to nanoscale light manipulation. This has led to impressive strides in the development of fields such as quantum optics [8], nanoscale lasers [9], near field imaging [10] and others. Despite the continual growth of the closely related fields of photovoltaics and nanophotonics, only recently have they started to merge, giving birth to a rich and interesting new research frontier, that of nanophotonic solar cells [11, 12].

1.2 Solar Cell Fundamentals

The sun can be viewed as a blackbody at a temperature of about 5800 K that continuously emits energy in the form of photons. The energy of these photons can be

harvested in numerous ways, such as through heating of an absorbing material or fluid (i.e. solar thermal), or by taking advantage of the photovoltaic effect in a semiconductor and extracting excited charge carriers at a voltage to create electrical power. While this thesis focuses mainly on photovoltaic devices, the concepts regarding light trapping and absorption are applicable to both areas of solar energy harvesting.

In a photovoltaic device, photons with energy above the material's bandgap are absorbed, exciting electron-hole pairs that can be extracted as electrical current at an applied voltage to give electrical power. The amount of extracted power divided by the amount of incident power from the sun gives the energy conversion efficiency.

In 1961, Shockley and Queisser calculated the theoretical maximum efficiency of a semiconductor photovoltaic device using the principle of detailed balance [13]. For this calculation, they first considered a photovoltaic device in equilibrium with its surroundings at an ambient temperature, T . This ambient temperature will have an associated blackbody spectrum of ambient photons, some of which the device will absorb. Exactly how many it absorbs depends on the absorptivity, $A(\omega)$, of the device, a function of the complex dielectric function of the absorbing material and the geometry. Since the solar cell is in equilibrium, the photons that are absorbed have to be balanced by an outgoing flux of emitted photons. The recombination causing this photon flux constitutes the minimum dark current, I_o , of the solar cell. This current flowing across the junction will increase exponentially when an external voltage is applied, giving the diode equation:

$$I(V) \approx I_o e^{\frac{qV}{kT}} \quad (1.1)$$

When the device is placed in a stronger illumination source, such as the sun, a much greater amount of electron hole pairs is excited and the device is no longer in equilibrium. These extra electron hole pairs flow in the opposite direction across the junction and can be collected and extracted as electrical current. Defining the total

amount of photoexcited current I_L , this gives a new I-V equation for an illuminated device:

$$I(V) \approx I_o e^{\frac{qV}{kT}} - I_L \quad (1.2)$$

The resulting dark current-voltage (I-V) curves for a diode in the dark and under illumination are shown in Figure 1.

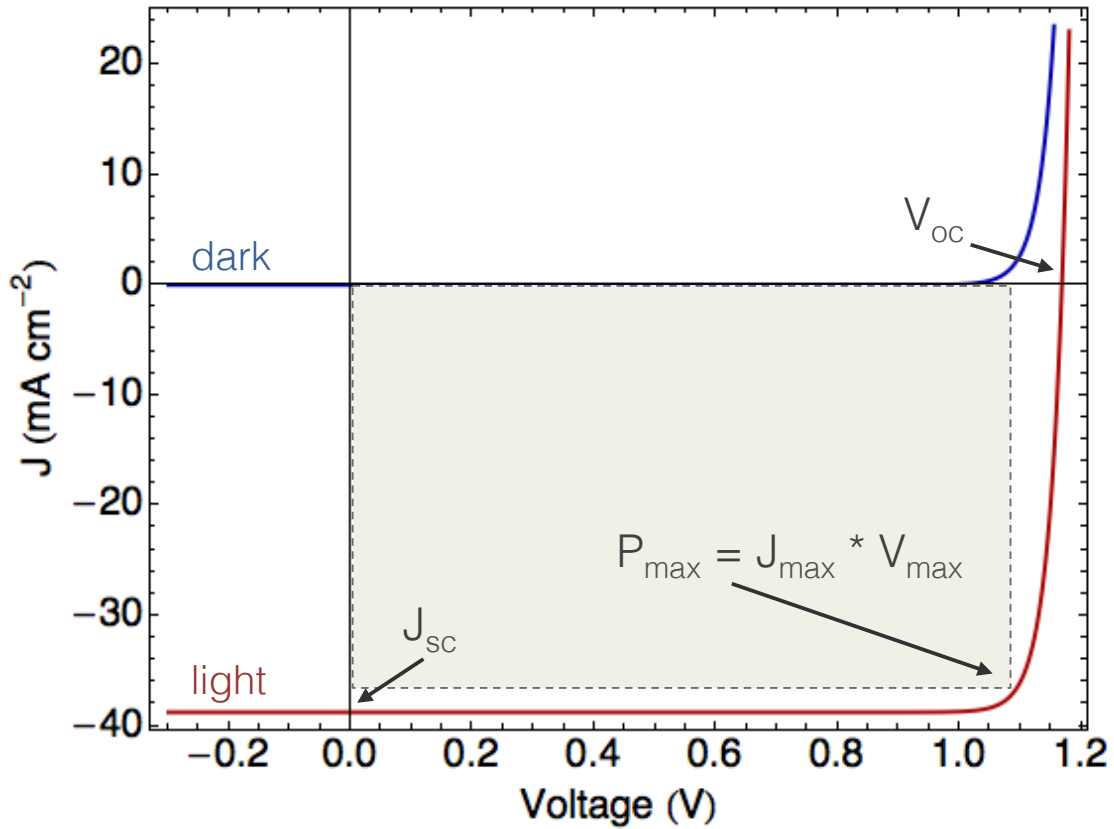


Figure 1.1: Current voltage curve for a p-n junction in the dark and under illumination. The important solar cell parameters J_{sc} , V_{oc} , FF and efficiency can be easily extracted.

Typically, the current is normalized by the area of the device receiving illumination, and the current density, J ($\frac{\text{mA}}{\text{cm}^2}$) is used rather than I (A) when describing solar cell devices.

This light J-V curve can be used to define a number of important parameters

widely used to characterize a solar cell's performance.

1. J_{sc} or short-circuit current: A measure of how well the solar cell absorbs light. This will depend on the thickness, geometry of the absorbing material as well as the dielectric function and the light-matter interaction. This is obtained by measuring the collected photocurrent a short-circuit when no voltage is applied to the device.
2. V_{oc} or open-circuit voltage: A measure of how well the device separates charge. This will first depend on the built-in voltage, a function of the bandgap of the material and the doping levels within the device. V_{oc} will also depend on how much recombination occurs in the device, including radiative and non-radiative channels, which affects the dark current, J_o . The V_{oc} is defined by solving the light J-V curve for V at J = 0 (i.e. the open-circuit condition):

$$V_{oc} = \frac{kT}{q} \ln\left(\frac{J_{sc}}{J_o}\right) \quad (1.3)$$

3. FF: Corresponds to the squareness of the J-V curve and is defined by $FF = \frac{J_{max}V_{max}}{J_{sc}V_{oc}}$. This will depend mostly on series and shunt resistances in the device.

These easily obtained parameters can be used to calculate the power conversion efficiency of the solar cell.

$$\eta = \frac{P_{max}}{P_{inc}} = \frac{J_{sc}V_{oc}FF}{P_{inc}} \quad (1.4)$$

where P_{inc} is the incident power density on the device.

1.3 Current State Of The Art Solar Cells

Using the method of Shockley and Quiesser, the maximum theoretical efficiency of a single junction solar cell of any given material can be calculated. All that is needed is an incident spectrum and the bandgap energy of the semiconductor. Two of the most important solar cell materials are Si and GaAs. The maximum efficiency of a single junction Si solar cell under the AM1.5G solar spectrum is about 30%. Currently, the highest achieved efficiency for a Si solar cell is 25% [14]. This efficiency for Si is currently limited by non-radiative recombination processes intrinsic to Si, such as Auger recombination. The thickness of typical record Si devices is usually above 50 microns. A Si record cell could benefit from advanced light trapping by significantly reducing the amount of active material needed, potentially down to below 5 microns, or more than an order of magnitude.

The theoretical maximum efficiency for a GaAs solar cell is about 33%. The current maximum achieved efficiency is 28.8% [14], by Alta Devices [15] using the epitaxial liftoff process of delaminating a thin film of GaAs from its parent substrate and adding a back reflector. All three of the important solar cell parameters are just slightly below their theoretical maximum values. A GaAs cell could benefit from advanced light trapping by reducing the amount of material needed to absorb the spectrum, potentially increasing the voltage by reducing the volume-dependent dark current.

1.4 Why Thin Solar Cells?

Despite the best Si solar cells being many tens of microns thick, the ultimate solar cell is one that is as thin as possible. There are many advantages for thinning the active layer, with the obvious disadvantage that it decreases light absorption. If the exponential reduction in absorption while thinning the cell can be prevented, a solar

cell could gain the following benefits:

- **Reduced Cost**

The most obvious advantage of a thin solar cell is that it reduces the amount of raw material needed to make the device. As of 2012, about 60% of a Si module cost is due to the Si alone [16]. Reducing the thickness of a Si device by an order or magnitude or more could significantly decrease this cost.

If the solar cell is made from an epitaxial material like a III-V, reducing the active layer thickness will decrease both the amount of precursor gas needed for growth as well as reactor run time for each device. Though direct bandgap materials like GaAs are already relatively thin ($\sim 2\text{-}5$ microns) compared to Si, their thickness could still in theory be reduced to below a micron, as will be shown in the next section.

- **Flexibility**

While a crystalline wafer of a semiconductor such as Si or GaAs is extremely brittle and can crack or shatter if handled improperly, a thin film of these materials can be extremely flexible. This opens up many new applications for solar power that otherwise would not be feasible with wafer-based devices. For example, a flexible module could be rolled out and used when needed as portable charging station, and rolled back up and stored conveniently when not needed. A flexible device could be incorporated into clothing or baggage, wrapped around curved surfaces, or even integrated into the outside of an automobile or aircraft.

- **Improved V_{oc} and Efficiency**

Perhaps the most intriguing motivation for making a solar cell as thin as possible is an increased operating voltage and possibility of an overall increased efficiency

compared to a thicker device. This is because the dark current density, J_o , is a function of the total recombination within the device. The more bulk material there is in the device, the more bulk recombination and the higher the dark current. This lowers the V_{oc} as shown in Equation 1.3. Plotted in Figure 1.2a is a calculation of the V_{oc} as a function of thickness for a GaAs solar cell with various amounts of bulk non-radiative recombination current. Also shown is how the J_{sc} decreases with thickness when there is only a single photonic pass. Clearly, in order to take advantage of the increased V_{oc} for thinner cells, significant light trapping is needed to maintain the J_{sc} of thicker cells. Shown in Figure 1.2b is the calculated efficiency of a GaAs cell with various amounts of light trapping. It can be seen that with increased light trapping, the maximum possible efficiency increases and occurs at thinner and thinner cells. Since both V_{oc} and J_{sc} need to be maximized to increase efficiency, the ideal solar cell is one that is as thin as possible yet still absorbs the available light from the sun.

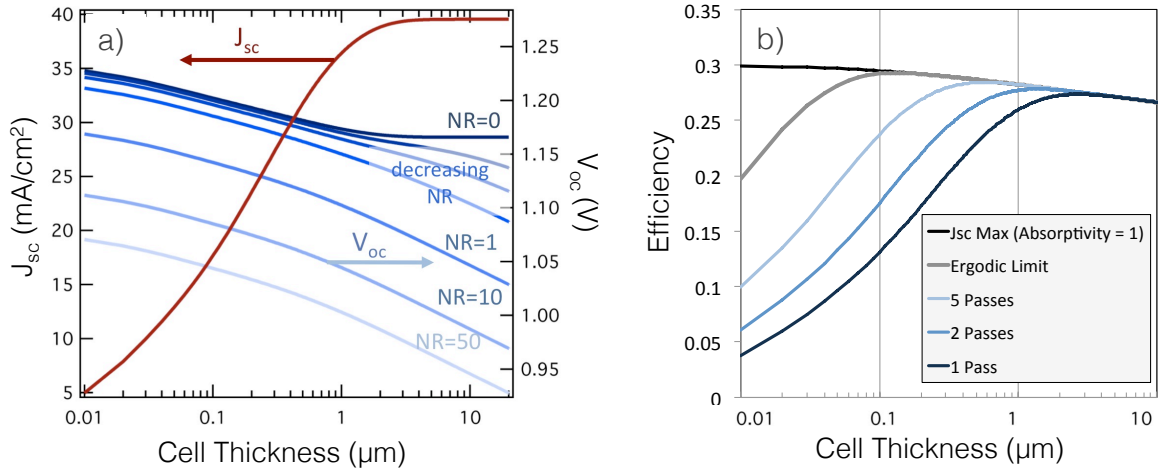


Figure 1.2: a) Effect of thinning a solar cell on J_{sc} and V_{oc} with no light trapping. NR is the amount of non-radiative recombination. b) Efficiency as a function of cell thickness with various amounts of light trapping. The more light trapping, the higher the maximum possible efficiency.

Chapter 2

Light Trapping In Thin Film Solar Cells

2.1 Single Pass Absorption

Photons with energy above a semiconductor's bandgap can be absorbed if given enough time to interact with the material. How quickly light is absorbed depends on the complex dielectric function of the material (i.e. refractive index and absorption coefficient), and the nature of the light-matter interaction. For light propagating freely as a plane wave in a homogeneous material, the amount absorbed, or intensity I , is exponentially dependent on how far it travels, given by the well known Beer-Lambert law:

$$I(z) = I_0 e^{-\alpha z} \quad (2.1)$$

A commonly used metric for electromagnetic absorption is the absorption depth, $\frac{1}{\alpha}$ defined as or the depth at which the intensity of a wave decays to $\frac{1}{e}$ (about 35%) of its initial value. Plotted in Figure 2.1 is the absorption depth for some common semiconductors.

A few things are clear from this plot. First, some materials absorb light much more strongly than others. For example, a direct bandgap material like GaAs has a

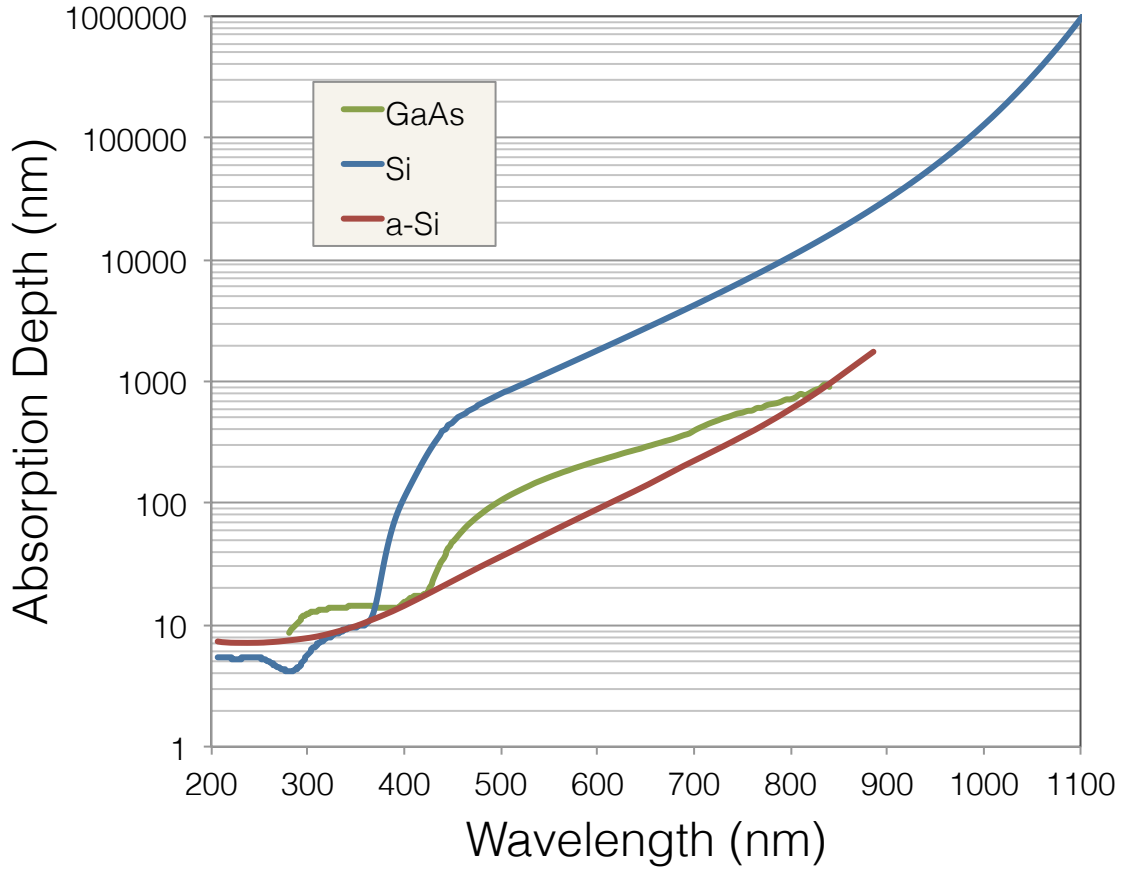


Figure 2.1: Absorption depth for common photovoltaic materials used in this thesis.

much shorter absorption depth across the entire spectrum compared to an indirect semiconductor like Si. This will dictate typical thicknesses for each type of solar cell, with GaAs solar cell thicknesses being a few microns and Si thicknesses being many tens or even hundreds of microns. Second, for nearly all materials, the absorption depth is a strong increasing function of wavelength. This has strong implications for light trapping, as the wavelengths that need the most consideration will be the longer ones, and the bandwidth of interest will depend on the thickness of the material.

2.2 Modes Of A Slab

In order to design structures for light trapping, an understanding of the optical modes of a semiconductor slab is critical. Consider a dielectric slab of material with a refractive index, n_2 , surrounded by an upper dielectric material with index, n_1 , and a lower dielectric with index n_3 . Following Yariv [17], we find that different types of electromagnetic modes exist in the slab for a single frequency. Modes that have oscillating field components both inside and outside the slab are known as radiation modes. Modes which are oscillating inside the slab but decay exponentially outside the slab are known as bound or trapped modes. Each of these will be described in more detail below.

The nature of the modes of a slab depends on the relative surrounding refractive indices and a very important quantity known as the propagation constant, β , or in-plane wavevector, $k_{||}$. It is useful to plot the relationship of wavevector and frequency in a dispersion diagram, as is shown in Fig. 2.2a,d. From this single diagram, we can describe and understand the modes that exist in most photonic structures.

We start with the definition of wavevector for a plane wave propagating in a homogeneous medium:

$$\omega = \frac{ck}{n} \quad (2.2)$$

where c is the speed of light and n is the refractive index of the material the photon is propagating in. If we define the in-plane wavevector $k_{||}$ as the component of the wavevector in the plane of the slab, we can start to describe the photon with the dispersion diagram. For a photon propagating inside the incident material with index, n_1 , it will have a $k_{||}$ of 0 when it is normal to the plane of the slab. As the incident angle is increased off-normal, it will gain a parallel component dependent on the angle and its frequency:

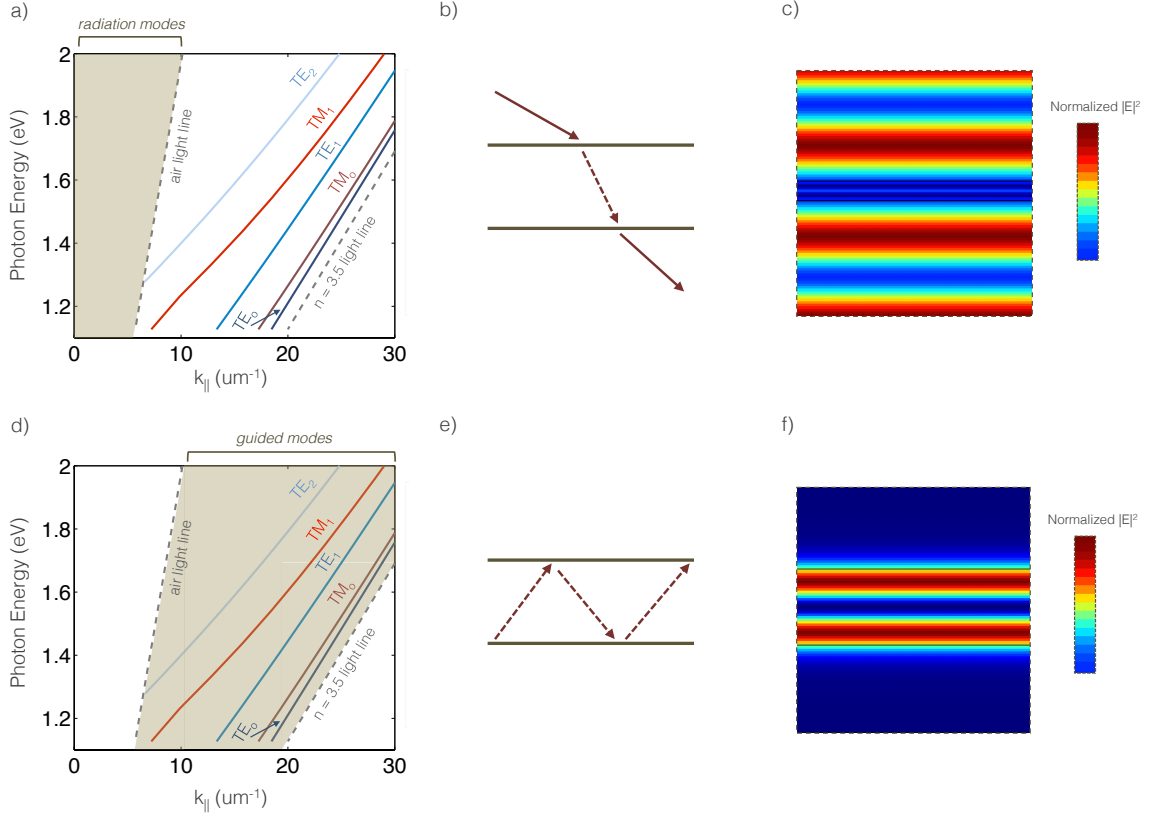


Figure 2.2: (top) Radiation modes of a 300 nm slab of index $n = 3.5$ in air represented (a) on a dispersion diagram (b) with ray optics and (c) as electric field intensity as a function of position. (bottom) Guided modes represented in the same 3 ways.

$$k_{||} = k \sin(\theta) \quad (2.3)$$

If the photon is propagating completely in the plane, all of its wavevector will be in the parallel component and it can be described by:

$$k_{||} = \frac{n\omega}{c} \quad (2.4)$$

This forms what is commonly known as the light line in the dispersion diagram as shown in Fig 2.2a.

Here we can see that as the refractive index of the material of propagation increases, the wavevector also increases. This means that the dispersion of photons

propagating in higher indices will appear towards the right on the dispersion diagram.

A photon incident on a planar slab at any of these angles will refract at an angle according to Snell's law, propagate through the slab at that angle, and exit the slab again at an angle according to Snell's law (at each interface, of course, portions will not only be refracted but also reflected as dictated by the Fresnel equations). This is commonly known as a single pass through the material and would result in minimal absorption if the material were a solar absorber. Adding a back reflector will only add a second pass, with the photon exiting from the top instead of the bottom if it is not absorbed. The set of modes and corresponding in-plane wavevectors associated with this are known as radiation modes and are shown in three different descriptions in Fig 2.2a-c. It is important to note that for a planar interface, these radiation modes are the only modes that can be accessed by photons incident from free space, which only results in 1-2 passes depending on if there is a back-reflector or not.

Photons that gain extra in-plane momentum ($k_{||}$) can access another set of modes that exist in the slab, called bound modes. These modes can be understood from a ray optics perspective as light trapped by total internal reflection. In the wave optics picture, these modes have oscillating fields within the slab and exponentially decaying fields outside the slab. These modes will have in-plane wavevectors between the light line of the incident medium and the light line of the bulk medium of the slab, given by $\omega = \frac{ck}{n_2}$. They form discrete bands in the dispersion diagram and may have multiple solutions at a single frequency corresponding to different mode orders. These modes are calculated and shown in Fig. 2.2d-f in 3 different representations for a 300 nm slab with refractive index 3.5 surrounded by vacuum.

A photon or wave in a trapped mode will stay trapped forever unless 1) something changes its momentum ($k_{||}$) by scattering or diffracting it out of the waveguide or into a different mode or 2) it is absorbed (if the material is absorbing at that wavelength).

Similarly, as stated before, a photon starting out in the lower index incident medium cannot enter one of these trapped modes unless something changes its momentum. Clearly, a photon trapped in a bound mode (having many effective passes) has a much greater chance of getting absorbed than a photon in a radiation mode (only 1-2 passes). Getting photons from free space with low in-plane momentum into trapped modes where they can be most efficiently absorbed is the central goal of solar cell light trapping.

2.3 Accessing Trapped Modes

In order for a photon incident from free space to access the guided modes of a slab, its in-plane momentum must be changed so that it matches that of the trapped modes.

A photon can elastically scatter off of a particle that has dielectric contrast with its surroundings if the particle's size is comparable to the wavelength. This will alter the momentum of the photon and may allow it to couple to nearby optical modes with various momenta. In the wave picture, this occurs because the photon is localized during the scattering event, introducing new, larger k -vectors (modes in k -space are inversely proportional to modes in real space) in the vicinity of the scattering particle [18]. If the particle is close enough to an optical mode (e.g. a guided mode of a slab), and the fields overlap, the energy of the incident wave can be transferred to the optical mode. In the quantum picture, scattering events are described by Fermi's golden rule, which states that a scattering event will send the scattered particle (i.e. a photon) into a new state depending on the nearby density of states. As we will see in the next section, a dielectric slab with a higher index than the incident medium has a higher density of optical states than its surroundings, and will preferentially accept photons scattered at the interface between the two media. A single isolated scatterer or a set of random, uncoupled scatterers will ideally redistribute the incident light in

many different directions, or angles from its incident angle.

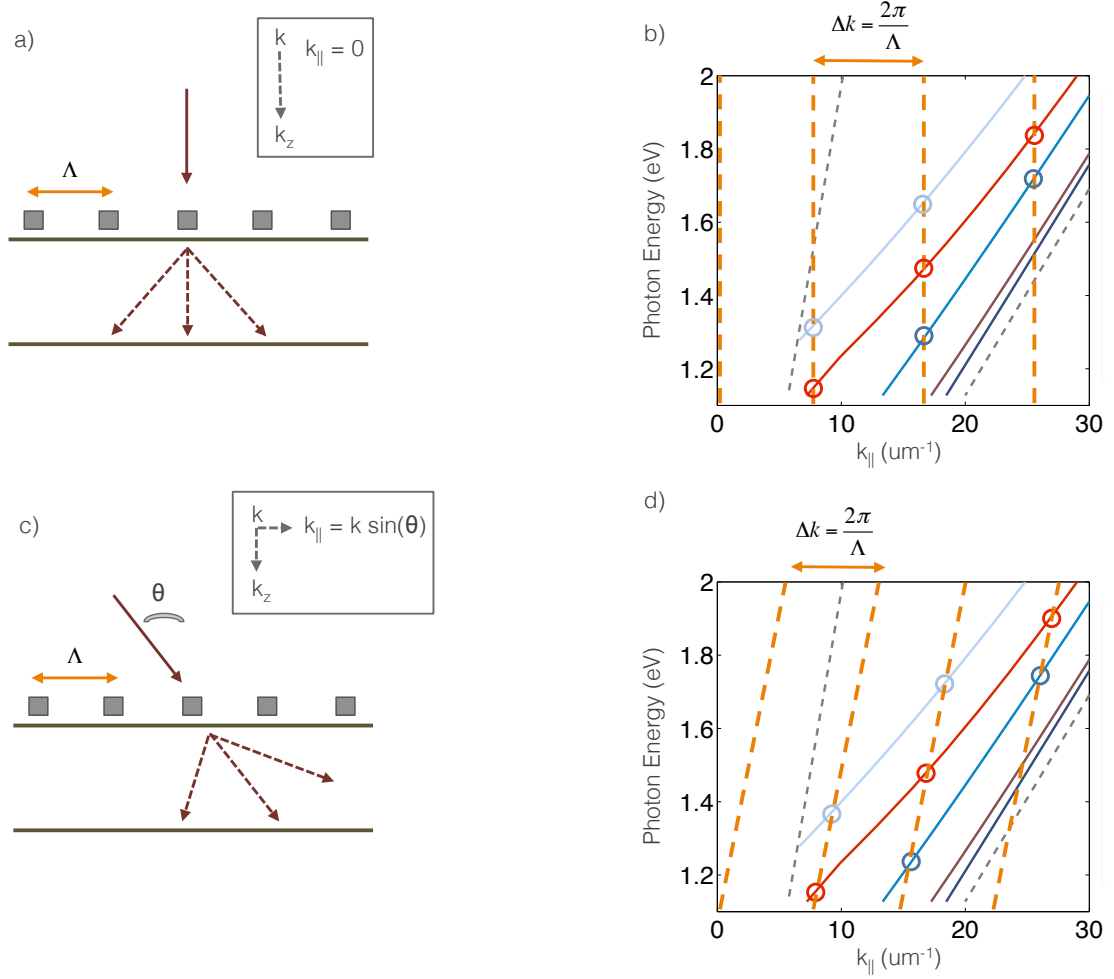


Figure 2.3: Coupling into a slab with a diffraction grating. The intersecting lines in (b) and (d) occur at wavelengths where light can be coupled into guided modes at a given angle. (top) Normal incidence. (bottom) Off-normal incidence.

Another way to access the guided modes of a slab is through diffraction. Diffraction can be viewed as a series of scattering events with the scatterers arranged in an ordered, periodic pattern. In the wave picture, certain angles of propagation are allowed due to constructive interference between the scattered waves, and other angles disallowed due to destructive interference. An ordered array of scatterers with period Λ , will add and subtract in-plane momentum from an incident plane wave with values of $\frac{2\pi n}{\Lambda}$, where n is an integer. These new values of in-plane momentum

can also correspond to new angles of propagation given by the diffraction equation:

$$m\lambda = \Lambda \sin(\theta_m) \quad (2.5)$$

where λ is the wavelength of light and m is an integer. This is schematically shown in Fig. 2.3a using the dispersion diagram of Fig. 2.2. Light can be coupled into the slab at the locations where the diffraction lines intersect the bands corresponding to the trapped modes of the slab. If the incident angle is changed, the starting value of $k_{||}$ will change, but the values of added momentum will not. This will only change the resonant wavelengths which couple into the slab as shown in Figure 2.3b. It is important to note that at a given angle, there is only a subset of available modes that can be accessed with a diffraction grating (i.e. the intersecting lines in Fig. 2.3), depending on the period of the grating and the incident angle. Alternately, scattering from single point sources or random surfaces as previously described can potentially couple light into all of the available modes of the slab. If the scattering surface is ideal, it will also do this at all angles. For this reason, random scattering surfaces are typically more useful for broadband, varied angle incoupling for applications such as solar cells.

2.4 The Ray Optic Light Trapping Limit

In 1982, Yablonovitch [19] published a theory describing a fundamental limit to how much light trapping could be achieved in a thin slab of semiconductor with ideal scattering surfaces. This limit is known as the ray optic light trapping limit, also often called the ergodic limit.

Yablonovitch arrives at this limit by considering a homogeneous slab of material with a refractive index, n , and immersing it in a vacuum (with refractive index 1 by definition) that contains blackbody radiation at a temperature, T . When the

radiation inside the slab reaches equilibrium with its surroundings, we can compare energy densities inside and outside the slab:

$$U_{in}(r, \omega) = \frac{n^3 \omega^2}{\pi^2 c^3} \cdot \frac{1}{e^{\frac{\hbar \omega}{kT}} - 1} \cdot \hbar \omega \quad (2.6)$$

$$U_{out}(r, \omega) = \frac{\omega^2}{\pi^2 c^3} \cdot \frac{1}{e^{\frac{\hbar \omega}{kT}} - 1} \cdot \hbar \omega \quad (2.7)$$

They clearly only differ by a factor of n^3 .

Absorption is directly related to optical intensity, so by converting the energy density to an intensity by multiplying by the group velocity $v_g = \frac{d\omega}{dk}$ and using the well known relation $\omega = \frac{ck}{n}$, the intensities become:

$$I_{in}(r, \omega) = \frac{n^2}{\pi^2 c^2} \cdot \frac{\hbar \omega^3}{e^{\frac{\hbar \omega}{kT}} - 1} \quad (2.8)$$

$$I_{out}(r, \omega) = \frac{1}{\pi^2 c^2} \cdot \frac{\hbar \omega^3}{e^{\frac{\hbar \omega}{kT}} - 1} \quad (2.9)$$

Which differ by only n^2 . If a simple back reflector is added to add a second pass for any light that escapes the rear of the slab, this intensity enhancement increases to $2n^2$. After averaging over all angles using a ray optics approach, Yablonovitch comes to an overall absorption, or path length, enhancement of $4n^2$.

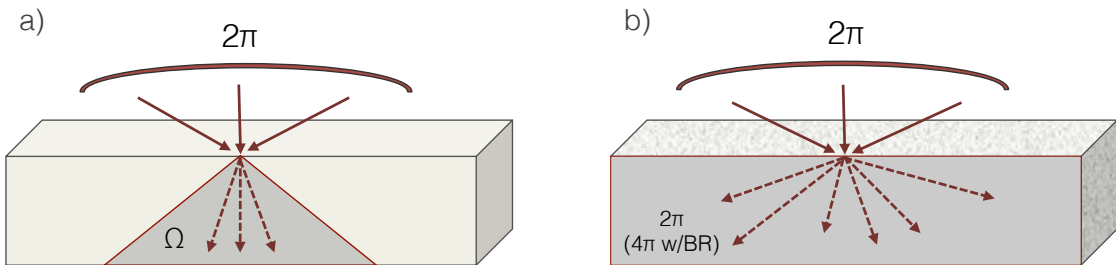


Figure 2.4: (a) Modes of a planar slab accessed at all incident angles, (b) Modes of a Lambertian textured slab accessed at all incident angles.

An intuitive way to understand where the $4n^2$ path length enhancement comes from is by considering the escape cone for light inside the slab. As mentioned previously, a subset of modes known as radiation modes exist inside the slab and can be accessed from free space. If the angle of incident light were swept through all 2π steradians outside the slab as shown in Fig. 2.4, the refracted rays inside the slab would sweep out a cone known as the escape cone. The solid angle, Ω , of this cone is less than the 2π steradians outside because of Snell's law of refraction and the fact that the index of the slab is higher than free space. Any angles outside of this cone correspond to trapped modes of the slab and cannot be accessed from free space without a momentum changing event. Now, consider a slab with perfectly Lambertian textured surfaces. These surfaces will scatter the light ideally into all 4π steradians that exist inside the slab. This ratio of internal angles, or modes accessed, gives the $4n^2$ light trapping limit.

$$\frac{4\pi}{\Omega} \approx 4n^2 \quad (2.10)$$

by series expansion and trigonometric identity where $\Omega = 2\pi(1 - \cos \theta)$ and $\theta = \sin^{-1}(\frac{1}{n})$. In this sense, reaching the light trapping limit can be understood as when incident light is able to access all of the modes inside the slab (both radiative and bound).

Chapter 3

Light Trapping Beyond The Ray Optic Limit

To utilize many of the benefits of ultrathin solar cells, the active layers for most materials have to be reduced to thicknesses where traditional light trapping is no longer effective. At some point, even light trapping that reaches the ray optic, ergodic limit is not enough to generate reasonable short circuit currents, particularly in the wavelength range near the semiconductor bandgap. For any given thickness, there is a range of wavelengths that is near fully absorbed upon $4n^2$ optical passes and another range that is not fully absorbed due to the exponential nature of the absorption process and the fact that the absorption coefficient approaches zero at the semiconductor band edge (Fig. 2.1). Therefore we can divide our conceptual approach to the light trapping limit between the spectral region where enhanced absorption is needed and where it is not. The transition region between these two regimes depends on the material properties, thickness, structure, etc.

There is previous evidence that solar cells with non-slablike geometries that operate in the wave optic rather than ray optic limit may exceed this limit [20–24], and recent theoretical work has successfully explained the phenomena in selected cases [25, 26]. The theory of Yu et al. establishes a relationship between the modes supported in a slablike solar cell and the maximum absorption attainable but is not easily extensible to the broad portfolio of light trapping schemes currently being ex-

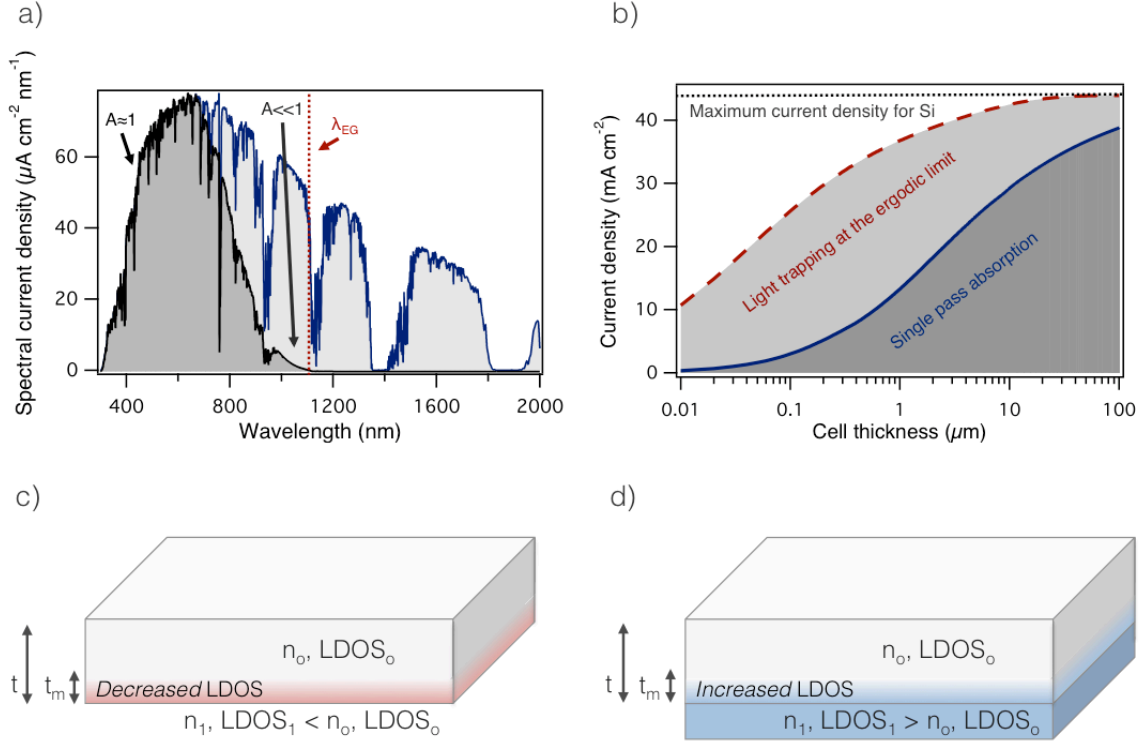


Figure 3.1: Traditional limits to photogenerated current. (a) Current density resulting from AM1.5 solar spectrum absorption for various thicknesses of a bulk slab of Si (inset) assuming either exponential absorption from a single pass or $4n^2$ passes at the ergodic light trapping limit. (b) Spectrally resolved absorbed current for a 100 nm slab of Si with light trapping at the ergodic limit. There is a significant region near the band edge where increased light trapping is needed beyond the ergodic limit. (c) A thin slab of semiconductor where the LDOS is affected by a lower index surrounding environment and (d) a higher index surrounding environment.

plored in the literature [11, 21, 27].

We find that a common defining feature of light trapping structures that can exceed the ray optic limit is that the electromagnetic local density of optical states (LDOS) integrated over the active absorber region must exceed that of the corresponding homogeneous, bulk semiconductor. That the density of optical states plays an important role in defining the light trapping limit has been alluded to in previous work [25, 28, 29], and we use it here as a defining approach for understanding light trapping. We develop a unified framework for thin film absorption of solar radiation and show that an enhanced integrated LDOS is the fundamental criterion that de-

termines whether light trapping structures can exceed the ray optic light trapping limit, leading to a strategy for design of solar absorber layers with wavelength-scale characteristic dimensions that exhibit optimal light trapping.

3.1 Condition for Exceeding The Ray Optic Limit

As in the original ray optics formulation [19], the electromagnetic energy density serves as a starting point for examining the partitioning of energy between the solar cell and the surrounding environment. For any given geometry, the electromagnetic energy density is a function of position. One way to express the electromagnetic energy density is in terms of the local density of optical states (LDOS), $\rho(r, \omega)$, the modal occupation number $\langle \nu \rangle$, and the energy of each mode, $\hbar\omega$:

$$U(r, \omega) = \rho(r, \omega) \cdot \langle \nu \rangle \cdot \hbar\omega \quad (3.1)$$

The modal occupation number is summed over all modes of the structure. In a homogeneous environment with refractive index, n , and with purely thermal Bose-Einstein occupation, the electromagnetic energy density takes the familiar form:

$$U(r, \omega) = \frac{n^3 \omega^2}{\pi^2 c^3} \cdot \frac{1}{e^{\frac{\hbar\omega}{kT}} - 1} \cdot \hbar\omega \quad (3.2)$$

By examining the ratio of energy densities inside and outside the solar cell at thermal equilibrium, we can determine the maximum light intensity enhancement and thus the maximum light trapping that is possible [19]. We do this by taking the ratio of electromagnetic energy densities in two distinct cases of interest. This gives an important ratio, that includes the LDOS ratio and the modal occupation number ratio:

$$\frac{U(r, \omega)_{case1}}{U(r, \omega)_{case2}} = \frac{\rho(r, \omega)_{case1}}{\rho(r, \omega)_{case2}} \cdot \frac{\langle \nu \rangle_{case1}}{\langle \nu \rangle_{case2}} \quad (3.3)$$

This same ratio can be obtained by starting with an expression for the local absorption rate:

$$A(r, \omega) = \frac{1}{2} \omega \cdot \epsilon''(r, \omega) \cdot E(r, \omega)^2 \quad (3.4)$$

The absorption can be related to the energy density by rewriting the energy density in terms of the ambient dielectric function and the electric field intensity. In limit of a lossless, dispersionless medium:

$$U(r, \omega) = \frac{1}{2} \epsilon(r, \omega) \cdot E(r, \omega)^2 + \frac{B(r, \omega)^2}{2\mu(r, \omega)} = \epsilon(r, \omega) \cdot E(r, \omega)^2 \quad (3.5)$$

Equating this with equation 3.1 and rearranging we have for the electric field intensity:

$$E(r, \omega)^2 = \frac{1}{\epsilon(r, \omega)} \cdot \rho(r, \omega) \cdot \langle \nu \rangle \cdot \hbar \omega \quad (3.6)$$

We can insert this into our expression for local absorption rate to determine how the LDOS and modal occupation number affect absorption:

$$A(r, \omega) = \frac{1}{2\epsilon(r, \omega)} \cdot \epsilon'' \cdot \rho(r, \omega) \cdot \langle \nu \rangle \cdot \hbar \omega^2 \quad (3.7)$$

Because equations 1 and 4 assume lossless materials, we can only introduce a small amount of absorption before these concepts become ill-defined. It is nevertheless common to use expressions like this in the limit of low absorption to describe light trapping phenomena, as has been done both in the original derivation [19] and subsequent treatments [25, 26]. We will find next, however, that Eq. 3.7 is not necessary but rather has been used to verify the importance of energy density ratios. As

with the expressions for energy density, we can now take the ratio of local absorption rate for 2 distinct cases of interest and again obtain Eq. 3.3.

We can use this ratio to examine numerous cases of interest. In the limit of large thicknesses, we will recover the ray optic light trapping limit for homogeneous materials in Section 3.2. First, we compare a homogeneous absorber with an arbitrarily designed absorber that may be capable of exceeding the ray optic light trapping limit:

$$\frac{\rho(r, \omega)_{case1}}{\rho(r, \omega)_{case2}} \cdot \frac{\langle \nu \rangle_{case1}}{\langle \nu \rangle_{case2}} = \frac{\rho(r, \omega)_{cell}}{\rho(r, \omega)_{bulk}} \cdot \frac{\langle \nu \rangle_{cell}}{\langle \nu \rangle_{bulk}} \quad (3.8)$$

where we have assumed integration over all modes of the structure. When an incoupling mechanism fully populates the modes of each structure, the light trapping enhancement is simply the LDOS ratio between the cell structure and a homogeneous bulk structure which achieves the ergodic limit. This implies that if the LDOS of the cell structure is larger than that of a homogeneous medium with the same refractive index, the ergodic light trapping limit can be exceeded. Inputting the expression for LDOS of a homogeneous medium with refractive index n , we reach the condition for exceeding the ergodic limit:

$$\frac{\pi^2 c^3}{n^3 \omega^2} \rho(r, \omega)_{cell} > 1 \quad (3.9)$$

assuming that all modes of the structure are fully occupied via an appropriately designed light incoupler, which is often taken to be a Lambertian scattering surface.

We now briefly discuss the importance of fully populating the modes of the arbitrarily designed solar cell structure. As the ratio of equation 3.8 indicates, a structure with an elevated LDOS is necessary but not sufficient to exceed the light trapping limit, which also depends on the modal occupation numbers. There are numerous examples of solar cell structures that very likely have an elevated LDOS; however, whether or not they have exceeded the traditional light trapping limit has remained

uncertain [20,23]. Structures that use diffractive elements such as gratings and photonic crystals often couple into only a small subset of the available modes, dictated by momentum conservation. This severely limits the number of modes that are occupied, much like the above-mentioned case of a planar interface. If these structures were integrated with a scattering layer, the full modal spectrum of the device could in principle be excited, and much more light could be absorbed within the solar cell. This would also resolve the relevant problem of limited angular and polarization response associated with many designs. We also note that full modal occupation is not necessary to surpass the ergodic limit, as will be shown below using FDTD calculations.

3.2 Recovering The Ray Optic Limit

Considering first a bulk, homogeneous slab of semiconductor with a planar interface, we find that light incident from all 2 steradians gets coupled into a small subset of the modes within the slab given by the escape cone defined by Snell's law. We call these radiation modes. We assume that all incident light is transmitted to the solar cell, thus each of these radiation modes is fully occupied with the maximum occupation number defined through the modified radiance theorem [30,31]. Each incident mode contains an occupation number, ν_{inc} , and is mapped into a single radiation mode within the semiconductor defined by Snell's Law with maximum occupation number $\nu_{max} = \nu_{inc}$ [30,31]. No more light can be coupled into these radiation modes within the slab as they are fully occupied to the maximum extent dictated by thermodynamics. There are of course $4\pi - \Omega$ modes inside the semiconductor left unoccupied in this case, and we call these trapped or evanescent modes [30]. These trapped modes are inaccessible from free space without a momentum changing event such as scattering or diffraction. We count the number of excitations within the slab by multiplying the

number of modes accessed by their occupation number.

We now look at the same slab of semiconductor with a lambertian scattering surface. We assume that this surface does not alter the density of states within the slab as is often assumed [19, 30]. This means that when we take the ratio of equation 3.8, the LDOS terms will cancel, and we will be left considering only the difference in modal occupation numbers. For an incident mode with occupation number ν_{inc} , the scattering event splits the energy in this mode between all equal modes within the semiconductor. Thus, each of the internal modes, both radiation and trapped, now have a fraction of this energy, let us say $\frac{\nu_{inc}}{4\pi}$. This means that each of the internal modes can be fed more energy as their occupation numbers are not at their maximum value. We can continue to couple light into the semiconductor until each of these 4π internal modes has an occupation number $\nu_{max} = \nu_{inc}$. We again count the number of excitations by multiplying the number of modes by their occupation numbers. We can now take the ratio in equation 3.8 for each of these two cases,

$$\frac{\rho(r, \omega)_{lambertian}}{\rho(r, \omega)_{planar}} \cdot \frac{\langle \nu \rangle_{lambertian}}{\langle \nu \rangle_{planar}} = \frac{\langle \nu \rangle_{lambertian}}{\langle \nu \rangle_{planar}} = \frac{4\pi \langle \nu \rangle_{inc}}{\theta_c \langle \nu \rangle_{inc}} = \frac{4\pi}{\theta_c} \approx 4n^2 \quad (3.10)$$

where we have assumed integration over all modes of the structure. This gives the traditional, or ergodic, light trapping limit.

3.3 Nanophotonic Solar Cell Designs For Exceeding The Ray Optic Light Trapping Limit

We now outline a portfolio of wavelength-scale solar absorber layer designs that exhibit an LDOS modified relative to that of a homogeneous slab of the same material. We begin by examining ultrathin, planar solar cells for which we calculate the LDOS

as a function of position within the semiconductor using the Greens dyadic for a layered planar system [10, 18, 32] and then integrate over position to get the spatially averaged LDOS. For the case of a finite thickness planar absorber, in Fig 3.1c-d, the LDOS modification can be viewed heuristically in terms a slab of thickness t with a homogeneous LDOS (LDOS_o) which is modified from its surface to some depth t_m by the LDOS of the neighboring material. In Fig. 3.2 we plot this averaged LDOS enhancement for various absorber structures as a function of thickness and wavelength. When $t \gg 2t_m$, the absorber LDOS modification by the surrounding materials is negligible, but when $t \approx 2t_m$ the change in the absorber layer LDOS due to the influence of surrounding materials becomes significant. First, in Fig. 3.2a we note that the integrated LDOS for a thin semiconductor slab surrounded by free space or lower index materials is always less than that of its corresponding bulk material as the slab thickness is reduced, implying that the light trapping limit in this structure is actually lower than that of the same material in bulk form. This has been pointed out before using a different methodology [30]. However, when the surrounding material includes a metal back reflector as shown in Fig. 3.2b, the integrated LDOS can exceed that of its corresponding bulk material in finite thickness layers, particularly for thicknesses below 200-300 nm. Further, the metal-insulator-metal (MIM) structure shown in Fig. 3.2c exhibits an integrated LDOS enhancement relative to its corresponding bulk absorber material that is very significant for all thicknesses below 500nm, exceeding 50 for all relevant wavelengths with ultrathin layers below 20 nm.

For a two-dimensional planar structure, the modal density of states can be obtained from the optical dispersion relations. In this case, the density of guided modes per unit area per unit frequency for the m^{th} mode can be written as [30]:

$$\rho_m = \frac{k_m}{2\pi} \left(\frac{d\omega}{dk_m} \right)^{-1} \quad (3.11)$$

where k_m is the propagation constant. In order to increase the density of modes

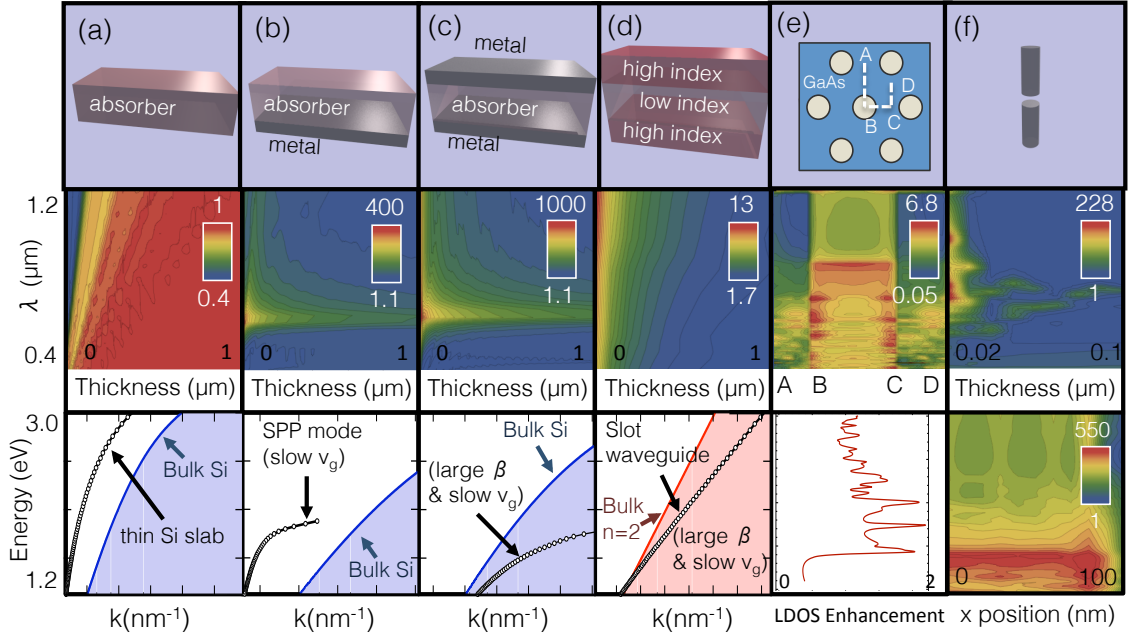


Figure 3.2: Potential solar cell architectures. (a) Planar slab of Si in air in which the LDOS is always below the bulk value. Structures with the potential to beat the ergodic limit: (b) planar slab of Si on an Ag back reflector, (c) Ag/Si/Ag planar structure, (d) high/low/high index structure with refractive indices 3/1.5/3, (e) a photonic crystal with index 3.7, and (f) a split dipole antenna made of Ag with a Si gap. The second row shows the LDOS enhancement (on a log color scale) over the bulk material for each structure for various cell thicknesses and wavelengths. Values of LDOS enhancement > 1 correspond to beating the traditional absorption limit. For (a - d), the bottom row shows examples of the 2D modal dispersion curves for each structure. The bottom of column e shows that the integrated LDOS enhancement > 1 for most wavelengths, and the bottom of column f shows the wavelength dependent LDOS enhancement > 1 for radial positions between the split dipole.

above the homogeneous value, either $k_m > k_0$ or $v_m = \frac{d\omega}{dk_m} < v_o$, where k_0 and v_o are the homogeneous values of the propagation constant and group velocity, respectively. Figure 3.2 also shows for each planar structure examples of the modal dispersion relations, showing regions where the density of states is increased due to either slow (low group velocity) modes or large in-plane propagation constants. Note that these dispersion plots do not fully depict the total LDOS, due to the existence of multiple modes; however, many of the key features can be obtained from the dispersion relations. A full 2D waveguide formulation requires a slightly different analysis, which

will be the subject of section 3.4. For the metallodielectric structures, the plasmonic modes that contribute to the LDOS enhancement exhibit parasitic Ohmic metallic losses, and so exceeding the light trapping limit in any structure incorporating metals, requires the useful absorption within the solar cell semiconductor absorber layer to dominate over parasitic metallic losses. This represents a challenge for successful implementation of certain cell designs incorporating metals, but we demonstrate below that it is possible to exceed the light trapping limit in metallodielectric structures with proper design.

A analogous planar structure without metallic losses is a dielectric slot waveguide [33] in which a low index absorber material is sandwiched between two nonabsorbing cladding layers of higher index, shown in Fig. 3.2d for a core of dielectric constant 1.5 and a cladding of dielectric constant 3. The LDOS within the low index slot will be increased due to the presence of the high index cladding layers, which have an LDOS significantly higher than that for a bulk slab of the low index material. Over the entire range of the solar spectrum there is a significant integrated LDOS enhancement in the dielectric slot (Fig. 3.2d). This effect can also be observed for common inorganic semiconductor materials such as GaP and CdSe. We perform a similar calculation to Fig. 3.2d using the dielectric functions of these realistic, all inorganic materials. For the cladding layer we use the weakly absorbing indirect semiconductor GaP and for the core we use CdSe. These materials fit the criterion at all wavelengths of interest that the refractive index of the core is lower than that of the cladding. In Fig. 3.3 we plot the spatially averaged LDOS enhancement within the CdSe slot for various slot thicknesses. It can be seen that over all wavelengths of interest there is an increased LDOS due to the slot waveguide effect, becoming more pronounced as the slot thickness is reduced.

Dielectric slot waveguides have considerable potential as structures to achieve absorption enhancement in polymer and low index solar cells as there is no metallic

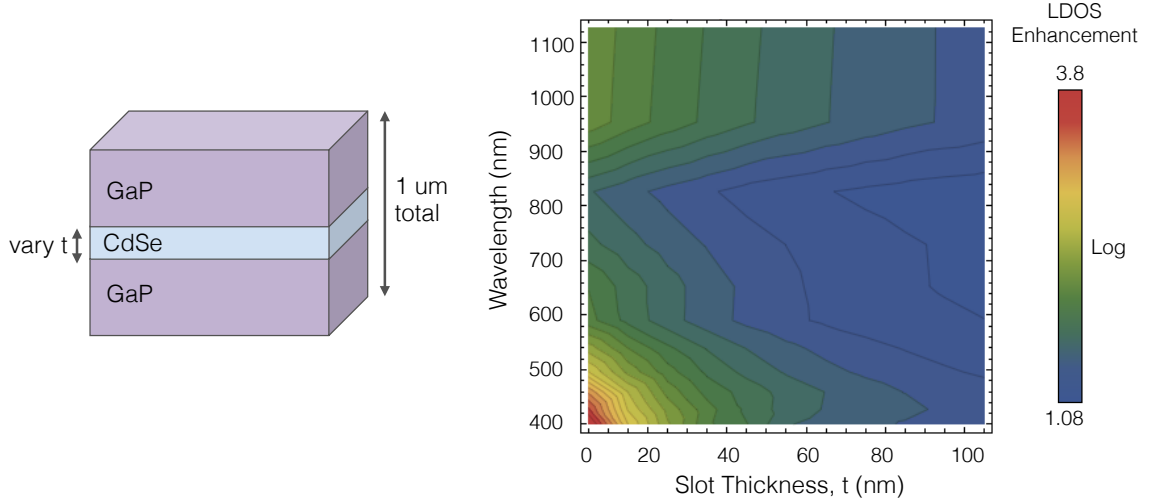


Figure 3.3: (a) Schematic of slot waveguide structure using realistic materials GaP and CdSe. (b) Averaged LDOS enhancement within the CdSe slot as a function of slot thickness with a constant total device thickness of 1 μm .

loss mechanism. This phenomenon for similar structures has also been recognized in two recent works using different methodologies [25, 26].

Next we examine other structures with potential to exceed the light trapping limit. Photonic crystals [5, 34] are interesting candidates as they are known to possess elevated LDOS around flat bands in their dispersive bandstructures. There are at least two ways that photonic crystals can be taken advantage of for solar cells. A photonic crystal could be carved out of a bulk, planar solar cell, or an unstructured, planar solar cell could be integrated with a photonic crystal. The former is certainly intriguing as large LDOS enhancements would be expected but has issues regarding increased surface recombination associated with nanostructuring the active region. Still, utilizing a liquid junction [21] or appropriate passivation of a solid state surface [35] could solve this problem. Here we consider integrating a non-absorbing planar photonic crystal with an unstructured, planar solar cell. This could be easily realized by making the photonic crystal out of an anti-reflection coating material such as SiN_x , ZnS or TiO_2 , or by patterning a window layer such as AlGaAs or InGaP on a III-V solar cell such as GaAs . Here, we take a material of index 3.7, common

for III-V materials like GaAs, InGaP, and AlGaAs, and create a hexagonal lattice of air holes in it with a radius of 205 nm and lattice constant of 470 nm. These parameters are designed so that there is a slow mode with high density of states at the GaAs bandedge at 870 nm. We put this photonic crystal on a thin 10 nm planar layer of the same material and calculate the LDOS as a function of position in the middle of the 10 nm plane. In Fig 3.4a it can be seen that there are significant LDOS enhancements at various positions throughout the structure. In Fig 3.4b we also show the spatial LDOS profiles for select wavelengths. It can be seen that at the bandedge and within the visible part of the spectrum there are significant LDOS enhancements and a suppression of the LDOS within the photonic bandgap starting at 870 nm.

In Fig. 2e we show the LDOS averaged over position for this structure. It exhibits an integrated LDOS enhancement relative to a GaAs film over the wavelengths of interest above the semiconductor bandgap.

Lastly, we point out that integrating solar cell absorber layers into an array of subwavelength scale optical cavities also offers a prospect of large LDOS and absorption enhancement beyond the ray optic limit. As an example, we calculate the LDOS within the gap of a metallic split dipole nanoantenna, shown in Fig. 3.2f. The LDOS enhancement is large and relatively broadband due to the hybridization of each of the monomer resonances and the low quality factor of the antenna. This structure allows for a large degree of tunability of the resonance wavelength, the LDOS peak enhancement and bandwidth by tuning the antenna length/diameter ratio as shown via FDTD simulations in Fig. 3.5. Of course, it is also possible to design all-dielectric cavities of this type which would eliminate any metallic losses.

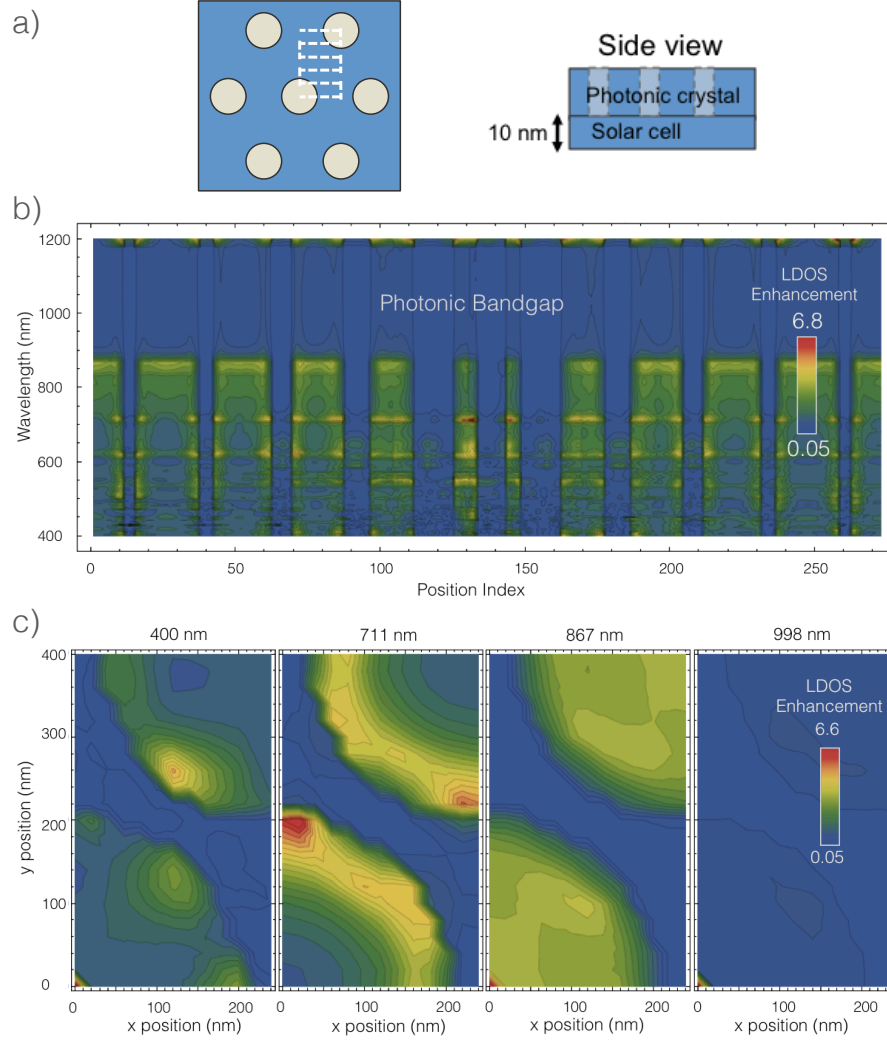


Figure 3.4: (a) LDOS map as a function of wavelength and position along the white dotted line shown within the schematic inset. (b) Spatial maps of the LDOS enhancement within the center of the 10 nm planar layer of dielectric at various wavelengths.

3.4 What Is The New Limit?

Figure 3.6 shows the density of states enhancement needed to absorb 99.9% of the solar spectrum for various thicknesses of Si and GaAs. For ultrathin layers we find that the density of states enhancement needed is very reasonable, especially in the context of the above results. It is thus possible to imagine absorbing nearly the entire solar spectrum with ultrathin layers of semiconductors as thin as 10-100 nm.

The most important criterion that gives an upper bound to the absorbance of a

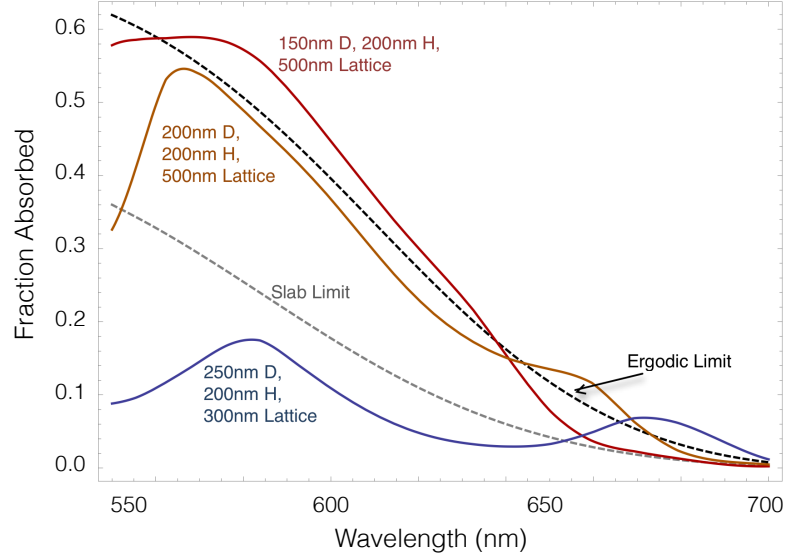


Figure 3.5: 3D FDTD calculated absorption spectra of a 10nm layer of P3HT:PCBM clad with various arrays of plasmonic Ag resonators. Depending on the resonator diameter (D), height (H) and lattice spacing, the ergodic limit can be exceeded over different portions of the spectrum.

solar cell absorber layer is the extent to which the density of states can be raised in the wavelength range where absorption is required, which is determined by the density of states sum rules [36, 37] which dictate that as the density of states is increased in a region of the spectrum, then it must decrease in another region of the spectrum so as to satisfy:

$$\int_0^\infty \frac{\rho_{cell} - \rho_{vac}}{\omega^2} d\omega = 0 \quad (3.12)$$

We show in Fig. 3.7 how this spectral reweighting could occur to allow a density of states enhancement in the desired region of the spectrum.

Spectral reweighting occurs naturally whenever a change in the density of states occurs, but can potentially be artificially engineered at will with clever tuning of dispersion using photonic crystals or metamaterials, for example. Thus the density of states could potentially be enhanced to a reasonably large value which is limited by the bandwidth of the spectral reweighting region as we will show.

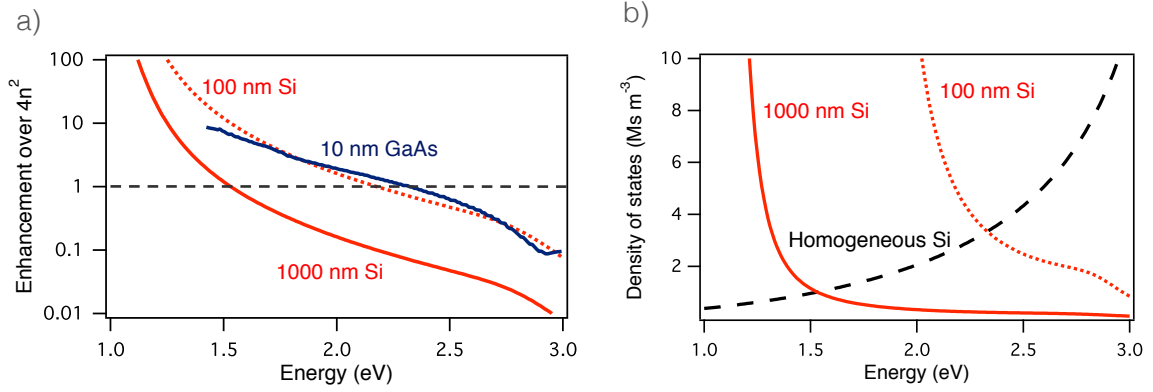


Figure 3.6: LDOS Enhancements needed to absorb the entire solar spectrum. (a) Absorption enhancement over $4n^2$ (proportional to LDOS enhancement over the homogeneous value) for various thicknesses of Si and GaAs needed to fully absorb the AM1.5 solar spectrum. (b) Needed density of states profiles for two thicknesses of Si needed to fully absorb the spectrum.

For a solar of material index n , absorption coefficient α , and thickness x , the density of states need to absorb all of the incident radiation is given by:

$$\rho_{max} = \frac{\rho_{bulk}}{1 - e^{-\alpha(4n^2)x}} \quad (3.13)$$

where $\rho_{bulk} = \frac{n^3\omega^2}{\pi^2c^3}$ is the homogeneous density of density of states of the bulk material.

If the cell is to absorb all of the incident light over the spectral range from ω_0 to ω_1 , e.g. over the solar spectrum, then over this range, $\rho_{cell} \rightarrow \rho_{max}$. By the sum rule, over some other spectral range, ω_2 to ω_3 , the density of states of the cell must be reduced. If n and α are approximately constant over the range ω_0 to ω_1 and n is constant over ω_2 to ω_3 , then the minimum bandwidth of the suppression region, $\omega_3 - \omega_2$, corresponds to:

$$(\omega_3 - \omega_2) = \frac{(\omega_1 - \omega_0)}{e^{-\alpha(4n^2)x} - 1} \quad (3.14)$$

Since the bandwidth of needed enhancement is limited (i.e. the solar spectrum)

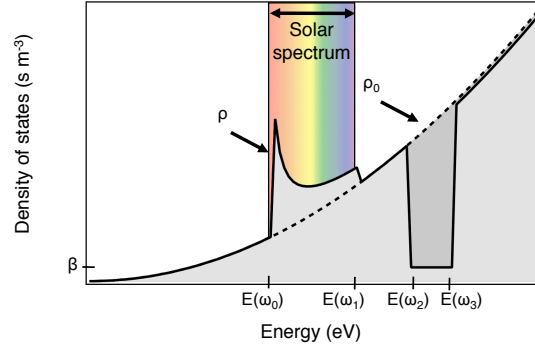


Figure 3.7: Schematic of spectral reweighting needed to achieve density of states enhancements.

and the region from which we can afford to decrease the density of states is nearly unlimited (i.e. regions outside of the solar spectrum), we expect other physical and practical limits to be relevant before a limit is reached for increasing the density of states, such as saturated absorption in the active layer or device and processing issues with extremely thin devices.

3.5 Numerical Demonstration Of Exceeding The Ray Optic Limit

As a simple proof-of-principle, we perform three-dimensional electromagnetic simulations using finite difference time domain methods for two test structures using the measured optical properties of real materials that demonstrate these concepts. Figure 3.8 shows the fraction of incident illumination absorbed by a 10 nm layer of P3HT:PCBM, a common polymeric photovoltaic material for both a dielectric slot waveguide (Fig. 3.8a) and a hybrid plasmonic structure (Fig. 3.8b).

For the slot waveguide, the P3HT:PCBM layer is cladded on both sides by 500 nm of roughened GaP, a high index material with little to no loss in the wavelength range of interest owing to its indirect bandgap at 549 nm. In this structure, the elevated

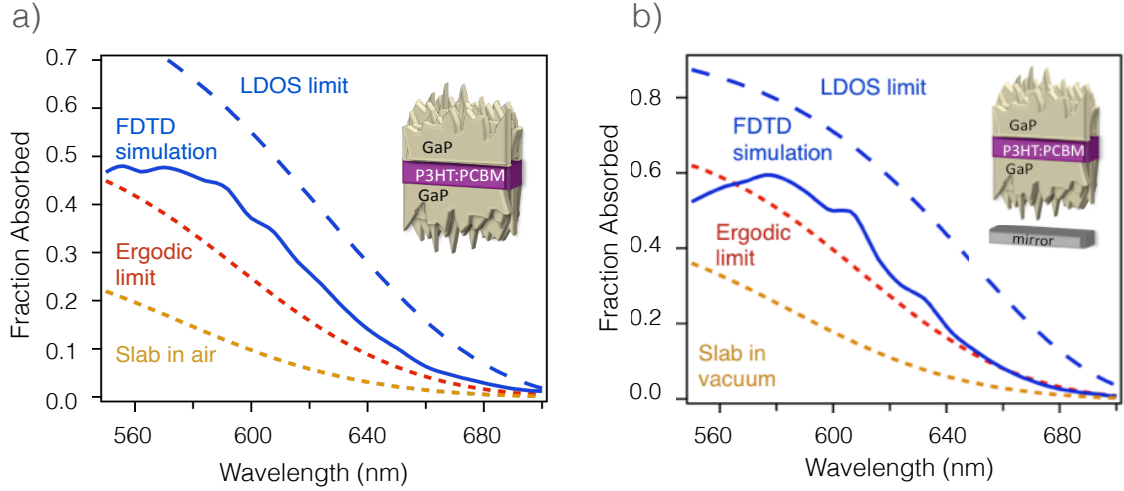


Figure 3.8: Full-wave simulations of a P3HT:PCBM structure cladded with roughened GaP (a) without and (b) with a back reflector that exceeds the ergodic limit. The absorption greatly exceeds the LDOS limit for the slab of P3HT:PCBM in air (dashed orange line) and approach the LDOS limit for the P3HT:PCBM slot (dashed blue line) with refined incoupling.

LDOS leads to an enhancement of the absorption that exceeds the ray optic light trapping limit even without full population of all of the modes of the structure at all wavelengths where the GaP cladding is transparent. This structure exceeds both the $4n^2$ and $2n^2$ limits for absorption enhancement, with and without a back reflector, respectively. Ideally, Lambertian scattering surfaces could be designed to allow more nearly equal incoupling to all of the modes, which will further enhance the absorption over the entire range of the spectrum to the new limit shown by the blue dashed line in Fig. 3.8a. We also calculate the LDOS limit for this slab in air (orange dashed line), which is exceeded by our simulation for all wavelengths.

The original ergodic limit calculation assumed isotropic illumination. Thus to truly exceed this limit a given design should have higher absorption when integrated over all angles. We thus calculate the angular response of the structure in Fig. 3.8 at two wavelengths to ensure the design truly exceeds the ergodic limit. Fig. 3.9 shows fraction of light absorbed at 550 and 600 nm as a function of angle of incidence, averaged over both polarizations. The ergodic limits are also shown for these two

wavelengths. The limit is exceeded for most angles for each of the wavelengths, falling off only at very steep angles as expected. The angle averaged absorbances for 550 nm and 600 nm light are 0.48 and 0.34, respectively, indicating that the ergodic limit is surpassed with this structure even with isotropic illumination.

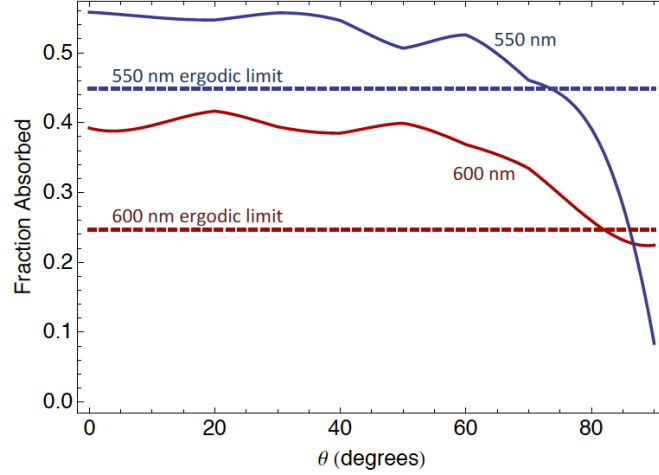


Figure 3.9: Angular behavior of the P3HT:PCBM structure that exceeds the ergodic limit.

Similarly, Fig. 3.10 indicates that plasmonic resonators situated above and below the absorber layer also enable absorption enhancements that surpass the ergodic limit. These two examples demonstrate that with proper design of LDOS and incoupling, the ergodic limit can be exceeded in several different ways.

We have identified the local density of optical states as a key criterion for exceeding the ray optic light trapping limit in solar cells. To exceed the ray optic limit, the absorber must exhibit a local density of optical states that exceeds that of the bulk, homogeneous material within the active region of the cell. In addition to this, the modal spectrum of the device must be appreciably populated by an appropriate incoupling mechanism. We have outlined a portfolio of solar absorber designs that can meet the LDOS criterion implemented utilizing plasmonic materials, dielectric waveguides, photonic crystals, and resonant optical antennas, and examples are given to show that incouplers can be designed that provide appreciable mode population.

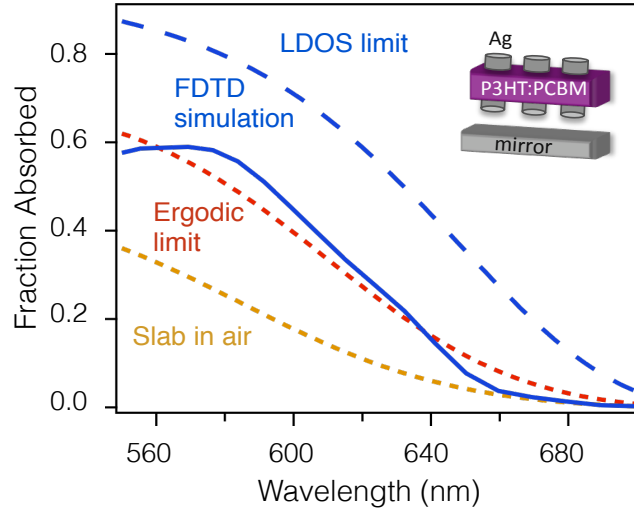


Figure 3.10: Full-wave simulations of a P3HT:PCBM structure cladded with plasmonic resonators with absorption enhancement exceeding the ergodic limit.

These concepts and design criteria open the door to design of a new generation of nanophotonic solar cells that have potential to achieve unprecedented light trapping enhancements and efficiencies.

3.6 Planar Waveguide Formulation for Exceeding The Ray Optic Limit

If we limit the scope of the previous section and consider only thin absorbing slabs (thickness, $h \sim \lambda$) that contain propagating modes, we can describe light trapping limits by extending a method initially developed by Stuart and Hall [30]. By considering the reduction in the number of photonic modes in an absorbing slab as the slabs thickness is reduced, they concluded that the maximum absorption enhancement is reduced below $4n^2$.

Despite the early work suggesting that the absorption enhancement in thin slabs is less than $4n^2$, recent work has shown that the enhancement may in fact exceed this limit through the use of photonic crystals [38], plasmonic waveguides [39], high

index claddings [25, 26], or an elevation of the local density of optical states [40]. Here we revisit the case of a thin waveguide and determine that the $4n^2$ limit can be exceeded for a number of structures that support large propagation constants and/or slow modal group velocities.

We follow a formalism similar to Refs [30, 39] and consider the thermal occupation of electromagnetic modes in a waveguide surrounded by vacuum. The total density of modes per unit volume and frequency is given by [30]:

$$\rho_{tot} = \rho_{rad} + \rho_m \quad (3.15)$$

where

$$\rho_{rad} = \left(1 - \sqrt{1 - \frac{1}{n_{sc}^2}}\right) \left(\frac{n_{sc}^3 \omega^2}{\pi^2 c^3}\right) \quad (3.16)$$

is the density of radiation modes not trapped by total internal reflection within a material of index n_{sc} , and

$$\rho_m = \frac{\beta}{2\pi h v_g^m} \quad (3.17)$$

is the density of waveguide modes with modal propagation constants β_m and group velocities v_g^m . Assuming that the modes of the structure are equally occupied from an appropriate incoupler, the total fraction of incident light absorbed by the film is [39]:

$$F_{tot} = \frac{\rho_{rad}}{\rho_{tot}} f_{rad} + \sum_m \frac{\rho_m}{\rho_{tot}} f_m \quad (3.18)$$

where

$$f_{rad} = \frac{\alpha}{\alpha + \frac{1}{4 \left(\frac{\rho_{tot} v_g^{rad}}{\rho_0 v_g^0} \right) h}} \quad (3.19)$$

and

$$f_{rad} = \frac{\alpha \Gamma_m}{\alpha \Gamma_m + \frac{1}{4 \left(\frac{\rho_{tot} v_g^{rad}}{\rho_0 v_g^0} \right) h}} \quad (3.20)$$

α is the attenuation coefficient, Γ_m is modal confinement factor, $\rho_0 = \frac{n_{sc}^3 \omega^2}{\pi^2 c^3}$ is the bulk density of states in vacuum, and $v_g^0 = c$ is the speed of light in the surrounding vacuum. We note that the ratios of the density of states gives the fraction of light that enters each mode and f_{rad} and f_m give the rate of absorption divided by the total rate of energy loss (absorption and out coupling).

We now consider the case of a thin waveguide that only supports one guided mode. For this case $\rho_{rad} \ll \rho_m$, and the total fraction of light absorbed can be approximated by:

$$f_{1-m} = \frac{\alpha \Gamma_m}{\alpha \Gamma_m + \frac{1}{4 \left(\frac{\rho_{tot} v_g^{rad}}{\rho_0 v_g^0} \right) h}} = \frac{\alpha \Gamma_m}{\alpha \Gamma_m + \frac{1}{4 \left(\frac{\beta_m \pi c^3}{2 \omega^2 h v_g^m n_{sc}} \right) h}} \quad (3.21)$$

which can be compared to the fraction of light absorbed in the traditional $4n^2$ limit [41]:

$$F_{4n^2} = \frac{\alpha}{\alpha - \frac{1}{4n_{sc}^2 h}} \quad (3.22)$$

In order to exceed the $4n^2$ limit, F_{1-m} must be greater than F_{4n^2} . With the condition $F_{1-m} > F_{4n^2}$, we obtain our central result:

$$\left(\frac{\beta_m}{k_0} \right) \left(\frac{v_g^{rad}}{v_g^m} \right) \Gamma_m > 4n_{sc} \left(\frac{h}{\lambda} \right) \quad (3.23)$$

Thus in order to surpass the $4n^2$ limit, we want well-confined modes ($\Gamma_m \sim 1$) that have large propagation constants ($\beta_m > k_0$), small group velocities ($v_g^m < v_g^{rad}$), and waveguide thicknesses that are small compared to the wavelength of the incident

light. By comparing Eq. 3.20 and 3.21, we note that the path length enhancement l_{path} is:

$$l_{path} = \left(\frac{c}{v_g^m} \right) \left(\frac{\beta_m}{k_0} \right) \left(\frac{h}{\lambda} \right) \Gamma_m \quad (3.24)$$

Note that the actual path length is $l_{path}h$ for the single mode waveguide case compared to $4n^2h$ for the traditional limit.

For a given waveguide structure, the dispersion relation is calculation to determine the modal parameters needed for Eq. 3.23. Figure 3.11 shows the dispersion relation for several structures based on a thin film of P3HT:PCBM, a common polymer solar cell blend. The propagation constants are obtained from the x-axis, and the slopes of the curves are proportional to the group velocities. Traditional photonic modes for the slab are confined to the region between the vacuum light line and the absorber light line (light blue region). In this region, $\beta_m < k_0$, $v_g^m > v_g^{rad}$, and $\Gamma_m \ll 1$ when the waveguide is thin. Thus, these photonic slab modes cannot surpass the $4n^2$ limit.

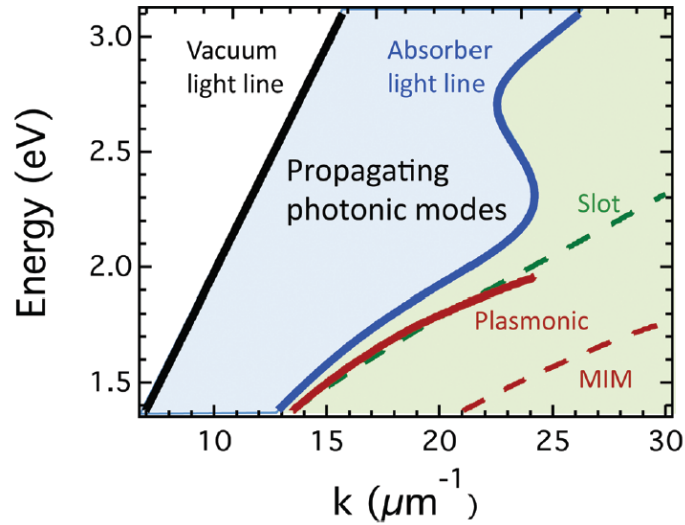


Figure 3.11: Waveguide dispersion relations. Plasmonic (solid red), Metal-Insulator-Metal (dashed red), and high-low-high index slot (green dashed) waveguides have dispersion relations that lie to the right of the bulk absorber light line (solid blue), which have large propagation constants, slow group velocities, and are well-confined.

Figure 3.11 also shows the dispersion relation for three structures that have large β_m , slow v_g^m , and large confinement factors. These structures include a surface plasmon polariton waveguide, a high-low-high index dielectric slot waveguide, and a metal-insulator-metal (MIM) waveguide. These dispersion curves represent the lowest order TM modes for the structures; however, higher order modes may exist depending on the thickness of the slab. While Eq. 3.23 is strictly valid only for a single, highly confined mode, the behavior of the fundamental mode typically dictates the absorption characteristics, as we shall see below.

A thin surface plasmon polariton waveguide (Fig. 3.12) satisfies the necessary conditions to surpass the $4n^2$ limit for a variety of wavelengths and slab thicknesses. Using Eq. 3.23, we find that the path length enhancement should exceed $4n^2$ for absorber thicknesses between 50-105 nm. However, the condition of only one well-confined mode in the structure is not met for thicknesses larger than 70 nm, because a second mode exists for larger slab thicknesses. Further, below 50 nm, the confinement factor is reduced. Figure 3.12a shows the actual absorption enhancement beyond $4n^2$ for $\lambda=580$ nm using Eq. 3.21, which takes into account both propagating and radiation modes. This structure surpasses the $4n^2$ limit for the entire range. The wavelength resolved absorption for a 50 nm thick slab of P3HT:PCBM on Ag is shown in Fig. 3.11b.

A high-low-high index dielectric slot waveguide is also found to exceed the $4n^2$ limit. This structure consists of a 10 nm P3HT:PCBM layer cladded on both sides by a 45 nm layer of GaP, a wide bandgap semiconductor with an indirect energy gap whose absorption is negligible over the wavelength region of consideration and whose real part of the refractive index exceeds that of P3HT:PCBM. This structure supports multiple modes; however we can use our expression for the path length enhancement to predict whether or not the structure could surpass the $4n^2$ limit if only one mode were present. Figure 3.13a shows that the lowest order TE and TM modes for $\lambda=580$

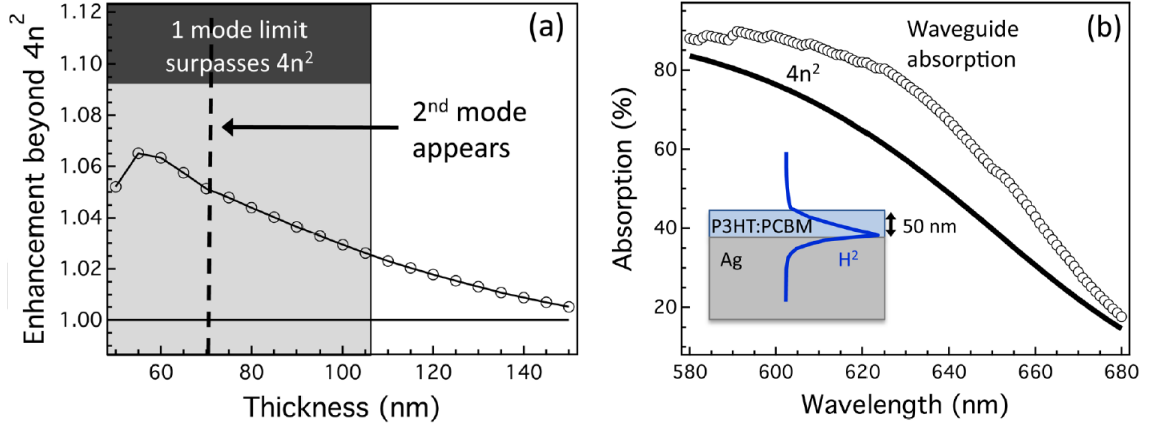


Figure 3.12: Plasmonic waveguides that beat the $4n^2$ limit. (a) Calculated absorption enhancement surpasses the $4n^2$ limit for a large range of thicknesses. Shaded region corresponds to the region where the limit is surpassed if only one mode were present. The appearance of a second mode (vertical dashed line) allows the absorption to surpass the $4n^2$ limit beyond the region predicted by the single mode model. (b) Plasmonic waveguide absorption surpasses the $4n^2$ limit throughout the useful absorbing spectrum of the polymer. Inset: Schematic of the plasmonic waveguide and the modal profile.

nm would both have path length enhancements in excess of $4n^2$ if this were a single mode waveguide.

Figure 3.13b shows the total absorption in the slot waveguide and the fraction of absorption coming from each of the modes. For wavelengths below 620 nm, there are three propagating modes; however, for longer wavelengths, there are only two modes since the second order TE mode is cut off. Because the cladding layer is thin, the radiation modes were assumed to be incident from vacuum and resulted in $< 1\%$ of the total absorption. If the radiation modes were allowed to occupy the full 4π steradians, ρ_{rad} would still contribute to less than 3% of the total absorption. Thus the main contribution to the absorption still comes from the propagating waveguide modes.

Finally, we explore a hybrid waveguide which combines the benefits of both a high index cladding and a plasmonic back reflector to achieve over 90% absorption in a 10 nm P3HT layerwell in excess of the $4n^2$ limit for bulk P3HT. The high index

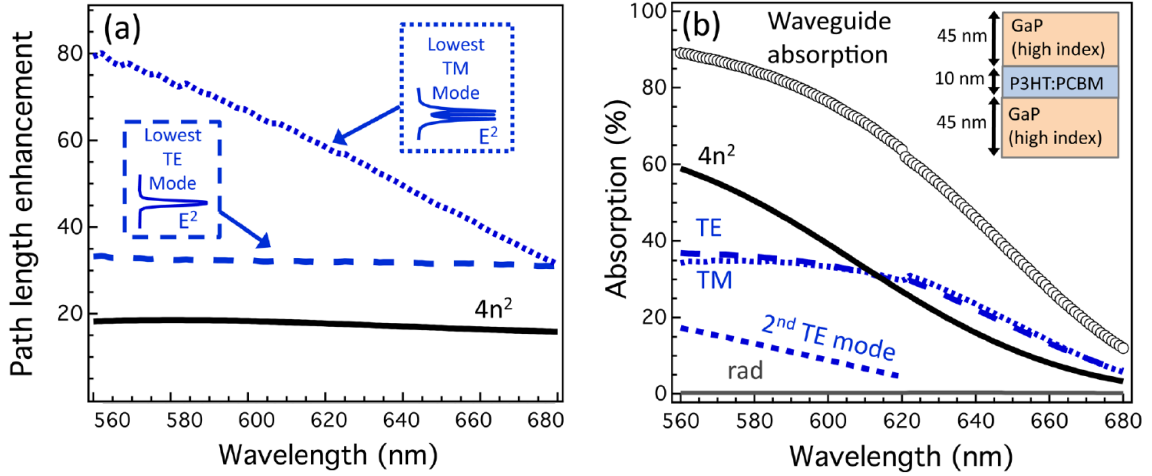


Figure 3.13: Slot waveguides that beat the $4n^2$ limit. (a) Path length enhancement if only one mode were present. Both the lowest TM and TE modes surpass $4n^2$. Insets: Mode profiles. (b) Modal decomposition of the absorbed fraction of the incident light. The total absorption surpasses the $4n^2$ limit. Inset: Schematic of the high-low-high index slot waveguide.

GaP cladding further confines the mode and reduces its group velocity. Figure 3.14 shows the total waveguide absorption, the absorption expected for $4n^2$ passes, and the absorption obtained by a 10 nm thick P3HT film surrounded by vacuum. Note that the 10 nm thick P3HT film in vacuum has a significantly lower absorption than would be expected by the $4n^2$ limit. This is due to the fact that the photonic modes are not well confined, have higher group velocities than do modes in the bulk, and have small propagation constants, which are in agreement with the conclusions of Ref. [30].

In summary, we have described a general method for predicting whether or not thin waveguides can have absorption enhancements in excess of the $4n^2$ limit based on their dispersion relations. We gave several examples of such structures by including plasmonic back reflectors and/or high index claddings in order to manipulate the modal propagation constant, group velocity, and confinement factor. Our results provide both a qualitative and quantitative design scheme for improving the light trapping in thin films, which is highly desired for solar cell applications.

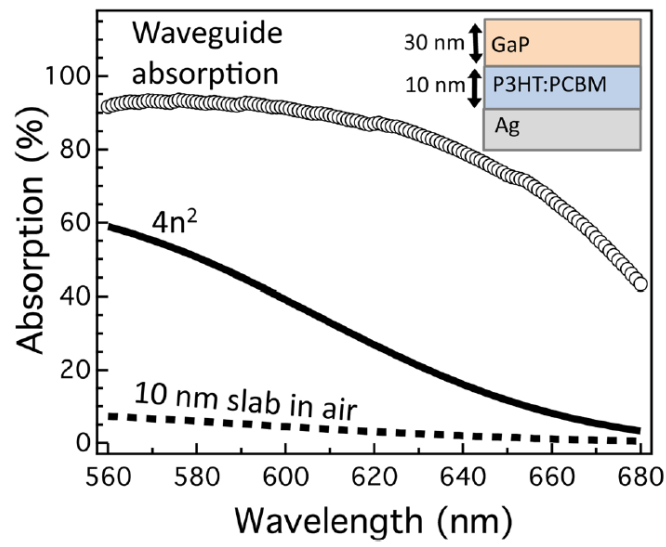


Figure 3.14: Absorption for a plasmonic waveguide cladded with a high index (GaP) top layer. Waveguide absorption (circles) is well in excess of the $4n^2$ limit (solid line) and the calculated absorption for a planar slab in vacuum (dashed line).

Chapter 4

Light Trapping With Dielectric Nanosphere Resonators

We have seen how various nanophotonic elements can act as useful tools to enhance optical absorption for photovoltaic devices. Here, we will examine in greater detail the behavior of a simple low cost, low loss scheme for absorption enhancement based on dielectric nanosphere resonators. The resonators can act as both scattering centers or as diffractive elements that change the momentum of incident photons and enables access of trapped modes in the absorbing layer. The periodic arrangement of the resonators allows for great flexibility for optical dispersion engineering and tuning of optical absorption for different materials applications. Here we show how this simple scheme can be applied to both traditional a-Si solar cell designs, as well as current thin-film GaAs solar cells. While neither of the two cases discussed here exceed the ergodic light trapping limit, further investigation with higher index resonators could potentially achieve this.

4.1 Dielectric Nanosphere Resonators for a-Si Absorption Enhancement

We propose here a light trapping configuration for a-Si solar cells based on coupling from a periodic arrangement of resonant dielectric nanospheres. It is shown that photonic modes in the spheres can be coupled into particular modes of the solar cell and significantly enhance its efficiency. We numerically demonstrate this enhancement using full field finite difference time domain (FDTD) simulations of a nanosphere array above a typical thin film amorphous silicon (a-Si) solar cell structure. The incoupling element in this design is advantageous over other schemes as it is composed of a lossless material and its spherical symmetry naturally accepts large angles of incidence. Also, the array can be fabricated using simple, well developed methods of self assembly and is easily scalable without the need for lithography or patterning. This concept can be easily extended to many other thin film solar cell materials to enhance photocurrent and angular sensitivity.

Thin film photovoltaics offer the potential for a significant cost reduction [11] compared to traditional, or first generation photovoltaics usually at the expense of high efficiency. This is achieved mainly by the use of amorphous or polycrystalline optoelectronic materials for the active region of the device, for example, a-Si. The resulting carrier collection efficiencies, operating voltages, and fill factors are typically lower than for single crystal cells, which reduce the overall cell efficiency. There is thus great interest in using thinner active layers combined with advanced light trapping schemes to minimize these problems and maximize efficiency.

Wavelength-scale dielectric spheres [42] are interesting photonic elements because they can diffractively couple light from free space and also support confined resonant modes. Moreover, the periodic arrangement of nanospheres can lead to coupling between the spheres, resulting in mode splitting and rich bandstructure [43, 44]. The

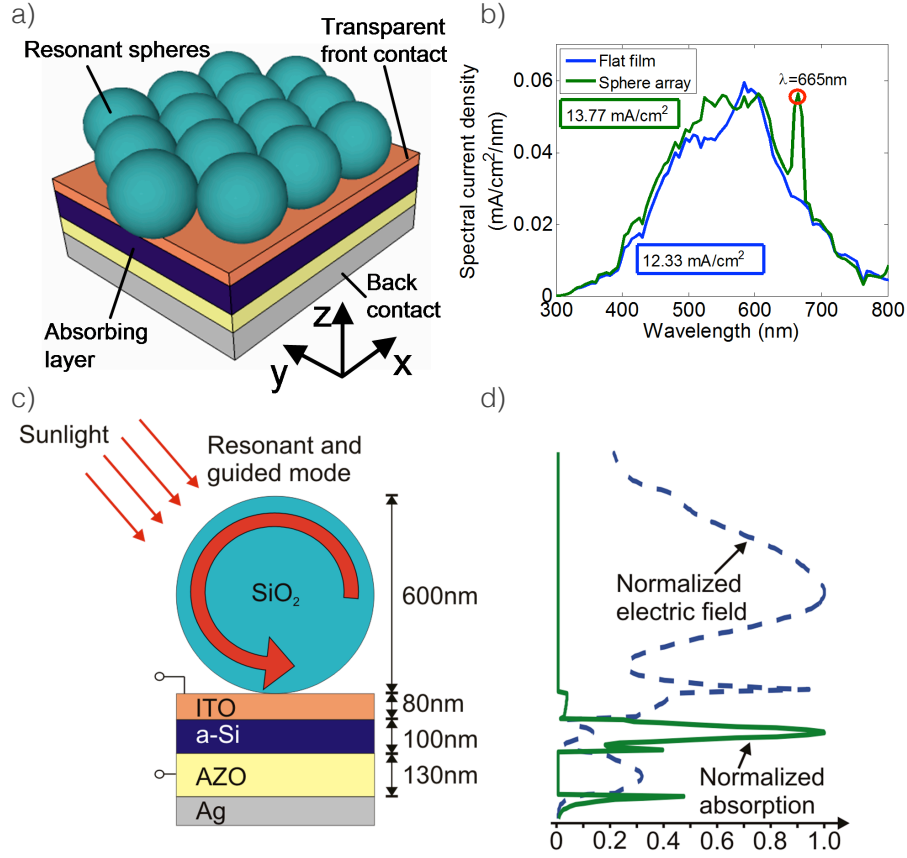


Figure 4.1: (a) 3D schematic of the dielectric nanosphere solar cell. (b) Current density calculated in the amorphous silicon layer with and without the presence of nanospheres. The a-Si thickness is $t=100$ nm and the sphere diameter is $D=600$ nm. (c) Cross section of a silica nanosphere on an amorphous silicon layer with an AZO and silver back contact layer. (d) Integrated electric field and absorption calculated from fig. 2(a) for normal incidence of a cross section at the center of the sphere at the resonant frequency $\lambda = 665$ nm.

coupling originates from whispering gallery modes (WGM) inside the spheres [44, 45]. When resonant dielectric spheres are in proximity to a high index photovoltaic absorber layer, incident light can be coupled into the high index material and can increase light absorption. Another important benefit of this structure for photovoltaic application is its spherical geometry that naturally accepts light from large angles of incidence.

Figure 4.1 (a) depicts a solar cell where close packed dielectric resonant nanospheres stand atop a typical a-Si solar cell structure. A cross section is represented in Fig. 4.1

(c). We use a silver back contact and, in order to avoid diffusion between the silver layer and the a-Si layer, a 130 nm aluminium-doped zinc oxide (AZO) layer is placed between the silver and the a-Si layer [46]. An 80 nm indium tin oxide (ITO) layer is used as a transparent conducting front contact and also acts as an anti-reflection coating. 600 nm diameter silica nanospheres with a refractive index of $n=1.46$ are directly placed on the ITO as a hexagonally close packed monolayer array.

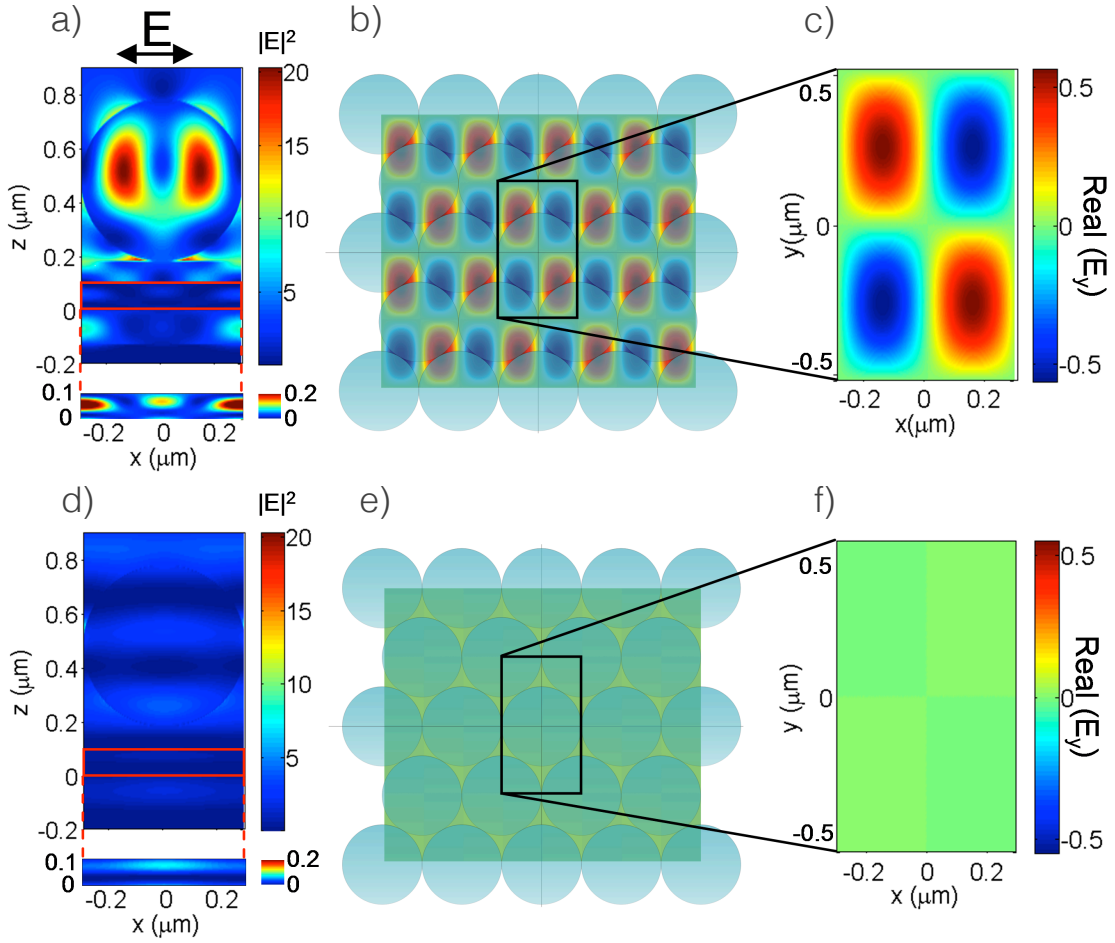


Figure 4.2: (a) Electric field intensity for a cross section at the middle of a sphere in the (x,z) plane at $\lambda=665$ nm. Below is a zoom of the a-Si layer. The direction of the electric field of the incident plane wave is also represented. (b,c) E_y component of the electric field from a cross section in the (x,y) plane in the middle of the a-Si layer. (d,e,f) Same as (a,b,c) for $\lambda=747$ nm which corresponds to a frequency off resonance.

In order to study the response of the system, we perform three-dimensional full

field electromagnetic simulations to determine the expected absorption enhancement compared to a-Si absorbers without a layer of dielectric spheres. A broadband wave pulse with the electric field polarized along the x axis [see Fig. 4.1(a)] is injected at normal incidence on the structure, and the fields are monitored at 100 wavelengths equally spaced between $\lambda=300$ nm and $\lambda=800$ nm. This wavelength range corresponds to the sun's energy spectrum below the bandgap of a-Si. In order to determine how much current can be generated from the structure, we calculate the optical generation rate in the silicon by [47]:

$$G_{opt}^n(\omega) = \int \frac{\epsilon''(\omega)|E(\omega)|_s^2}{2\hbar} \Gamma_{solar}(\omega) dV \quad (4.1)$$

where ϵ'' is the imaginary part of the dielectric function of the silicon and $|E(\omega)|^2$ is the electric field intensity integrated over the simulation volume containing the amorphous silicon [48]. If all electrons generated are collected, this will correspond to the device's short circuit current. Γ_{solar} is a factor used to weight each wavelength by the AM1.5 solar spectrum. In Fig. 4.1 (d), we plot the normalized integrated electric field and absorption of a cross section at the center of the sphere perpendicular to the incoming plane wave and in the plane of the electric field for the resonant frequency $\lambda=665$ nm. The absorption is proportional to $\epsilon''|E(\omega)|_s^2$ as shown in Eq. 4.1.

To compare the influence of the spheres on the solar cell structure presented in Fig. 4.1 (a), we calculate the spectral current density in the a-Si layer with and without the presence of 600 nm diameter nanospheres. The result is presented on Fig. 4.1 (b). The overall integrated current density corresponding to the energy absorbed in the a-Si in the presence of the nanospheres is $J=13.77 \frac{mA}{cm^2}$, which corresponds to an enhancement of 12% compared to the case without the sphere array. Over almost the entire wavelength range, the spectral current density is higher with the spheres than without the spheres, while the narrow band response is due to a coupling between the spheres and the solar cell. Furthermore, there exists discrete enhancements at specific

wavelengths. The broadband enhancement can be explained by the spheres acting as an anti-reflection coating. At $\lambda=665$ nm, the enhancement is greater than 100%. To explain this increase in the current density, we plot in Fig. 4.2 (a) the electric field intensity for a cross section in the middle of a sphere in the (x,z) plane. Two lobes are observed on each side of the sphere. These are characteristic of WGMs. They have significant field strength within the periodic arrangement of the sphere layer.

The WGMs of the spheres couple with each other due to their proximity [49], which can lead to waveguide formation [43].

We represent in Fig. 4.2 (b) and (c) the E_y component of the electric field for a cross section in the (x,y) plane in the middle of the a-Si layer. The observed field profile is periodic and oscillates in phase with the period. Because the sphere array by itself has very low loss, the mode energy eventually gets absorbed into the a-Si and increases the generated photocurrent. In Fig. 4.2 (c), we show the E_y component of the electric field, corresponding to a TE guided mode along the x axis. There also exists a TM guided mode of the same periodicity that contributes to the enhancement of the absorption at $\lambda=665$ nm (not shown). As a comparison, we show in Fig. 4.2 (d,e,f) an equivalent analysis, off resonance at $\lambda=747$ nm. Clearly there is no resonance in the sphere and no excitation of a guided mode at this wavelength.

The spherical shape of the structure above the solar cell also enables incoupling at large angles of incidence. In order to verify this, we compared the absorbed light at normal incidence and at 20° and 40° angle to the normal in both TE and TM polarizations. For simplicity, we considered only an array of silica spheres above a 100 nm a-Si layer. Figure 4.3 (a) and (d) show a schematic of the simulated structures without and with silica spheres on top of the a-Si. Figure 4.3 (b), (c), (e) and (f) correspond to the spectral current density in the a-Si for both cases without and with silica spheres respectively, and for TE and TM polarizations. For normal incidence, the calculated improvement is 29.6% and is independent from the

polarization. This high improvement compared to the solar cell previously described can be explained by the absence of an antireflection coating layer and back reflector layer in this simplified case. For TM polarization, the improvement is 13.8% for 20° and 3.9% for 40° incidence angle. For TE polarization, the improvement compared to a flat layer remains around 29% for all angles. However, in the case of a TM polarization, for a flat a-Si film, the larger the angle, the larger the energy absorbed. That is why the current improvement of a structure with spheres decreases over that of a structure without spheres in the case of a TM-polarized plane wave.

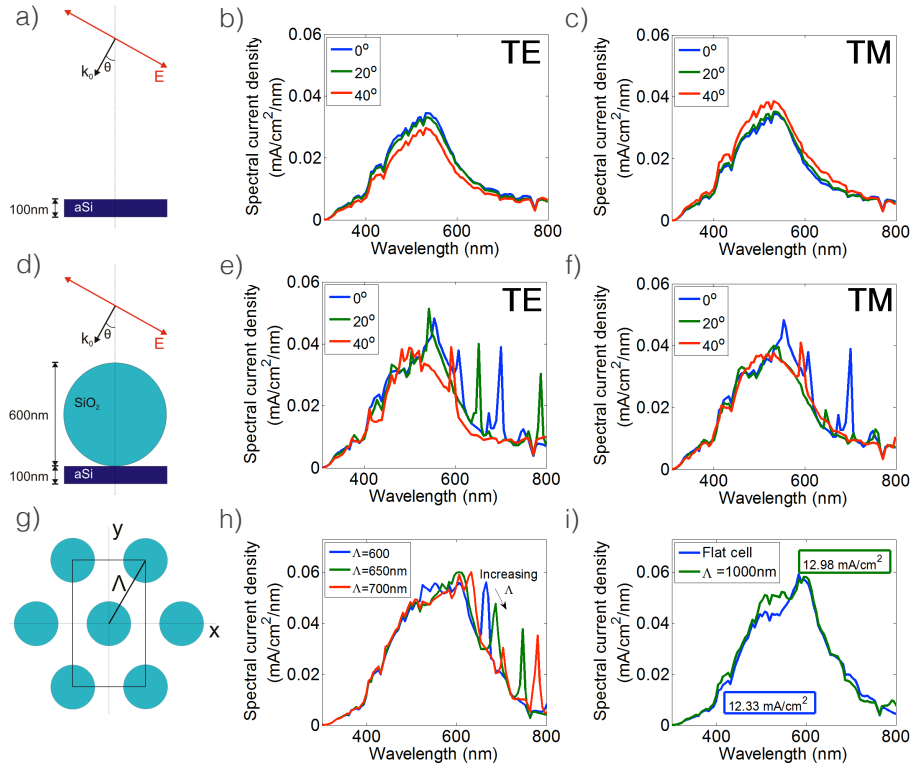


Figure 4.3: (a) Schematic of the flat case model with an angle and spectral current density in (b) TE and (c) TM polarization. (d) Schematic of the case with nanospheres on top and spectral current density in (e) TE and (f) TM polarization. (g) Top view of the periodic arrangement of the nanospheres with a large lattice constant. The rectangle indicates the periodicity used for numerical simulations. (h) Current density for three different sphere spacings where an efficient coupling between the spheres exists. (i) Current density for a flat cell and with a relatively large distance between the spheres.

As the lattice constant of the hexagonal array of spheres varies, as represented in

Fig. 4.3 (g), the efficiency of the WGM guided wave changes due to different coupling conditions between the spheres. In Fig. 4.3 (h), we show the spectral current density for different spacings between the spheres. The peak at $\lambda=665$ nm for close packed spheres is shifted to longer wavelengths as the distance between the spheres increases. This provides evidence that the incoupling is due to a diffractive mechanism. For $\Lambda=650$ nm and $\Lambda=700$ nm, a second peak appears at $\lambda=747$ nm and $\lambda=780$ nm, respectively. This corresponds to an optimal coupling condition between the WGM and the a-Si waveguide mode for these specific periodicities and wavelengths. For the considered design, a separation of $\Lambda=700$ nm gives the highest current density with $J=14.14 \frac{mA}{cm^2}$ which represents an enhancement of 15% compared to a flat a-Si cell with antireflection coating. As shown on Fig. 4.3 (i), when $\Lambda > 1000$ nm, the coupling between the spheres almost disappears and the enhancement significantly decreases. From an experimental point-of-view, a close packed configuration is more feasible than a hexagonal one. However, the spacing between spheres could be varied by an additional coating on each sphere or by assembly on photolithographically patterned substrates [50]. An intriguing aspect of changing the spacing between the spheres is that it allows one to tune and adjust which wavelengths are coupled into the solar cell. This, coupled with the option of using different sphere sizes in a single array could potentially allow for broadband enhancement.

In order to estimate the influence of the sphere diameter on the enhancement of the solar cell efficiency, we represent on fig. 4.4 the ratio between the spectral current density of a solar cell with close packed spheres over the spectral current density of a solar cell without spheres. The sphere diameter varies between $D=100$ nm and $D=1000$ nm. We can observe a general broadened enhancement due to the additional anti-reflection coating made by the spheres. Moreover, strong discrete enhancement lines also appear. These correspond to the WGMs at certain wavelengths. Since the a-Si absorption becomes weaker over $\lambda= 600$ nm, the enhancement corresponding to

the WGMs becomes significant over this wavelength. This strong enhancement where a-Si is weakly absorbing is obtained for sphere diameters between 500 nm and 900 nm. Therefore, a way to broadly enhance the a-Si absorption in this weakly absorbing region could be to randomly mix sphere diameters in the range 500 to 600 nm.

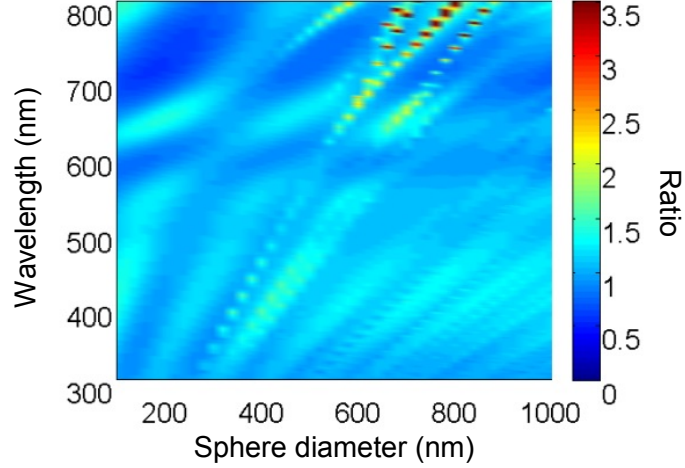


Figure 4.4: Ratio between the spectral current density of a solar cell with spheres over the spectral current density of a solar cell without spheres. Spheres are close packed.

We have investigated several photovoltaic absorber configurations based on a periodic array of resonant silica nanospheres atop an a-Si layer and demonstrated that strong whispering gallery modes can significantly increase light absorption in a-Si thin film solar cells. We presented here a new concept for a solar cell where a resonant guided mode is excited due to a nanosphere array above the active layer and eventually absorbed in the a-Si under it. We optimized the structure design for the largest absorption enhancement for a given sphere diameter. The spectral position of the absorption enhancement can be easily tuned by varying the sphere diameter and lattice constant. Also, the number of resonances can potentially be increased to make the response more broadband by assembling arrays of spheres with different diameters [51]. This concept has advantages over other absorption enhancement schemes because the incoupling elements are lossless and their spherical geometry

allows light to be efficiently coupled into the solar cell over a large range of incident angles. Also these arrays can be fabricated and easily scaled using standard self assembly [45, 52] techniques without the need for lithography. In addition to this, the presented enhancement results are performed on a totally flat a-Si layer which has an advantage over cells grown on textured surfaces as surface roughness or topography can create holes, oxidation and thus reduce the efficiency and lifetime of the solar cell. The sphere array can also be easily integrated or combined with existing absorption enhancement techniques. This light trapping concept offers great flexibility and tunability and can be extended for use with many other thin film solar cell materials.

4.2 Dielectric Nanosphere Resonators for GaAs Absorption Enhancement

The route to more than 30% single junction solar cell efficiency requires the short circuit current J_{sc} , the open circuit voltage V_{oc} , and the fill factor FF to be near their theoretical maximum values. The current single junction solar cell record at 1 sun illumination is 28.2% [15], which is for a GaAs cell. While it is unclear whether the current losses are from absorption or collection, investigating all optical methods to maximize the absorption is of great importance. Additionally, reducing the amount of material is necessary for reducing both the cost and weight of the cell, which requires advanced light trapping strategies as the active layer thinned [11].

Thin film photovoltaics offer the possibility to significantly reduce the cost of a solar cell compared to first generation solar cells, usually at the expense of efficiency. It is therefore of great interest to combine thin film absorbing layers with advanced light trapping schemes to reduce the cost without reducing the efficiency. Light trapping is a critical requirement in thin film photovoltaics, and dielectric texturing is a viable method to induce light trapping [19], but for some materials thin film device quality

often suffers upon direct texturing of the semiconductor active region. Texturing the active layer increases the path length of the incident photons and increases their probability to be absorbed, but it can be at the cost of limiting the solar cell's lifetime caused by faster cell degradations. It can also reduce the electrical properties of the solar cell by adding surface recombination. Thus it is desirable to develop a simple, scalable design method in which textured dielectric layers provide for light trapping on smooth, planar thin film cells.

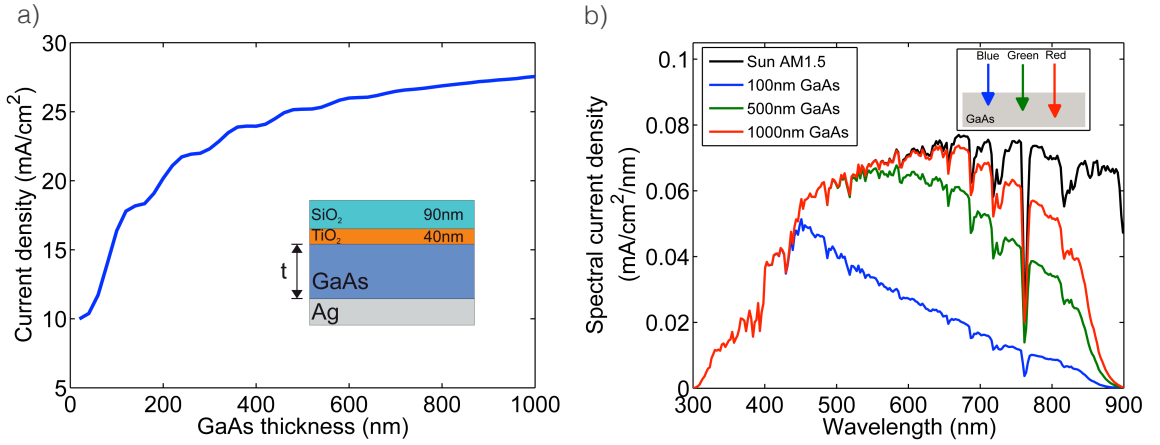


Figure 4.5: (a) Current density of a flat GaAs solar cell with back reflector and double anti-reflection coating as a function of the GaAs thickness. (b) Calculated spectral current density for different GaAs layer thicknesses. The spectral range is weighted by the solar spectrum and compared with the AM1.5 solar spectrum.

We propose here an approach for coupling light into smooth untextured thin film solar cells [45] of uniform thickness using periodic arrangements of resonant dielectric nanospheres deposited as a continuous film on top of a thin cell. It is shown that guided photonic modes in the spheres [44] can be coupled into particular modes of the solar cell and significantly enhance its efficiency by increasing the fraction of incident light absorbed [53]. We numerically demonstrate this enhancement using full field finite difference time domain (FDTD) simulations of a silicon dioxide (SiO₂) nanosphere array above gallium arsenide (GaAs) solar cells featuring back reflectors and double anti-reflection coatings. The incoupling element in this design has ad-

vantages over other schemes as it is a lossless dielectric material, and its spherical symmetry naturally accepts a wide angle of incidence range. Moreover, analytical models show that for nanospheres of a given dielectric material, a large number of resonant modes can be supported, which can give rise to a 11% absorption enhancement in a 100 nm thick GaAs absorber layer at several wavelengths between 300 nm and 900 nm and 2.5% enhancement in the case of a 1000 nm thick GaAs absorber layer. Also, the SiO₂ nanosphere array can be fabricated using simple, well developed self assembly methods and is easily scalable without the need for lithography or patterning. This concept can be easily extended to other thin film solar cell materials, such as silicon or copper indium gallium diselenide (CIGS).

We demonstrated previously the use of dielectric nanospheres for solar applications in the case of a thin film amorphous silicon solar cell [53]. GaAs is the semiconductor whose absorption is best matched with the solar spectrum [54] and which currently has the world record for single junction solar cell efficiency at 1 sun illumination [15]. Moreover, it has already widely been investigated in several configurations [55, 56]; therefore, we extend the concept of using dielectric nanospheres to a GaAs solar cell. We numerically demonstrate the optimal sphere size and spacing to achieve the highest possible photocurrent density for several thicknesses of GaAs solar cells with a double antireflection coating and a hexagonally close packed array of silica spheres.

We first consider a GaAs solar cell with a 40 nm thick titanium dioxide (TiO₂) and 90 nm thick silicon dioxide (SiO₂) double layer antireflection coating and a silver back reflector. A broadband wave pulse with the electric field polarized along the x-axis is injected at normal incidence on the structure, and the fields are monitored at 300 wavelengths equally spaced between $\lambda = 300$ nm and $\lambda = 900$ nm. This wavelength range corresponds to the sun's energy spectrum below the bandgap of GaAs. The optical generation rate in the GaAs is calculated using [48]:

$$G_{opt}^n(\omega) = \int \frac{\epsilon''(\omega)|E(\omega)|_{GaAs}^2}{2\hbar} \Gamma_{solar}(\omega) dV \quad (4.2)$$

where $|E(\omega)|_{GaAs}^2$ is the electric field intensity integrated over the GaAs volume [48] and ϵ'' is the imaginary part of the dielectric function of the GaAs. Γ_{solar} is a factor used to weight each wavelength by the AM1.5 solar spectrum. We represent in Fig. 4.5a the current density of a flat GaAs solar cell with back reflector and double anti-reflection coating as a function of the GaAs thickness. The current density considerably increases within the first five hundred nanometers. This shows that most of the light is absorbed within this range. For a 500 nm thick GaAs solar cell, we calculate a current density of $25.19 \frac{mA}{cm^2}$. Then, above 500 nm, the current density slowly increases to reach $27.56 \frac{mA}{cm^2}$ for a 1000 nm thick GaAs solar cell. This value corresponds to 82% of the maximum attainable value. Even though this value is high, it still gives potential for improvement.

We present in Fig. 4.5b the AM1.5 solar spectrum and plots that indicate the fraction of the solar energy absorbed in three thin GaAs layers on a single pass. The current density is calculated by $J = G_{ana}^n(\omega)e^-$ where e^- is the elementary charge and

$$G_{ana}^n(\omega) = \alpha(\omega)N_0 \int e^{-\alpha(\omega)x} dx \quad (4.3)$$

is the analytically calculated optical generation rate. N_0 is the sun photon flux at the top of the GaAs layer and $\alpha(\omega) = \frac{4\pi k}{\lambda}$ where k is the imaginary part of the refractive index. Figure 4.5b gives us an indication of where in the spectral range there exists potential for improvement to increase the absorption in a GaAs absorbing layer for the three considered thicknesses. Clearly, a large fraction of the solar spectrum is poorly absorbed, especially in the 600 - 900 nm spectral range for the case of a 1000 nm thick GaAs absorbing layer. Thus, a way to increase the absorption in this

particular wavelength range will have a direct influence on the solar cell's efficiency. We develop in the next section a way to significantly increase the light absorption in the weakly absorbing part of a GaAs solar cell by using the modes of a dielectric nanosphere monolayer array.

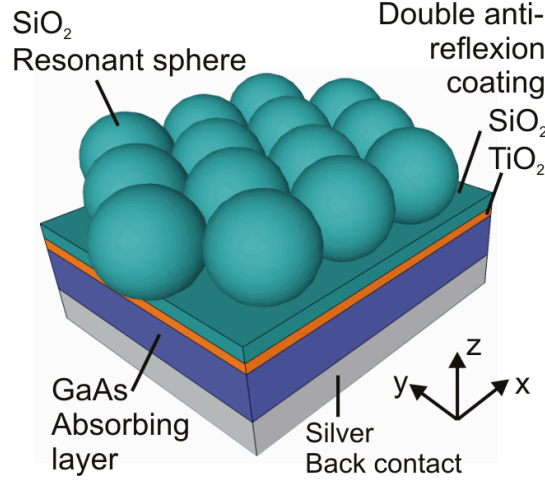


Figure 4.6: Schematic of a GaAs solar cell with hexagonally close packed SiO_2 nanospheres on top of it.

In order to estimate the influence of a hexagonally close-packed monolayer array of dielectric nanospheres atop the flat GaAs solar cell (Fig. 4.6), we perform 3D FDTD electromagnetic simulations to determine the expected absorption enhancement. A schematic of the cross section is represented in Fig. 4.7a. In Fig. 4.7b, we compare the expected spectral current density in the case of a flat GaAs solar cell and a cell with a hexagonally close-packed monolayer array of 700 nm dielectric nanospheres for a 100 nm thick GaAs solar cell. The dip between 450 nm and 600 nm wavelength is due to Fabry-Prot interference in the flat region of the solar cell. The dip appears in an off-resonance range where the influence of the spheres is negligible. That's why a similar dip mainly influenced by the flat region of the solar cell can be seen both with and without the sphere array.

We labeled several peaks corresponding to different mode orders in the nanospheres

[45] above the solar cell. For the case represented in Fig. 4.7d, the enhancement due to the sphere's whispering gallery mode is more than 300%. Because in the near infrared part of the solar spectrum GaAs is weakly absorbing, we are able in this case, due to the monolayer spheres array, to enhance the generated current density by more than 11%.

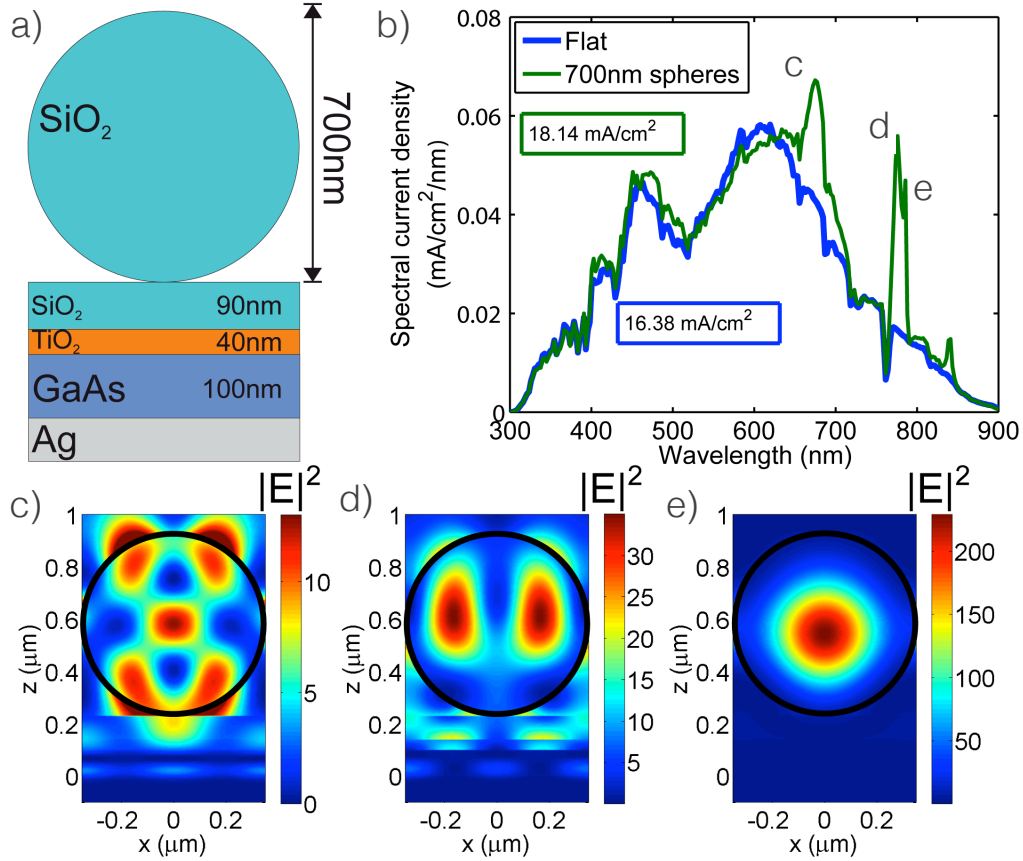


Figure 4.7: (a) Cross section of a silica nanosphere on a flat GaAs solar cell with back reflector and double layer anti-reflection coating. (b) Spectral current density of a 100 nm thick GaAs flat cell and a cell with a hexagonally close-packed monolayer array of 700 nm diameter dielectric nanospheres. Each peak labeled (c), (d) and (e) correspond to different whispering gallery mode orders where we show the electric field intensity for a cross section at the middle of a sphere at different wavelengths for the labeled peaks. The E field of the initial plane wave is oriented in the (x,z) plane. The black circles show the contour of the sphere.

In Fig. 4.8a, b, c, we illustrate the ratio between the spectral current density of a solar cell with hexagonally close packed spheres over the spectral current density of a

solar cell without spheres for three different thicknesses of GaAs: 100 nm, 500 nm and 1000 nm, respectively. The spheres' diameter varie between $D=100$ nm and $D=900$ nm. Strong enhancement occurs corresponding to optical dispersion of the array of coupled whispering gallery mode dielectric spheres. In Fig. 4.8d, e, f, we plot the current density as a function of the sphere diameter for the same GaAs thicknesses previously described. In the case of the 100 nm thick GaAs solar cell, the highest current density is obtained for 700 nm diameter spheres and equals $J=18.14 \frac{mA}{cm^2}$ (see Fig. 4.8d). In the case of a flat GaAs solar cell, the same current density would be obtained for a 160 nm thick GaAs solar cell, which means that in this particular case, it is possible to save 37.5% of the active material to obtain the same amount of current density.

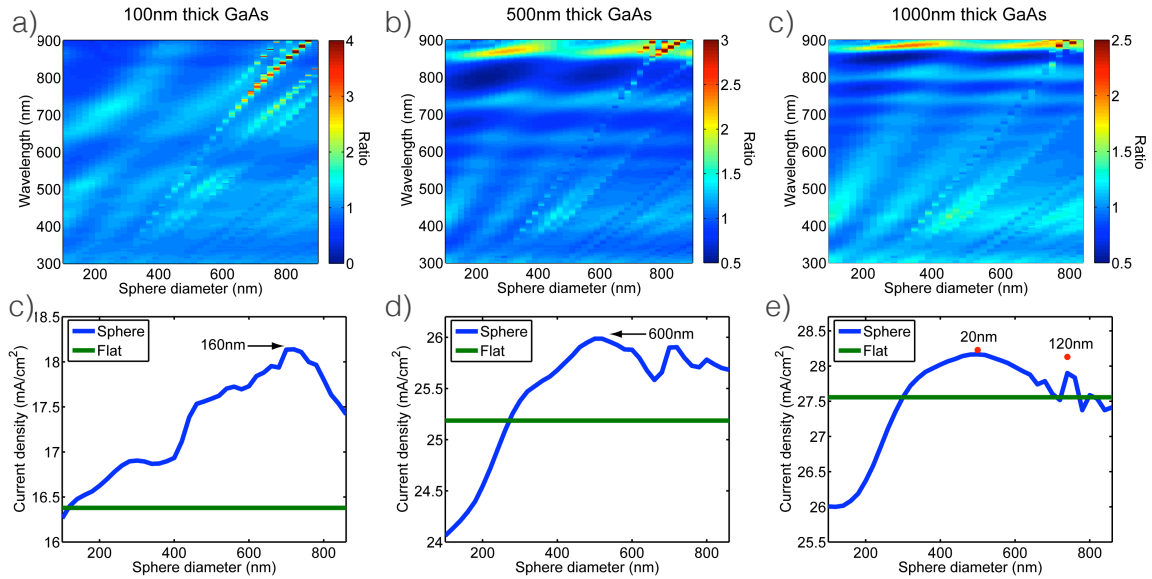


Figure 4.8: Ratio between the spectral current density of a solar cell with hexagonally close packed spheres over the spectral current density of a solar cell without spheres for a (a) 100 nm, (b) 500 nm and (c) 1000 nm thick GaAs solar cell. (d,e,f) Current density of a solar cell as a function of the sphere diameter above it. The current of the equivalent flat cell is also represented. On (d) and (e) is represented for the highest value obtained with sphere what thickness of an equivalent flat GaAs solar cell would be. On (f), the red dots show the value for the written spacing between the spheres.

In Fig 4.8a, the enhancement due to the sphere array clearly appears in the range

between 700 nm and 900 nm wavelength where the enhancement lines directly refer to the mode orders. In the case of the 500 nm thick GaAs solar cell, the highest current density is obtained with 500 nm diameter hexagonally close packed nanospheres on top of it and equals $J=26.00 \frac{mA}{cm^2}$. This corresponds to a 3.2% enhancement compared to a flat GaAs solar cell with double antireflection coating where the current density equals $J=25.19 \frac{mA}{cm^2}$. Note that, as shown in fig. 4.8e, in order to obtain the same current density with a flat GaAs solar cell, we would have need 600 nm of active material. For the case of the 1000 nm thick GaAs solar cell, the highest current is obtained for $D=500$ nm diameter spheres and is equal to $J=27.41 \frac{mA}{cm^2}$ (see Fig. 5f). Some enhancement for subwavelength diameter spheres is also seen, probably due to scattering effects [42]. There is still room for improvement for each of these cell thicknesses as the currents are not yet at the maximum attainable value, even for the 1000 nm thick cell. The current densities can potentially be increased further by utilizing spheres of multiple diameters, partially embedding the spheres or texturing the underlying AR coatings. On a given peak resonance, the absorption is also influenced by the distance between the sphere array and the GaAs layer. Therefore, there exists an optimal distance between the sphere array and the absorbing layer which can be tuned for maximizing the absorption related to each independent peaks due to the sphere modes. However, modifying the distance between the spheres and the absorbing layer means to modify the double antireflection coating thickness and potentially degrade the performance of the cell off resonance. If we slightly tune the spacing between the spheres to $a=20$ nm, it reaches $J=28.23 \frac{mA}{cm^2}$ which corresponds to an enhancement of 2.5% compared to a flat solar cell with double antireflection coating. As we can see on Fig. 4.7, the enhancement occurs mainly at wavelength scale diameter spheres where low order whispering gallery modes occur. In the case of 740 nm diameter nanospheres, we can show that by tuning the spacing to $a=120$ nm between the spheres, we can increase the spectral current from $J=27.90 \frac{mA}{cm^2}$ for

a hexagonally close packed array of nanospheres to $J=28.13 \frac{mA}{cm^2}$. This represents an enhancement of 2.0% compared to a flat solar cell with double antireflection coating. While this enhancement is less than shown earlier for the case of the 500 nm diameter sphere array with 20 nm spacing, a part of the enhancement occurs near the band edge, which may be beneficial for thin cells. This improvement due to the spacing is detailed on Fig. 4.9. At $\lambda=870$ nm, there exists a mode with an effect that can be significantly enhanced with the spacing between the nanospheres as it can be seen on Fig 4.9b. In order to understand this enhancement, we plot on Fig. 4.9c the field profile of a cross section at the middle of a sphere in the (x,z) plane at $\lambda=870$ nm for a hexagonally close packed array of nanospheres and compare it with the case where the spheres are $a=120$ nm away from each other. It appears that this separation results in a greater coupling between the array of spheres and the active material. This is most likely due to a better coupling between the spheres themselves as the field profile suggests.

We demonstrated light absorption enhancement on a 100 nm, a 500 nm and a 1000 nm thick GaAs solar cell structure featuring a back reflector, a double layer anti-reflection coating, and a close packed silica nanosphere array. The thinner the cell is, the more potential for improvement. We could see the highest improvement of 11% for the 100 nm GaAs solar cell by adding 700 nm hexagonally close packed SiO_2 nanospheres on top of it. We could see that depending on the size of the spheres, the enhancement we obtain occurs on different parts of the spectrum. Therefore, the best current densities are obtained where nanosphere array modes enhance the weakly absorbing region of the active material. By optimizing the sphere size and spacing, we showed an improvement of 2.5% in the current generation for the case of a 1000 nm thick GaAs solar cell. As we also showed the overall absorption enhancement obtained with thinner absorbing layers, around 100 nm, is much greater. In the case of a 1000 nm thick GaAs solar cell, because the initial absorption is very high for the

considered flat structure, the improvement using a single size nanosphere structure is much less; however, there is still improvement potential in the range 800 - 900 nm, leading to total absorbed currents close to the maximum attainable value.

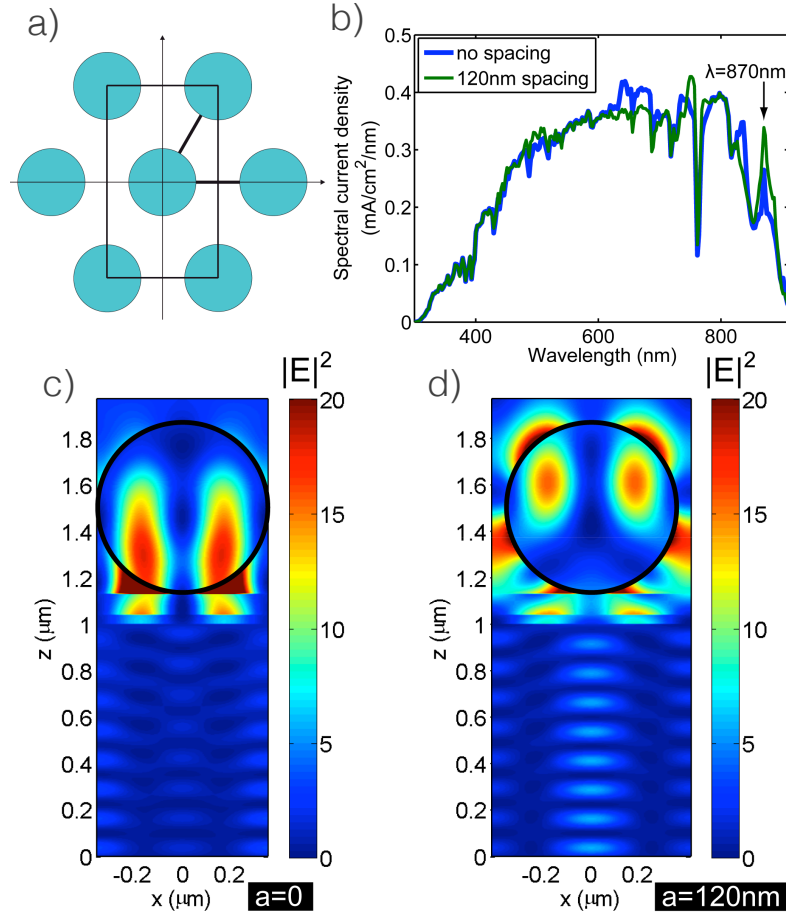


Figure 4.9: (a) Top view of the periodic arrangement of the nanospheres with a spacing between them. The rectangle indicates the unit cell used for numerical simulations. (b) Comparison of the spectral current density of a 1000 nm thick GaAs flat cell in the case where 740 nm nanospheres are hexagonally close packed and in the case where there is an $a=120$ nm gap between them. (c,d) Corresponding field profile at the resonant wavelength $\lambda=870$ nm. The black circles show the contour of the sphere.

Chapter 5

Light Trapping In Ultrathin Film Si With Photonic Crystal Superlattices

5.1 Introduction

The cost per watt of photovoltaic modules has been steadily decreasing due to increased manufacturing capacity. Currently, the cost of the wafer is one of the dominant expenses for a photovoltaic cell, and thus engineering efficient thin film devices has the potential to significantly reduce cost. Inherently, the short collection lengths in thin film devices can lead to improved open circuit voltage and relaxed material constraints in cells with very low surface recombination velocities. However, thin films suffer from poor light absorption, and advanced light trapping strategies are required for these cells to achieve reasonable efficiencies and competitive cells.

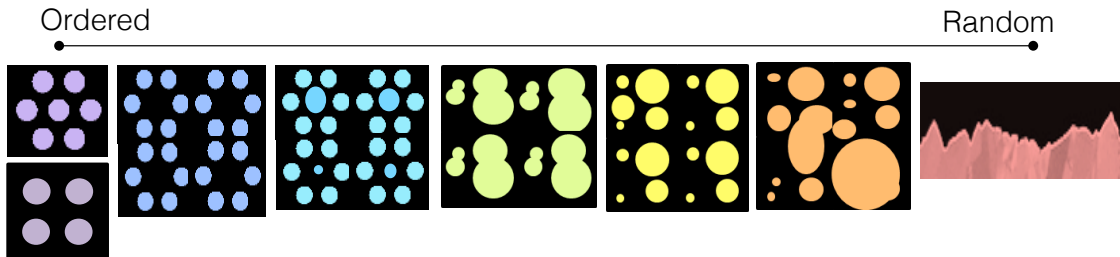


Figure 5.1: Conceptual diagram illustrating a range of possible light trapping structures incorporating different degrees of randomness and order.

Nanostructured photovoltaics are an attractive possible solution to this problem. Texturing the active layer of a solar cell on a wavelength scale has recently been shown to have potential to exceed the traditional ray optic light trapping limit [25, 40]. This is due to the fact that a properly nanostructured device can have an elevated local density of optical states (LDOS) throughout the absorber region, increasing the light matter interaction and allowing the possibility for more energy to be coupled into the solar cell where it can be absorbed. There are numerous ways to nanostructure a photovoltaic absorber layer that have been explored recently including the use of nanowires [20, 21], nanospheres [53], nanodomes [57], photonic crystals [58, 59], and plasmonic structures [11]. While it has been shown in numerous publications [25, 26, 40] that the ray optic limit can be exceeded in low index polymer materials, it is much more challenging to achieve maximum light trapping in thin films of high index materials such as Si, where more work is needed.

A major open question in nanophotonic light trapping is whether periodic, aperiodic or a random texturing is optimum [60–62]. There are many different ways to explore the design space between periodic and random, including adding randomness to the absorber, incoupler, or both. Previous work has focused on tuning disorder in the absorber. In one study, a random walk algorithm was used to optimize the lattice positions of Si nanowires, and it was found that aperiodic lattices outperformed periodic ones [63]. Further studies proved that too much randomness decreased absorption [64]. Recent work with air holes in thin Si slabs has also shown that a proper degree of randomness designed using structural correlations outperformed an uncorrelated random lattice [65].

We approach this question by considering separately the two most important factors regarding light trapping [19, 40]: incoupling and the density of optical states. An optimal light trapping structure will have a large density of optical states within the absorber, as well as the ability to fully populate all of the optical modes of the

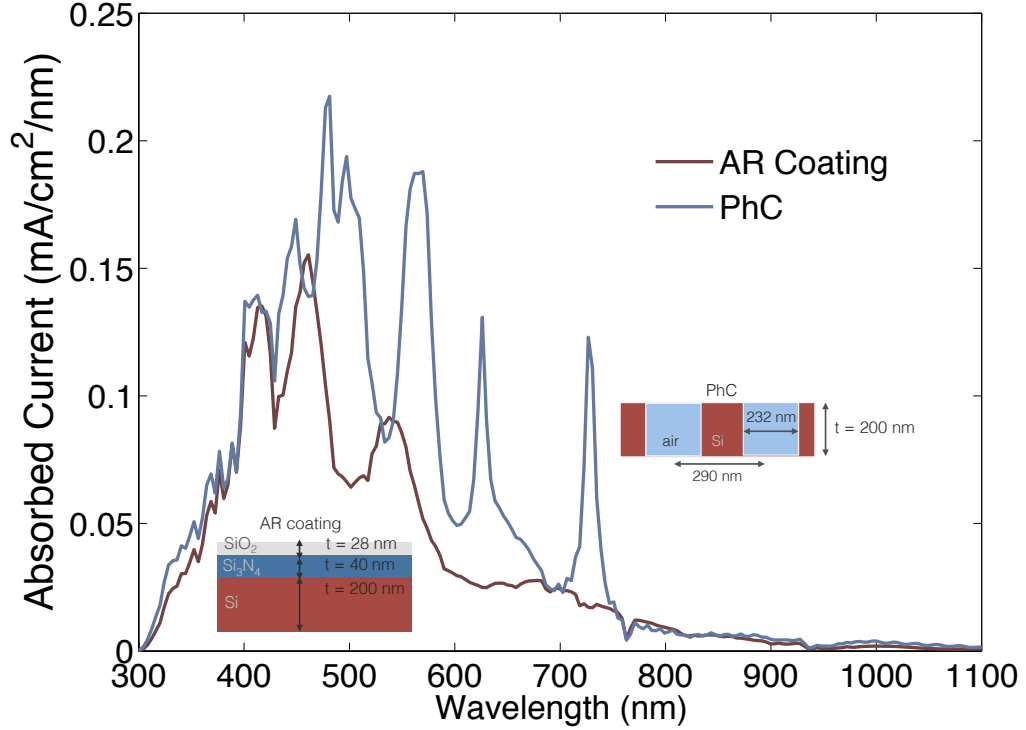


Figure 5.2: Absorption spectrum of a planar Si layer with a two-layer AR coating of SiO_2 and Si_3N_4 , optimized for thickness, compared to that of a rectangular lattice photonic crystal ($r = 116\text{nm}$, $a = 290\text{nm}$) of the same thickness.

device (i.e. maximize the modal occupation number for each mode). Traditionally, for a bulk absorbing material, the optimal light trapping structure has been a random, Lambertian surface [19]. In this case the density of optical states has been assumed to be that of a homogeneous material with a given refractive index. For a thin film, nanophotonic solar cell, though, this is no longer the case. The density of optical states can actually be increased above that of the bulk, homogeneous value, and thus the limits to absorption can potentially be larger in a nanophotonic solar cell compared to those of a traditional, bulk cell. However, optimal incoupling becomes an issue with thin devices as typical Lambertian texturing is usually not possible because it typically requires fabrication of features larger than the thickness of the cell.

Wavelength-scale periodic structures can take advantage of the inherent increases

in the density of optical states associated with the periodicity [29], but always come with a significant angular tradeoff that limits the population of optical modes to those which conserve momentum. Ideal random texturing will allow full population of optical modes at all incident angles, but typically does not increase the density of optical states. We have begun exploring these concepts using as a test system a silicon photonic crystal slab that is a weakly absorbing material. We suggest that the optimal light trapping structural motif may exist between the two extremes of perfectly periodic and fully random structures, for the reasons discussed above. This is shown schematically in Figure 5.1.

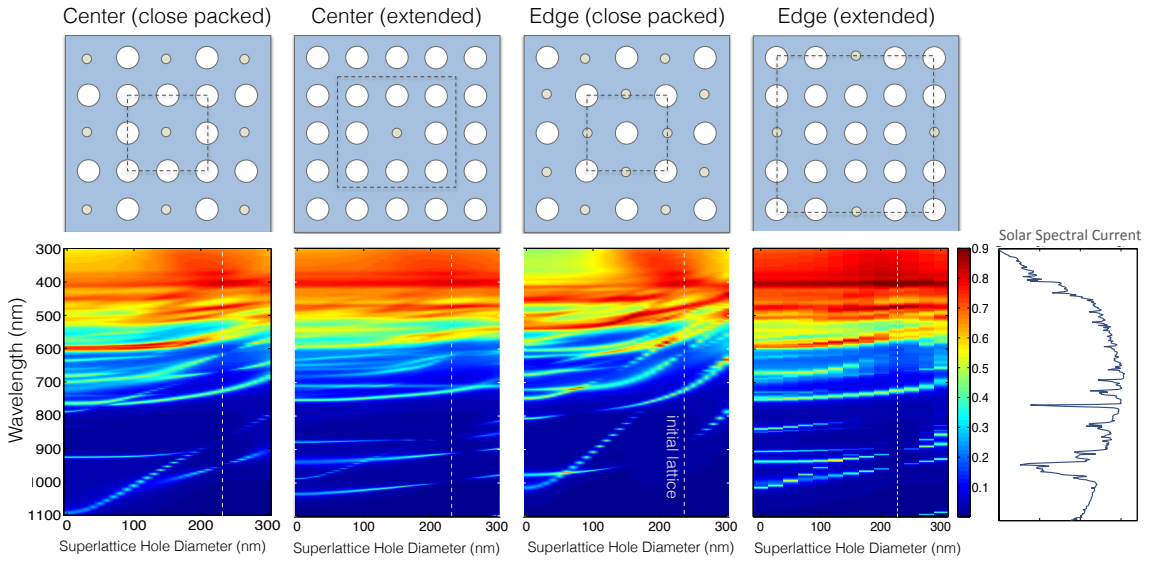


Figure 5.3: Four different superlattice geometries (top) and their spectral absorption as a function of superlattice air hole diameter (bottom). For reference, the vertical dotted white lines indicate when the superlattice air hole diameter is the same as the background lattice air hole diameter (i.e. no superlattice).

In this work, we begin with simple periodic two-dimensional slab photonic crystals and begin to add more complexity to them by adding sublattices of defects to form 2D photonic crystal superlattices (not to be confused with superlattices of layered semiconductor materials sometimes used in solar cells). This is an initial step away from the leftmost extreme case shown in Figure 5.1. These structures perturb the

initial periodicity of the traditional photonic crystal structures and introduce new modes into the slab. These modes can act as either localized, isolated resonator modes or as delocalized, Bloch modes formed by infinite coupling of single resonators [44, 66]. Some lattices of this type have been investigated for use in various nano-optics applications such as photonic crystal lasers [67], but not for solar cells. We find that many different superlattice configurations lead to increased absorption compared to simpler photonic crystal lattices. Lastly, for the first time we combine roughened or random surfaces with photonic crystals with optimized superlattices to obtain a synergistic effect.

5.2 Superlattices In A Square Photonic Crystal

Let us first consider a simple square lattice of air holes in Si with $a = 290\text{nm}$ and $r = 116\text{ nm}$. We first calculated the normal incidence absorption spectra for this structure and integrated over the AM 1.5 spectrum to obtain an absorbed current. Our calculations are done using rigorous coupled wave analysis (RCWA) using the RSoft DiffractMOD software package and are supported with finite difference time domain (FDTD) calculations using the Lumerical software package.

The normal incidence absorption spectra is shown in Figure 5.2. Shown for comparison are the absorption spectra for a 200 nm slab of planar Si with and without an optimized 2-layer anti-reflection coating. It is interesting to note that even this lattice, which is not optimized, has significantly higher absorption than equivalent thickness planar layers. This simple photonic crystal lattice has a few peaks of high absorption as well as broad wavelength ranges in the solar spectrum where absorption is very weak. The broader peaks are due to Fabry-Perot modes related to the thickness of the slab and the narrower peaks are due to coupling to gamma-point modes of the photonic crystal bandstructure, their number and position dictated by momen-

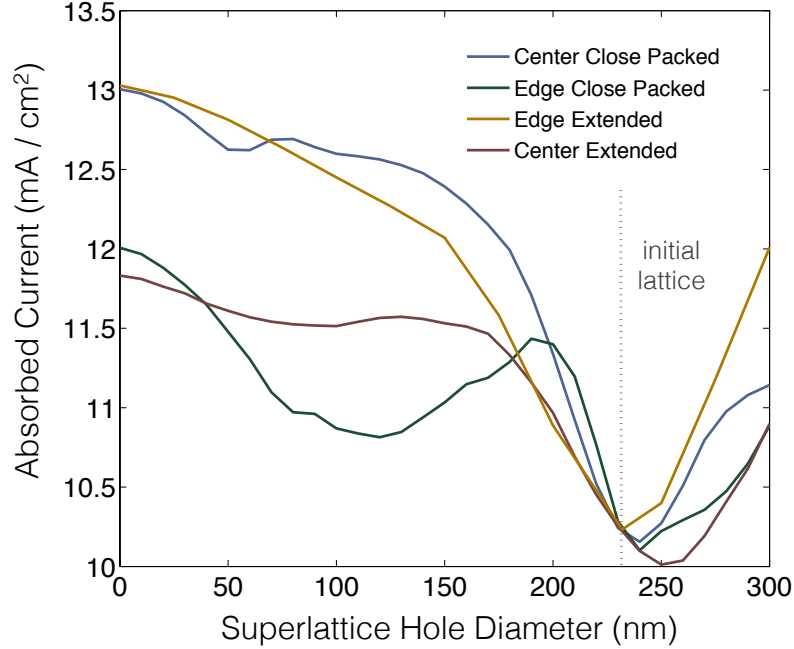


Figure 5.4: Absorbed current as a function of superlattice air hole diameter for four different configurations obtained by integrating the spectral absorption data in Fig. 5.3 and weighting by the AM 1.5 solar spectral current.

tum conservation. In the regions where there are no peaks, the lack of absorption is due to either a lack of available optical modes at those frequencies or the inability to couple to these modes from free space, due to momentum conservation. In the present work, we aim to increase the number of these absorption peaks by modifying the original lattice with superlattices of different configurations.

There are numerous ways to introduce superlattices into this structure. We explore four different superlattices which we term center close-packed, center extended, edge close-packed, and edge extended as shown in Figure 5.3. The terminology is based on the placement and spacing of the defects that are introduced to the background lattice. We vary the diameter of the air holes at the superlattice positions and plot the spectral absorption in Figure 5.3. For reference, on each of these plots is a vertical dotted white line corresponding to the case when the superlattice air hole diameter is the same as the background lattice (i. e. when the structure is just the original,

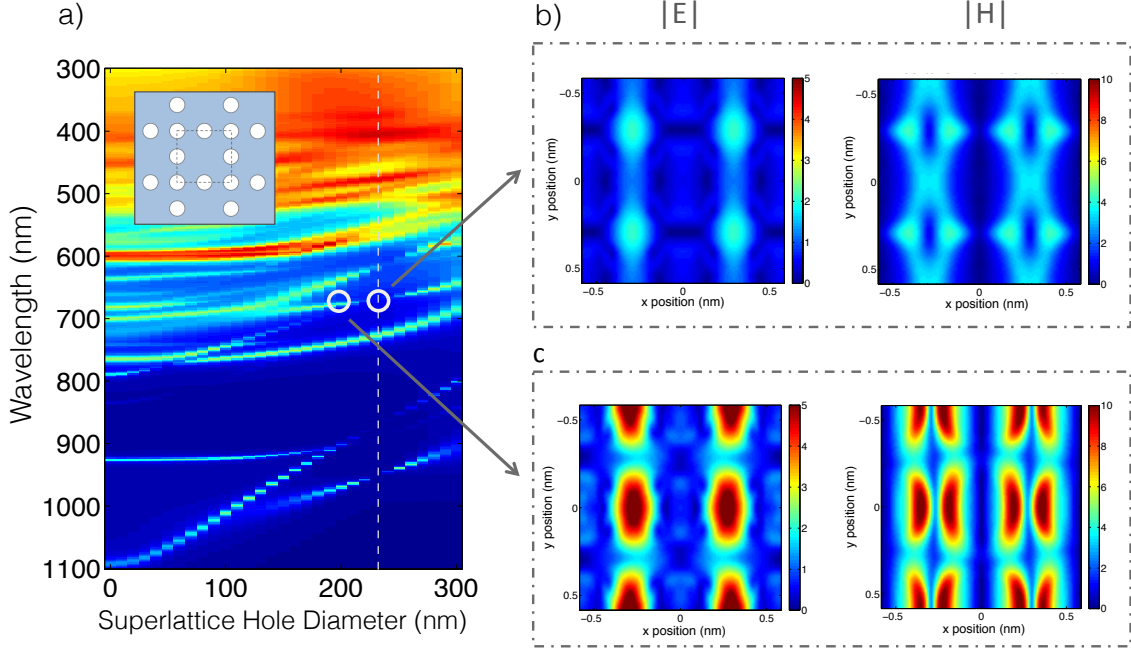


Figure 5.5: Field profiles (E-field polarized along y direction) for a wavelength of 678nm for (b) the original lattice and (c) the center close-packed superlattice. The field intensities are much higher for the superlattices, leading to increased absorption. The shape of the field profiles is also different in each case, suggesting the introduction of new optical modes through the addition of a superlattice.

unperturbed lattice). For each of these superlattices, it can be seen that as soon as the superlattice air holes are different from the background lattice new resonances appear in some regions of the spectrum.

When these absorption spectra are integrated and weighted by the solar spectral flux, we obtain values for total absorbed current as a function of superlattice air hole diameter, shown in Figure 5.4. It can be seen that for nearly every defect size in each of the four defect configurations the absorbed current is higher than the original lattice. This corresponds well with the observation of new resonances being introduced when the original lattice is perturbed. The overall absorbed current is a complicated function of where each resonance is introduced into the spectrum and how much current is available in each region. It is interesting to note that for most superlattice diameters the absorbed current increases, but for some diameters

it decreases. This is a complicated function of the nature of the newly introduced modes, where their electric fields are concentrated, Si filling fraction, etc. For each of these lattices, the most resonances and highest integrated absorption occurs for a defect diameter of zero, or when there is no air hole at all at the superlattice locations.

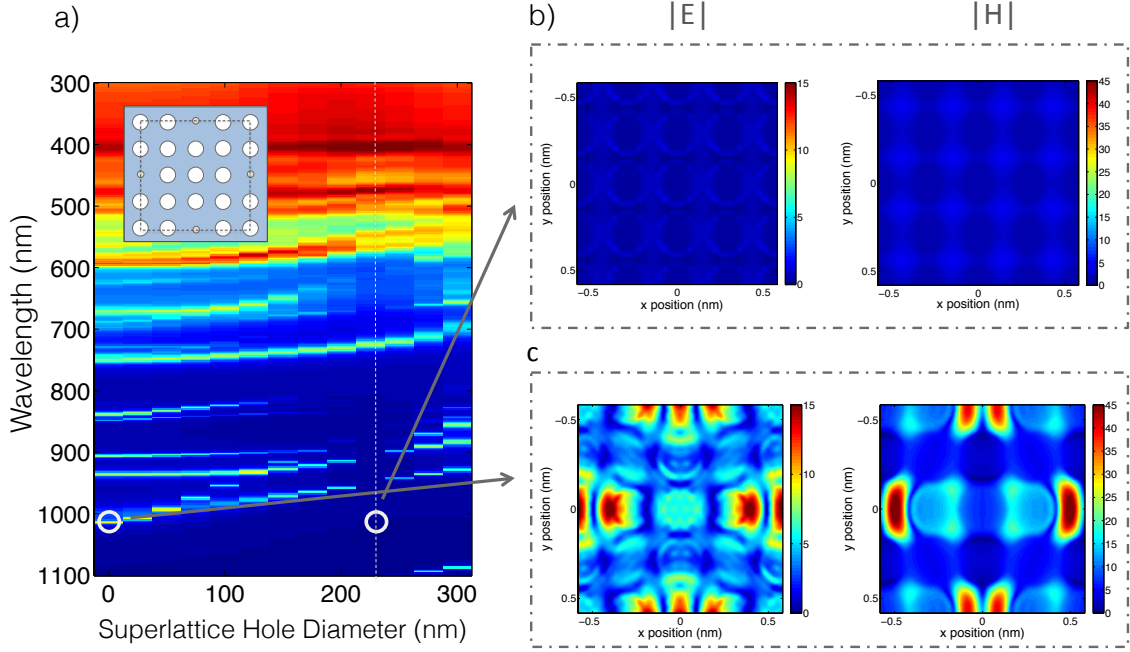


Figure 5.6: Field profiles (E-field polarized along y direction) at a wavelength of 1010nm for (b) the original lattice and (c) the edge-extended superlattice. In this case, the localized field profiles suggest that the new modes of the superlattice act more like isolated resonators.

To examine the absorption enhancement in further detail, we first take the center close-packed lattice with an air hole diameter of 0 nm and plot field profiles in Figure 5.5. Figure 5.5b shows the electric and magnetic field magnitudes at a wavelength of 678 nm for the original, unperturbed lattice. For comparison, the field magnitudes are also shown in Figure 5.5c for the same wavelength with slightly smaller diameter (190 nm) air holes in the superlattice. There is a significantly higher field magnitude for both the electric and magnetic components, as well as different field profiles. The altered field profiles suggest that new optical modes are introduced by the presence of the superlattice. The increased field magnitude leads to the higher absorption than

the case without the superlattice. Also worth noting with these field profiles is the fact that the new modes appear to be extended modes rather than isolated defect resonances. This is likely as the locations of the new defect air holes are reasonably close, and any mode that would exist inside one of these holes would couple with a neighboring mode, forming a periodic set of coupled resonators analogous to the tight binding description of bound states in solid-state physics.

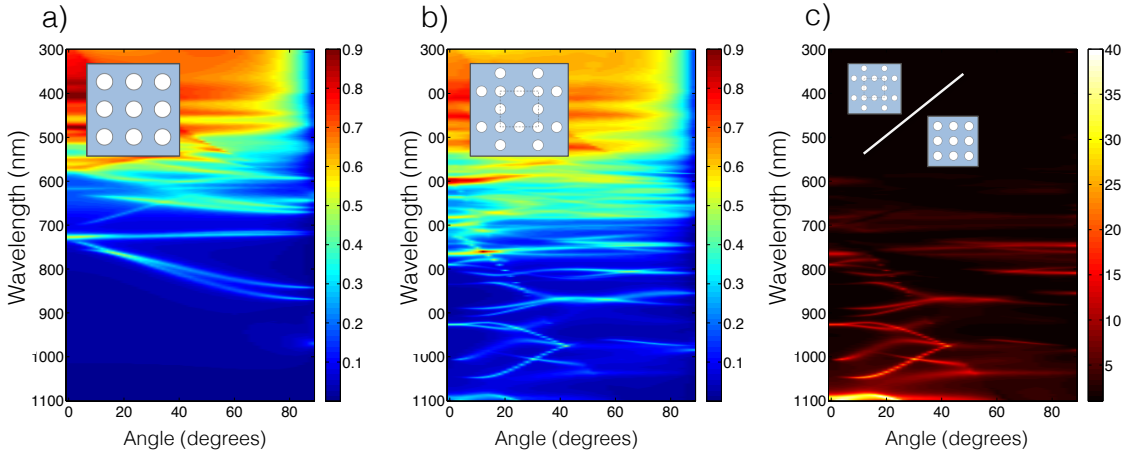


Figure 5.7: TE-TM averaged angular absorption spectra for (a) the original lattice, and (b) the center close-packed superlattice. (c) Absorption enhancement ratio obtained by dividing spectra (a) by spectra (b).

Next we examine field profiles from a lattice that has a larger separation between superlattice points, the edge extended lattice. Figure 5.6 shows field profiles for modes at a wavelength at 1010 nm with a superlattice air hole diameter of 0 nm and for the original lattice. Again, it can be seen that the field magnitudes are much higher for the case with the superlattice, leading to the higher absorption at this wavelength. The field profiles are also very different for each case. Here, the fields for the superlattice case are more isolated than for the center close-packed lattice, acting more like weakly interacting resonators. This is because the superlattice positions are separated by a larger distance and their resonant field profiles overlap less with neighboring resonators.

In Figure 5.7 we compare the TM-TE averaged angular spectra for the original lattice and the angular spectra for the center close-packed superlattice that has a superlattice air hole diameter of 0 nm. Additional resonances introduced by the superlattice are present at all angles contributing to increased absorption. The fact that they strongly shift in frequency with angle suggests that the defects in this case are coupled together as mentioned above, forming an in-plane coupled resonator waveguide [44] with its own dispersion characteristics. We also plot the absorption enhancement ratio for these two cases in Figure 5.7c, which gives a clear map of all the new resonances introduced by the superlattice.

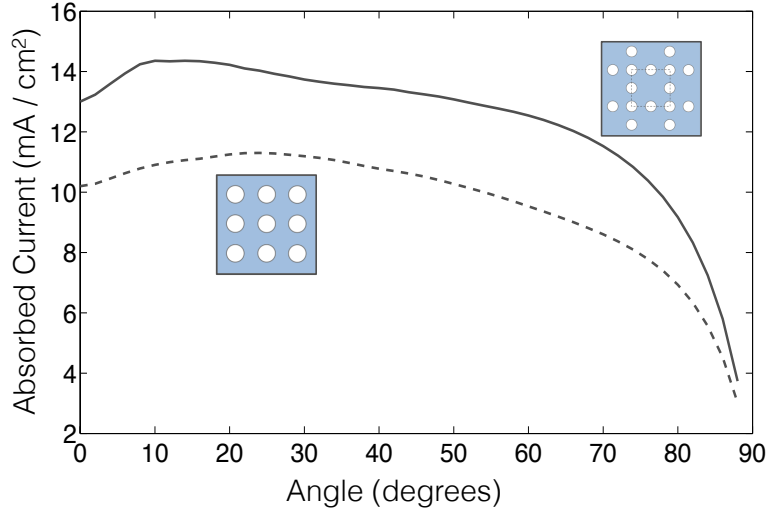


Figure 5.8: Integrated absorbed current for the center close-packed superlattice (solid line) and the original lattice (dashed line) as a function of incident angle, averaged over TE and TM modes and weighted by the AM 1.5 solar spectral current.

In addition to the new resonances introduced by the defects, incoupling to many of the modes present in the simple periodic photonic crystal are altered in the superlattice, as can be seen by the enhanced absorption for the superlattice even for some modes that were also present in the simple periodic photonic crystal. This altered incoupling to the modes of the simple periodic crystal structure could be due to altered reflectivity or through altered scattering due to the change in local dielectric

environment. The integrated absorbed current as a function of angle for the initial periodic case and the structure with an optimal superlattice is shown in Figure 5.8. The optimal superlattice always has a higher absorbed current at all angles.

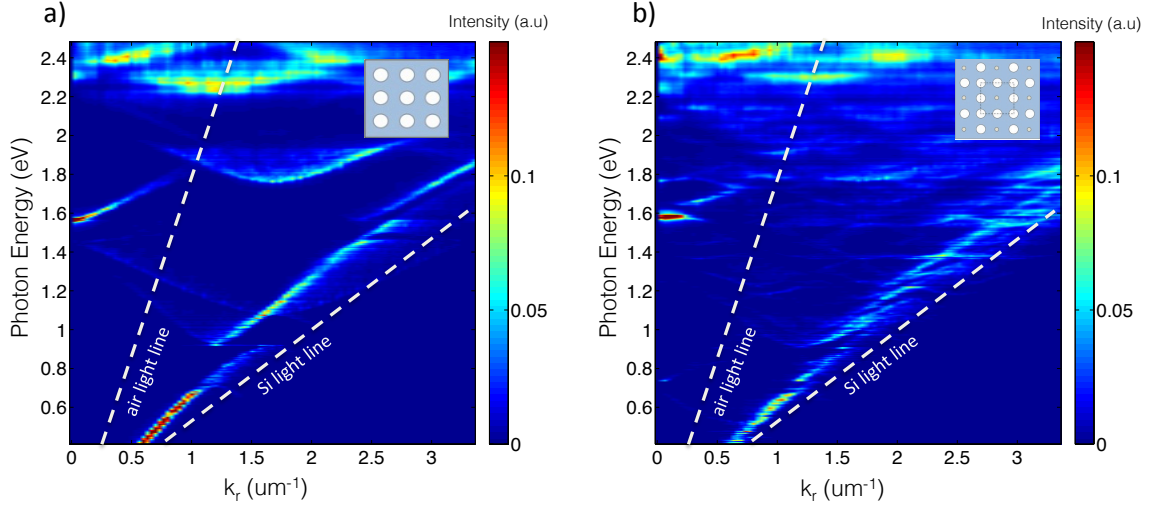


Figure 5.9: Maps of available modes as excited by sets of random dipoles in 2D lattice representations of a) base lattice with 290nm period, 232 nm diameter and b) base lattice with 0nm center close packed sublattice. There are clearly new modes introduced both above and below the air light line when the sublattice is added.

The angular spectra in Figure 5.7 shows the modes of the photonic crystal that are accessible from free space, or above the light line. There are other modes within the photonic crystal though that are below the light line and not accessible from free space. To get an idea of how many of these modes there are in each structure, we perform two-dimensional simulations of each structure, injecting energy into each lattice with sets of dipole sources with random positions and phases. We then take the spatial Fourier transform of the resulting field patterns to obtain a reciprocal space representation of the modes excited at each frequency. Upon averaging over radius in k -space, we can obtain a map of all the modes available in the structure as a function of in-plane wave vector. Though not quantitative due to the intensities of the peaks changing with dipole number and position, this method allows for a comparison of the relative density of modes in each structure. This method has recently been used

to investigate similar aperiodic structures [65]. Our results are shown in Figure 5.9. It is clear that there are additional modes both above and below the air light line for the superlattice case. Though not accessible for light incident on the photonic crystal alone, these additional modes could be excited with the addition of a scattering layer above or below the photonic crystal, as we will show below.

5.3 Superlattices In An Optimized Hexagonal Photonic Crystal

The addition of superlattices can be beneficial in many situations. To emphasize this, we now test this concept on a different starting simple periodic lattice. We begin with a hexagonal lattice of air holes in a 200 nm thick slab that has been optimized for absorbed current with respect to lattice constant and air hole diameter. We then introduce a rectangular superlattice on top of the original, forming what is known as a Suzuki lattice [68]. In addition to this, we test one other case by extending the rectangular superlattice into what we term the extended Suzuki lattice. Figure 5.10 shows the spectral absorption for these two cases as we vary the superlattice air hole diameter.

Again shown for reference is the original lattice case indicated with a vertical dotted white line. Similar to the square lattice case, increased absorption can be seen on either side of the dotted line at certain wavelengths, corresponding to the introduction of new resonances in the film when the superlattice is introduced. In Figure 5.11, we again plot the integrated absorption weighted by the solar spectrum and see that there is again always a superlattice case that outperforms the original lattice. A difference in this case, however, is that the optimum superlattice air hole diameters are not at 0 nm, instead they lie at slightly smaller diameters than the original lattice. The overall enhancement over the original lattice is also less, due to

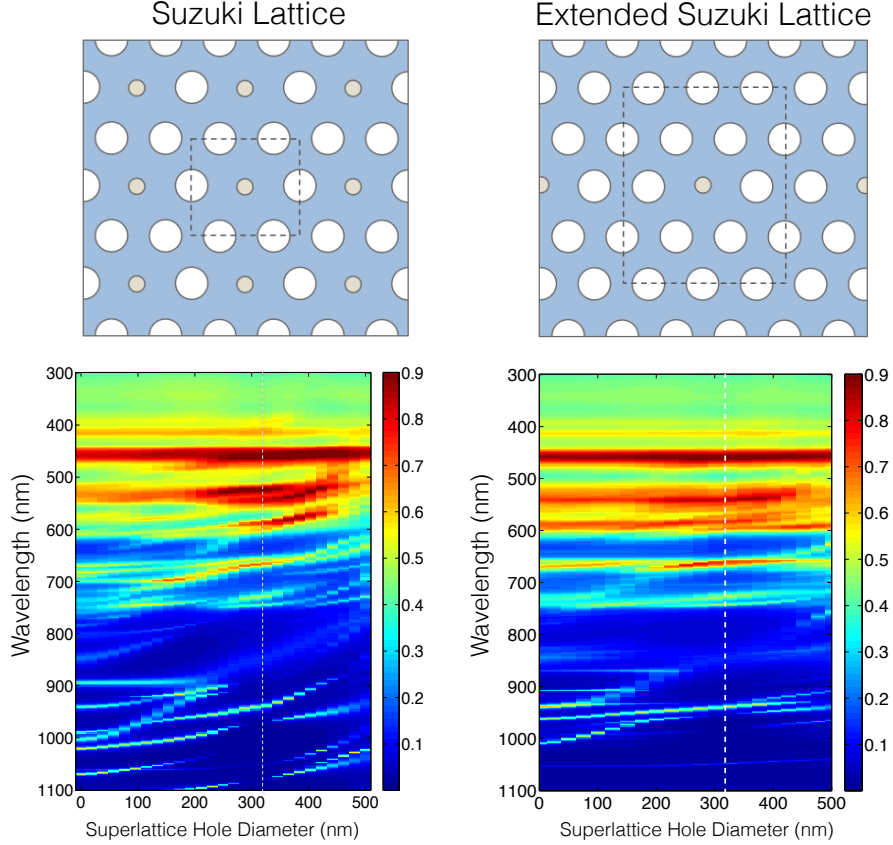


Figure 5.10: Fraction of light absorbed at normal incidence for (left) Suzuki lattice and (right) extended Suzuki lattice with a simple periodic lattice of $a = 510\text{nm}$ and $r = 155\text{nm}$.

the fact that the starting point was optimized.

Nevertheless, a reasonable enhancement is obtained in this case when the optimal superlattice is used. Lastly, in Figure 12 we calculate the angular response of the original hexagonal lattice and the optimal Suzuki superlattice corresponding to a defect diameter of 210 nm . Again there are many new resonances that are introduced by the addition of the superlattice, leading to increased absorption at all angles.

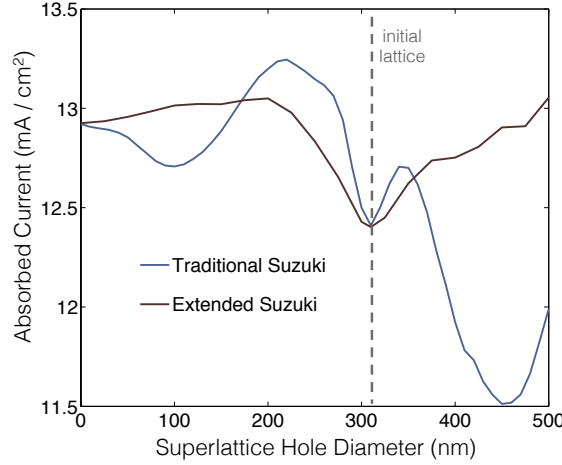


Figure 5.11: Absorbed current as a function of superlattice air hole diameter for two different superlattices in the hexagonal lattice obtained by integrating the data in Fig. 9 and weighting by the AM 1.5 solar spectral current.

5.4 Addition Of A Randomly Textured Dielectric Incoupler

We now further enhance absorption through the addition of a back reflector and a transparent, randomly-textured layer of dielectric material above the absorber. The back reflector adds a second pass for the photons that would otherwise escape out the back of the slab. The randomly textured dielectric incoupler layer enhances anti-reflection as well as helps facilitate randomization of the incoming wavevectors, increasing the number of accessible modes in the slab. We investigated numerous different textures calculated using FDTD at normal incidence. Fig. 5.13 shows the best case we found corresponding to a layer of Si_3N_4 with rms roughness of 40 nm and peak correlation length of 40 nm below a SiO_2 layer with rms roughness of 100 nm and correlation length of 100nm. We typically see an additional $2 \frac{mA}{cm^2}$ of absorbed current due to the back reflector, and in the case of Fig. 5.13, we see about a $3 \frac{mA}{cm^2}$ increase from the randomly-textured dielectric incoupler. This leads us to a total absorbed current of $18.3 \frac{mA}{cm^2}$ for the initial square lattice in this study with $a = 290$

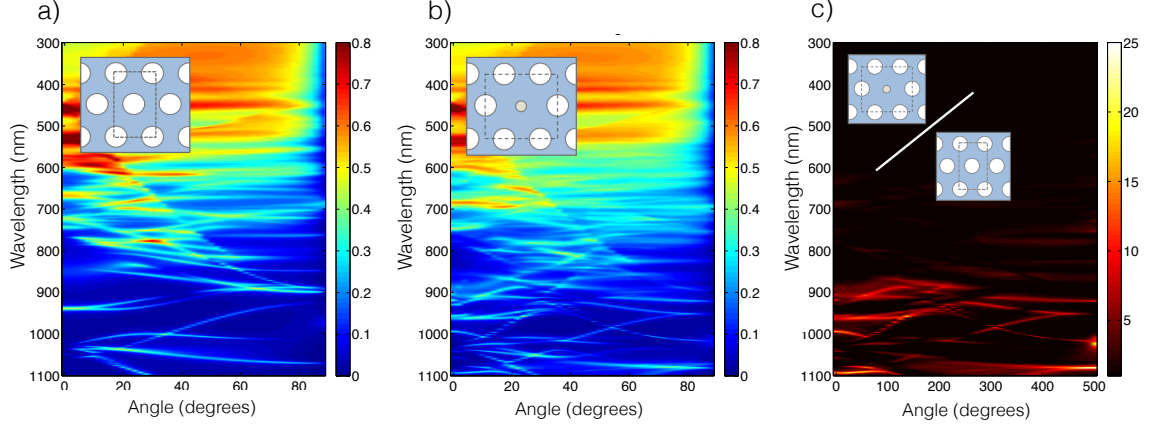


Figure 5.12: TE-TM averaged angular absorption spectra for (a) the original hexagonal lattice, (b) the optimal superlattice, and (c) the enhancement ratio.

nm and $d = 232$ nm. When this same texturing is placed on the optimal hexagonal superlattice case ($a = 510$ nm, $d = 310$ nm, $d_{\text{superlattice}} = 210$ nm) we achieve a absorbed current of $19.5 \frac{\text{mA}}{\text{cm}^2}$.

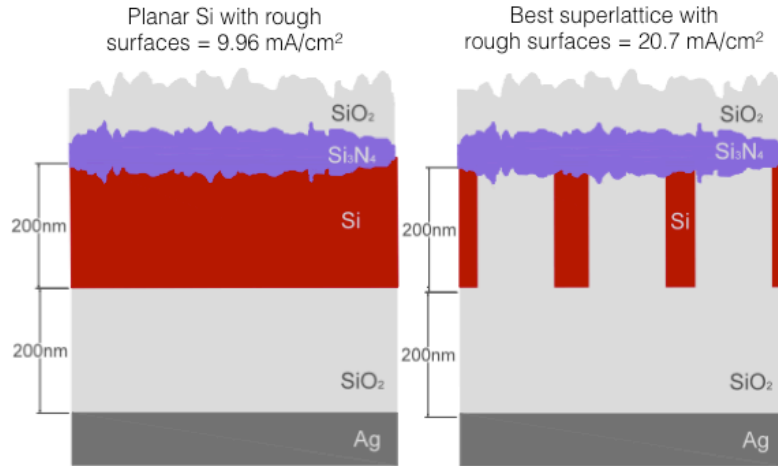


Figure 5.13: Schematic of a planar slab with roughened texturing (left) and the highest-performing structure (right), wherein a photonic crystal superlattice is integrated with a randomly textured dielectric incoupler.

Additionally, when we start with a different square lattice with optimized period and air hole diameter ($a = 550$ nm, $d = 350$ nm) and add an optimized edge close-packed superlattice ($d_{\text{superlattice}} = 300$ nm), as well as a randomly-textured

dielectric incoupler, we observe the highest absorbed current of this study at $20.7 \frac{mA}{cm^2}$. This is still less than the ergodic limit at 200 nm total thickness which is $31 \frac{mA}{cm^2}$. If we instead use the equivalent thickness of our structure, which is 144 nm, the optimal structure is closer but still below the ergodic limit at this thickness of $29 \frac{mA}{cm^2}$. While a different structure may be necessary to reach or exceed the ergodic limit, the absorbed current of $20.7 \frac{mA}{cm^2}$ is still more than 2 times larger than that of a planar Si slab with the same roughened texturing at $9.96 \frac{mA}{cm^2}$, as shown in Figure 5.13. We have also confirmed that each of the optimized superlattice structures have higher absorbed currents than the same randomly-textured dielectric incoupler applied to each of their respective starting lattices. These higher currents are achieved with the same incoupler due to the greater number of modes in the optimized superlattice than both the planar slab and the starting lattice.

5.5 Thicker Absorber Layers

The previous calculations were all done for 200 nm thick Si slabs mainly to illustrate the effects of different light trapping strategies. For thin layer Si cells to be competitive with commercial Si photovoltaic efficiencies, slightly thicker active regions and higher currents are necessary. To show that our approach can be extended to thicker absorbing regions, we simulated superlattice photonic crystal layers with randomly-textured dielectric incouplers with Si thicknesses of 1 to 4 microns, which can result in absorbed currents between 30 and $40 \frac{mA}{cm^2}$. For example, our 2 μm thick cell has $\sim 34 \frac{mA}{cm^2}$, comparable to other results in the literature [69] with similar thicknesses. It is also worth noting that we do not use equivalent thickness as a metric as it can complicate comparison of different patterns. These currents are not only approaching the ergodic ray optic light trapping limit for these thicknesses, but also show that our designs may be implemented to create thin film cells that are competitive in efficiency

with thicker cells. In Fig. 5.14 we show the simulated maximum absorbed currents for different geometries and thicknesses ranging from 200nm to 4 microns and compare with the ergodic limit.

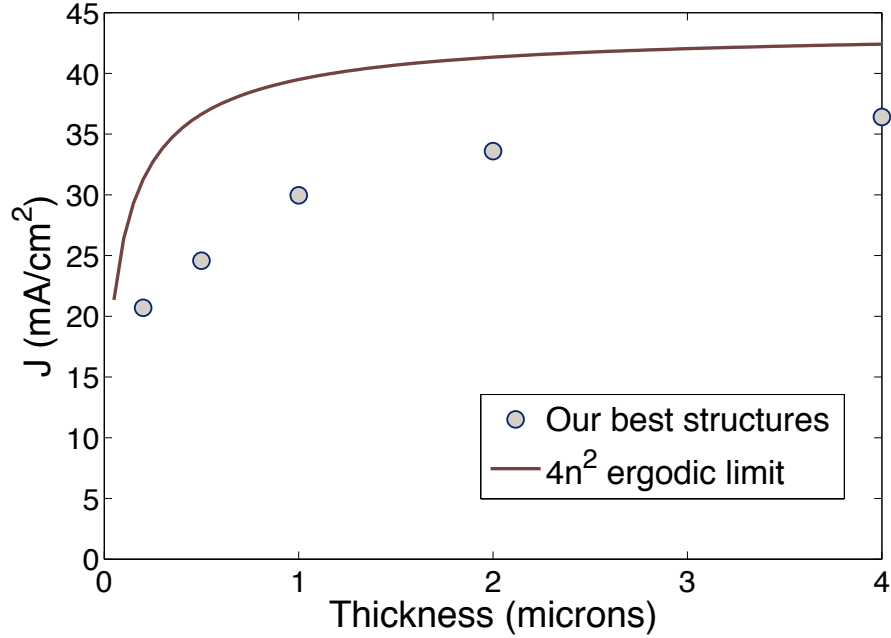


Figure 5.14: Summary of the change in absorbed current with changes in the geometry and thickness of the absorbing layer compared to the ergodic light trapping limit.

5.6 Conclusions

These results strongly suggest that simple periodic lattices are not optimal for light trapping in photonic crystals and that incorporation of additional superlattices can significantly increase absorption at all angles. Also, these results indicate that finding optimal disorder is not always trivial, as evidenced by the fact that the optimal superlattice type and diameter was different for different starting lattices. Thus, large multiparameter optimizations may be necessary to find optimal light trapping structures incorporating disorder. We have just provided one example of combining periodic and random structures to increase light trapping, but do not claim to have

found an absolute best combination. Much more work is needed to fully explore the other regions of the periodic to random continuum depicted schematically in Fig. 5.1. Two obvious extensions of the superlattice structures we have studied would be to introduce defects at non-periodic sites in a photonic crystal lattice and to use a poly-disperse size distribution of defects. These scenarios are much more computationally demanding and thus were not explored in this work, but will be the subject of future work. We have also shown that the combination of superlattice photonic crystals with randomly-textured dielectric incouplers significantly increases absorption. This is due to the fact that rough surfaces randomize incoming photons, lifting the constraint of selective mode occupation that occurs with periodic structures. These findings lend support to the idea that for most light trapping applications, a combination of periodic and random texturing may be optimal.

Chapter 6

Light Trapping In Thin Film GaAs

6.1 Introduction

GaAs is an ideal material for photovoltaic energy conversion. It has a direct bandgap well matched to the AM1.5G spectrum [54], can be epitaxially grown in high single crystal quality, and can be passivated with other III-V materials in the same epitaxial growth process. Traditionally, GaAs solar cells have been grown on substrate wafers, with the active device roughly index matched to the thick, inactive substrate material (\sim hundreds of microns). This makes light trapping difficult as nearly all photons incident on the device only get a single pass through the material. If they are not absorbed on the first pass, they enter the substrate where they are parasitically absorbed. Adding a back reflector or scattering surface to the wafer would be useless, as nearly all of the photons would be absorbed before reaching it. As a result, the active regions of high efficiency GaAs cells have traditionally been several microns thick.

Recently, GaAs cells have had renewed interest due to the process of epitaxial liftoff (ELO) [70, 71] in which the active device region can be removed from the substrate and placed on a reflective surface. This has allowed GaAs to achieve the world record single junction efficiency record [15], which has been steadily increasing for the last several years due to the efforts of the solar startup Alta Devices. One

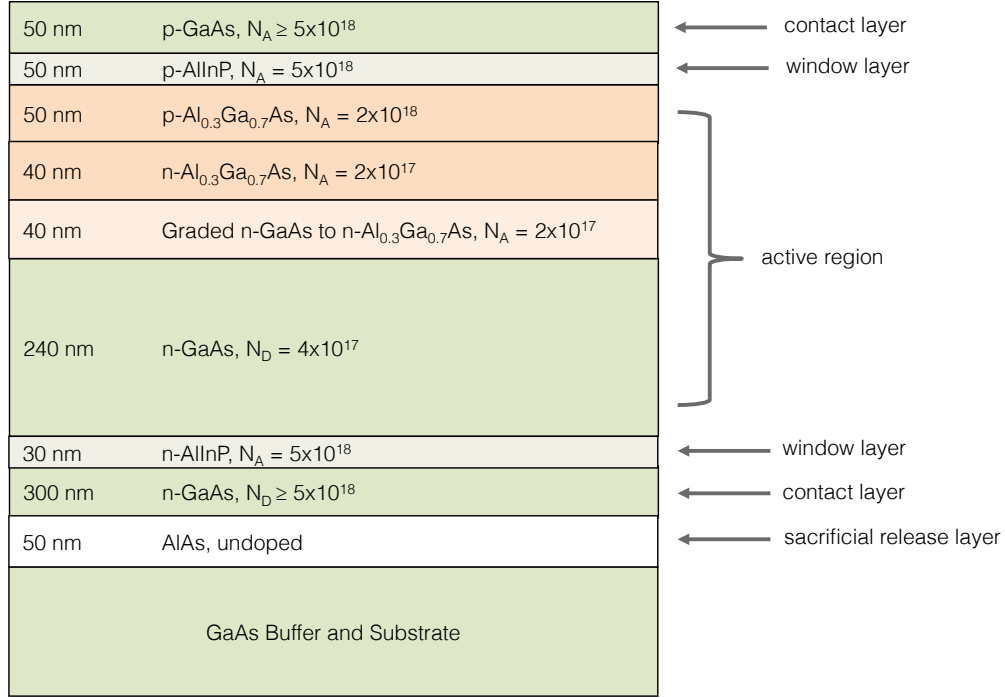


Figure 6.1: GaAs solar cell device architecture used in this study.

of the main reasons for this is due to an increased voltage when a back reflector is added. This is due to an increase in photon recycling and external radiative efficiency by removing the parasitic loss channel of the rear substrate [72]. The cost and weight of a thin-film cell is also reduced due to the reduction of total semiconductor material by ~ 2 orders of magnitude. Another advantage of adding a back reflector is that the active layer can also be thinned as non-absorbed rays get at least a second pass after reaching the rear of the cell. A thinner active region not only further decreases weight and cost, but also can potentially lead to a higher overall efficiency by increasing the voltage, a function of the volume-dependent bulk recombination. This increase in efficiency, of course, is only possible if the short circuit current of a thinned cell can be maintained high enough with sufficient light trapping. Additionally, Alta Devices has demonstrated that GaAs cells that have been removed from their substrate can be flexible, opening up new applications for photovoltaics that wafer-based cells cannot

be used for.

Here, we extend this concept further to even thinner active regions well below a micron. At these thicknesses, the cell can be considered “optically thin” (i.e. thin enough that even with perfect anti-reflection, a planar cell will not absorb enough photons to reach a reasonable efficiency). At these thicknesses, advanced light trapping schemes are needed. We design and fabricate ultrathin GaAs solar cells of $\sim 300\text{nm}$ and remove the devices from their native substrates using the process of epitaxial liftoff. We further process them into functioning devices by mesa etching and electrical contacting.

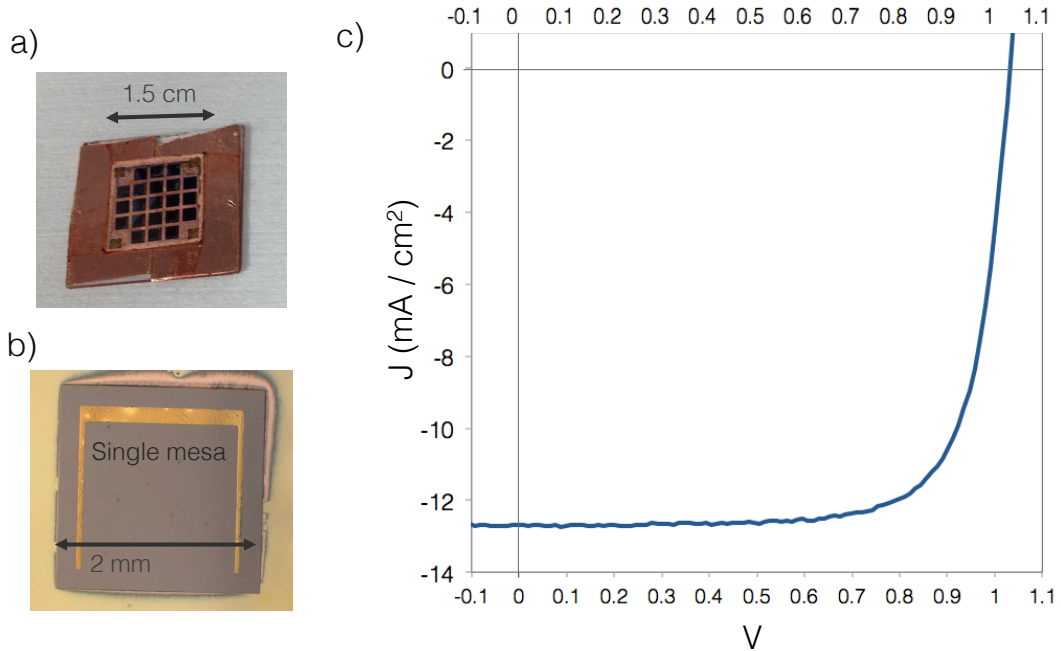


Figure 6.2: a) Image of lifted-off sample containing numerous GaAs devices after full processing, b) Image of single GaAs device after processing. c) Typical J-V curve of a cell after processing, before AR or nanoparticle deposition.

We then numerically examine ways of enhancing the absorption of a GaAs thin-film solar cell with various periodic nanopatterns of TiO_2 cylinders above the active region of the device. We examine the expected angular behavior of the cell and show that with the appropriate patterning, a periodically textured cell can outperform a

cell with an optimized anti-reflection coating at all incident angles. We then identify additional sources of photocurrent loss and identify ways of further increasing the solar absorption with additional device processing.

We then develop and implement a process for patterning thin GaAs solar cells with TiO_2 nanocylinders using the process nano-imprint lithography. We demonstrate this as a viable route to ultra-thin solar cells with significant enhanced absorption from a scalable, low-loss light trapping scheme.

6.2 Epitaxial Liftoff of Ultra-thin Film GaAs

GaAs heterojunction solar cells were grown via metal organic chemical vapor deposition (MOCVD) on a GaAs substrate wafer with an intermediate AlAs release layer at an outside chemical foundry, IQE. The full heterostructure is shown in Fig. 1. The AlAs layer preferentially etches at a rate 10^7 times faster than GaAs [71] and significantly faster than the other layers in the device in a hydrofluoric acid (HF) solution.

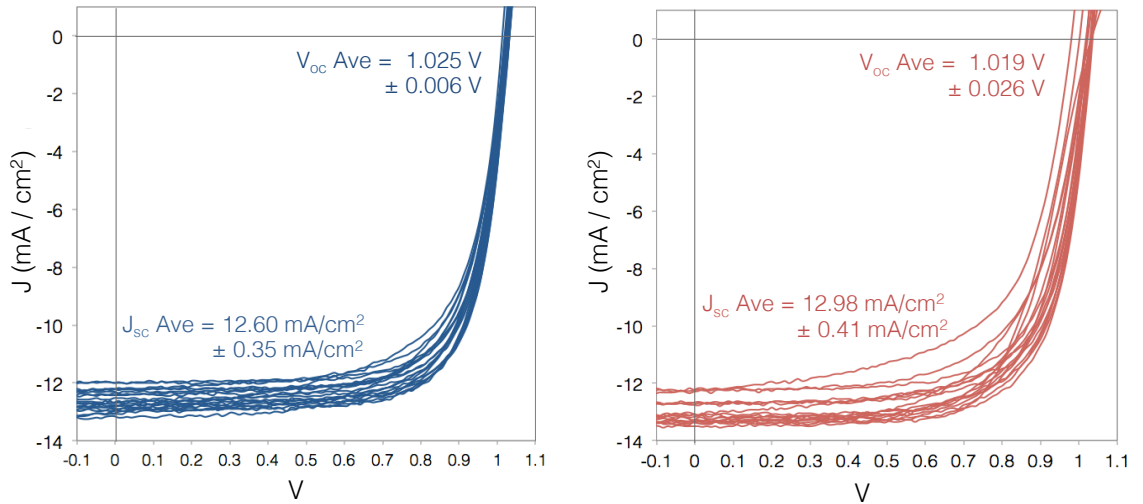


Figure 6.3: Sample to sample and cell to cell variation in thin-film GaAs J-V curves made via epitaxial liftoff. Each plot is a different 1.5 cm x 1.5 cm processed sample. Each trace in a different, mesa-isolated cell.

The wafers were diced into $1.5 \times 1.5 \text{ cm}^2$ squares before processing. The surface was cleaned by blowing with a supercritical CO_2 sno-gun, followed by sonication in acetone and isopropyl alcohol. They were then dipped in a hydrochloric acid solution for 30s, and dried with nitrogen. A thin 3 nm Ni layer was evaporated on the device side of the sample with ebeam evaporation at $\sim 1 \times 10^{-7}$ Torr, followed by 200 nm of thermally evaporated Cu. The samples were then immersed in a Cu electroplating solution and ~ 100 -200 μm of Cu was electroplated on the thermally evaporated metal. Following this, excess electroplated Cu on the edges of the sample was removed with a razor blade, and the samples were attached to a flexible plastic Kapton handle with bonding wax. The samples were then etched in 10% hydrofluoric acid overnight to release the device from the substrate. Following ELO, $2 \times 2 \text{ mm}$ devices were isolated by mesa etching. Finally, Ni/Cu top contacts were deposited via ebeam and thermal evaporation as before.

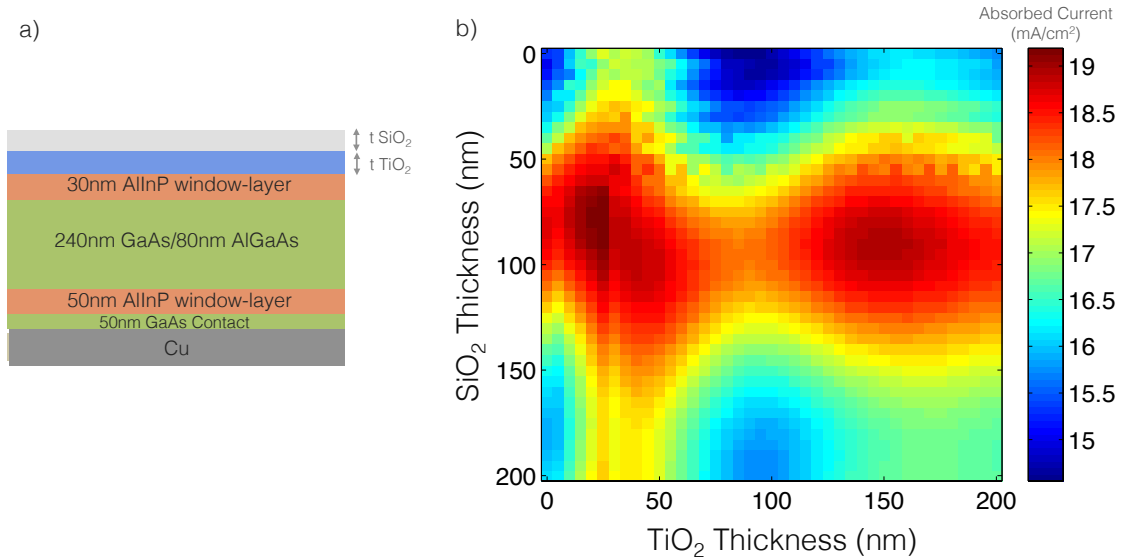


Figure 6.4: a) Layered structure used in the electromagnetic simulations. b) Bilayer anti-reflection coating optimization for the GaAs solar cell used in this study.

Current-voltage curves were taken for each of the mesa-isolated cells on each sample. Figure 3 shows current density-voltage curves for multiple cells on 2 different

1.5x1.5 cm ELO samples. Each lifted off sample contains 21 different 2x2 mm mesa-isolated cells. Cell to cell variation is small, but can be attributed to slight differences in surface and edge texture, contact variation, and slight curvature variations of the thin, non-rigid device/Cu handle.

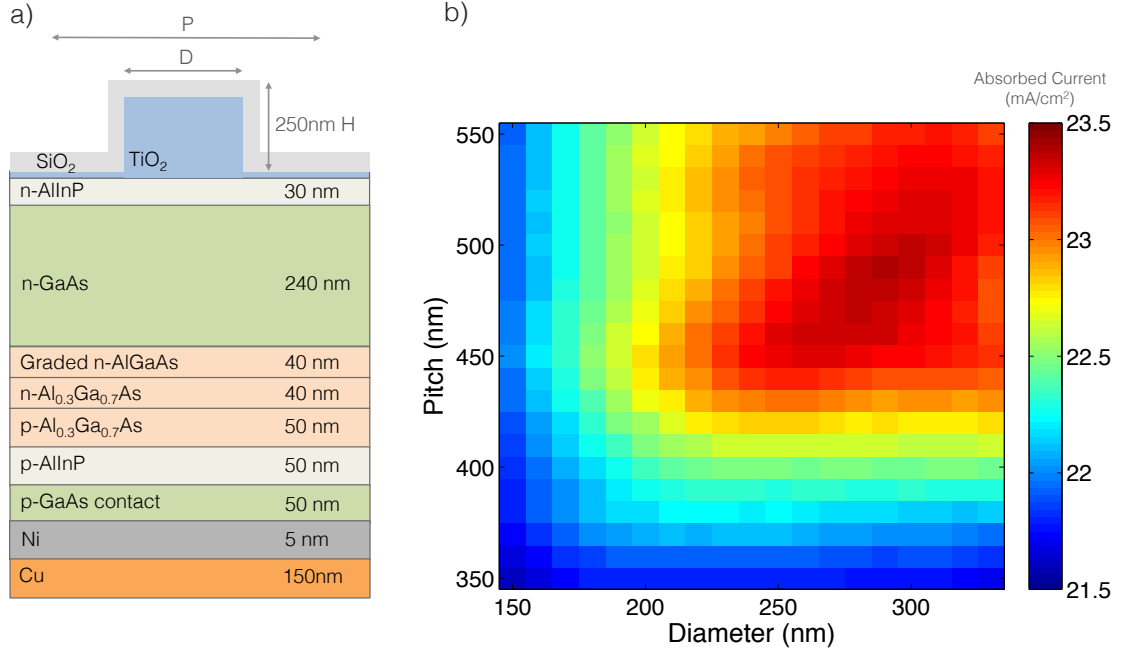


Figure 6.5: a) Schematic of nanopattern and optimization parameters. b) Square lattice TiO₂ cylinder FDTD optimization.

6.3 Pattern Optimization and Electromagnetic Simulations

We perform full-field electromagnetic calculations to investigate the absorption of the thin-film GaAs solar cell with and without various nanopatterning. Spectral absorption of the GaAs solar cell after ELO was calculated using the finite-difference time domain (FDTD) method with a commercial software package, Lumerical. First, optimal thicknesses for a bilayer anti-reflection coating made of TiO₂ and SiO₂ was calculated via a 2 parameter thickness optimization. The figure of merit for this op-

timization was the AM1.5G weighted absorbed current. This was obtained by taking the spectral absorption spectrum (i.e. fraction absorbed as a function of wavelength) and multiplying it by the binned spectral current in the AM1.5G spectrum. Upon integration over all wavelengths above the bandgap of GaAs, an absorbed current density is obtained. This would be synonymous with the often used short circuit current (J_{sc}) density if perfect electrical collection is assumed. The results of a bilayer anti-reflection coating optimization is shown in Figure 4.

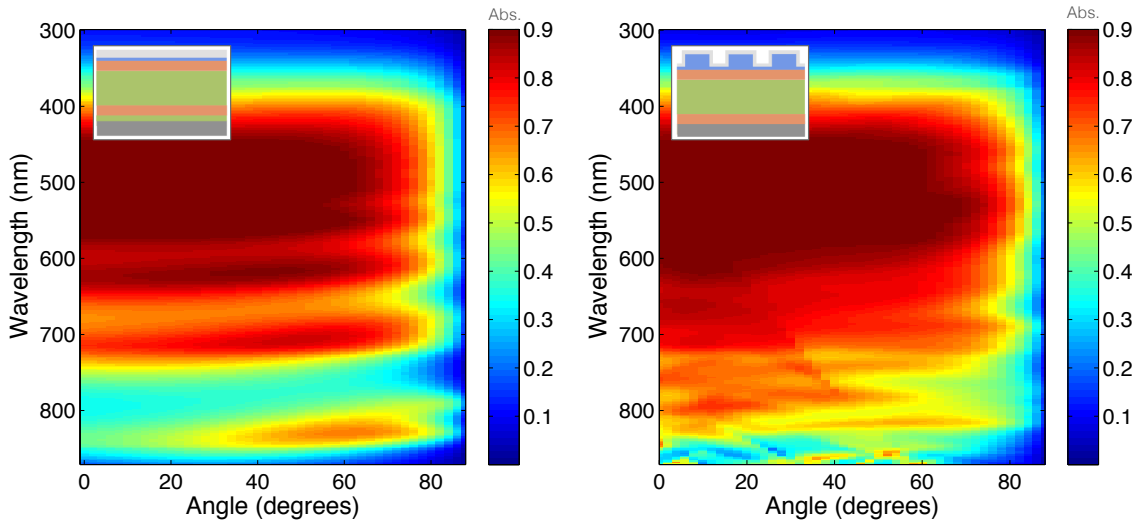


Figure 6.6: RCWA simulations of angular response of a) GaAs cell with planar optimized anti-reflection coating and b) optimized TiO_2 cylinder nanopattern.

FDTD was then used to determine the optimal nanopattern that maximizes the AM1.5G spectrally integrated absorbed current. Numerous optimizations were performed for different lattices, different cylinder heights, different back reflectors, etc. An example of an optimization for a hexagonal lattice of TiO_2 rods coated with a conformal 90nm SiO_2 layer on an Ni/Cu back reflector is shown in Figure 5. It can be seen that the absorbed current is significantly higher than what was obtained with the optimized bilayer anti-reflection coating from Figure 4.

To examine the angular behavior of the nanopattern, calculations were performed with rigorous coupled wave analysis (RCWA) for both TM and TE polarizations over

an angular range of 0-88 degrees. The results are shown in Figure 6. Also shown for comparison is the angular behavior of the cell with the optimized planar anti-reflection coating.

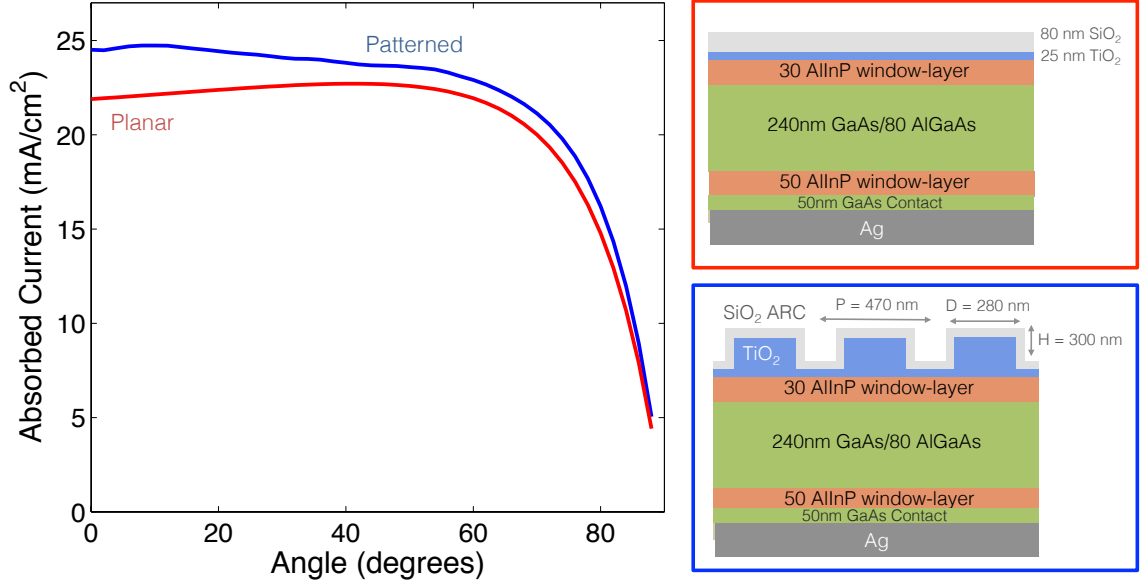


Figure 6.7: AM1.5G spectrally integrated absorbed current for the planar anti-reflection coated cell and the TiO_2 nanopatterned cell.

There is clearly increased absorption with the nanopattern, particularly in the long wavelength range near the GaAs bandgap. For a more quantitative comparison, the AM1.5G spectrally integrated absorbed current is calculated for each angle and plotted in Figure 7.

The enhanced absorption occurs due to numerous photonic resonances introduced by the periodic nanopattern. Some of these resonances change their spectral position as a function of angle, while others are relatively insensitive to the incident angle. To further examine the nature of these resonances, we plot the electric field intensity as a function of position at different wavelengths and angles in Figure 8.

At the points labeled “a” and “b” in Figure 8, the electric field shows a localized field within the TiO_2 cylinder above a Fabry-Perot type resonance in the planar solar cell. This same field pattern occurs at incident angles of both 40 and 60 degrees along

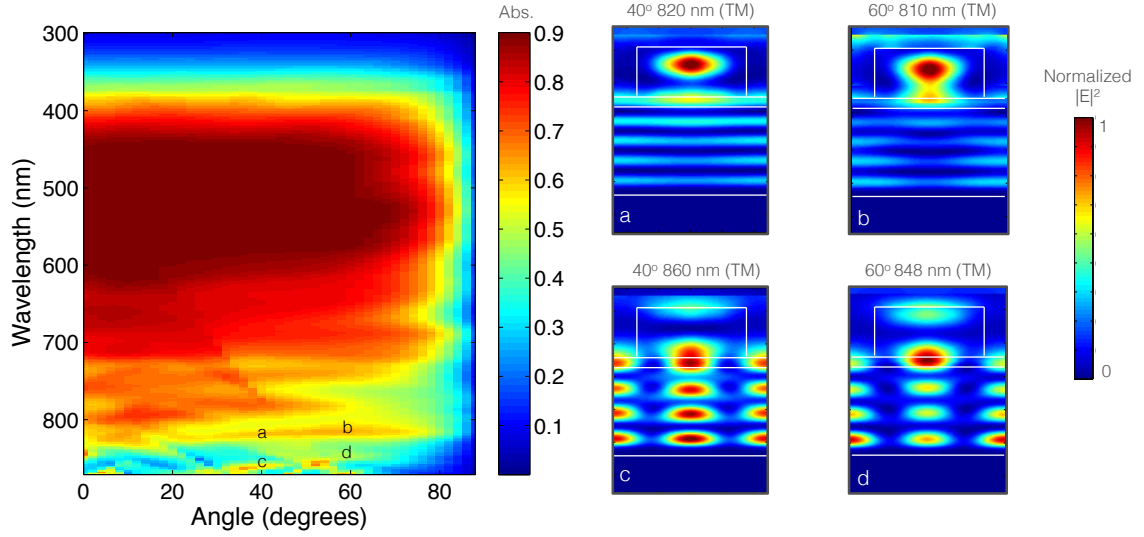


Figure 6.8: Electric field intensities for several resonant modes observed in the angular absorption spectrum.

the same resonance line in the angular absorption spectrum. Since these resonances are localized and not propagating in-plane, they are relatively insensitive to incident angle and can be considered non-dispersive. A different type of mode is seen at points “c” and “d” in Figure 8. These field profiles reveal a periodic, propagating mode in the solar cell region. These types of modes have their own dispersion and change spectral position with incident angle as the incident in-plane wavevector is changed. Since they are not present in the planar absorption spectrum, the periodic array above the solar cell must be incoupling incident light into these normally ”trapped” modes of the high index solar cell.

While the enhanced absorption introduced by the TiO_2 nanopattern is significant, the integrated absorbed current is still well below the theoretical value of $\sim 31 \frac{\text{mA}}{\text{cm}^2}$. To examine where the remaining optical losses are, we calculate the absorption in each of the layers of the structure and plot it in Figure 9.

A significant amount of absorption in the blue region of the spectrum occurs in the top AlInP window layer. This is difficult to avoid without thinning this layer or using a different material with lower absorption coefficient. In fact, even the current

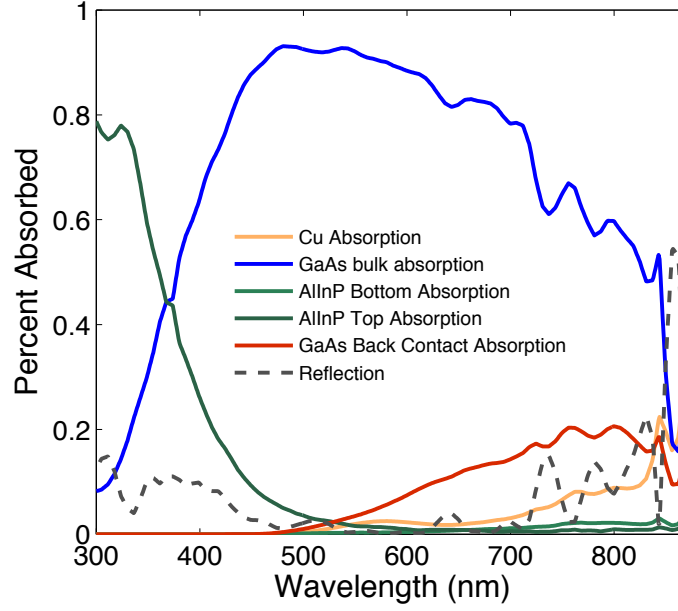


Figure 6.9: Quantification of losses in each layer of the GaAs solar cell structure.

world record GaAs solar cell shows similar losses in the blue region of the spectrum in the external quantum efficiency (EQE) curve [15]. Additional significant losses occur in the rear 50nm highly doped GaAs contact layer. This layer is present solely to achieve ohmic electrical contact between the device and rear metal. For III-V materials with high conductivity and low sheet resistance like the ones used here, electrical contact does not need to be made conformally over the entire planar area. Significant portions of the contact layer could be removed and the device could be contacted selectively as is done on the top surface of the device. This would result in less interaction of the incident light with the lossy rear contact layer, resulting in less parasitic absorption and potentially higher usefully absorbed current. Additionally, if a low refractive index dielectric spacer is placed between the device and rear metal reflector, reflection can occur at this interface and reduce interaction and loss at the rear metal surface.

To quantify how much of an improvement is achievable, we re-optimize a hexagonal periodic pattern of TiO_2 cylinders on a device without a rear GaAs back reflector

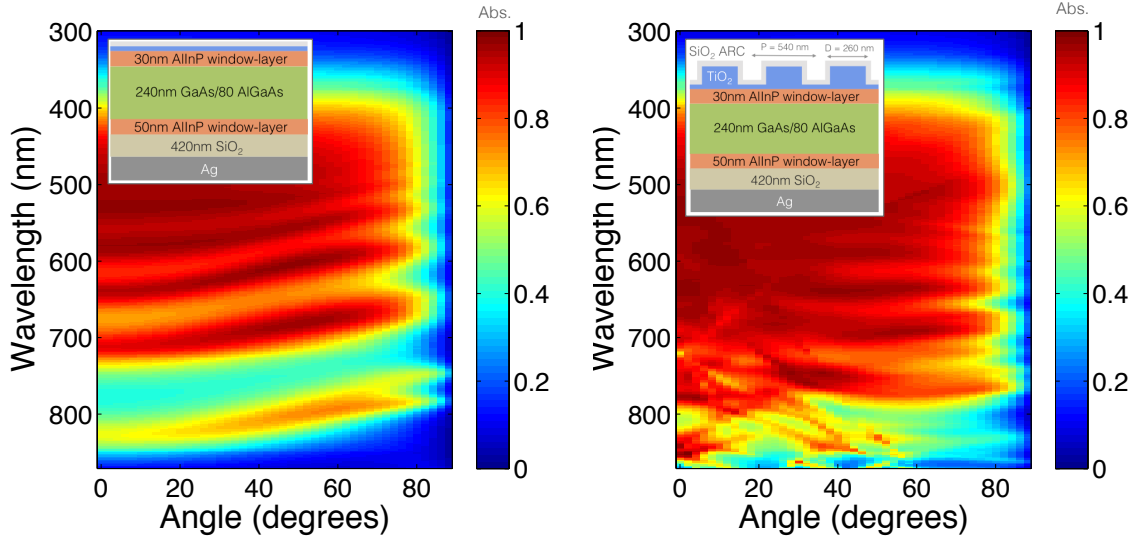


Figure 6.10: Angular spectra of the GaAs solar cell with the rear contact removed with and without addition of an optimized nanopattern.

and with an optimized dielectric spacer of refractive index 1.5. The angular spectra of this structure compared with a similar structure without the TiO_2 patterning is shown in Figure 10.

Again, we see significant absorption enhancement in the long wavelength region of the spectrum due to new modes being excited by the periodic nanopattern. To compare all of the structures we have examined, we plot the integrated absorbed current over all angles in Figure 11.

A significant increase in absorbed current is seen for both cases without a GaAs rear contact layer. The highest absorbed current at all angles is achieved with an optimized TiO_2 nanopattern on a cell without a rear GaAs contact layer and a dielectric spacer between the device and rear reflector.

In reality, the entire GaAs contact layer cannot be removed to allow for selective contact to the device. Because of this, the actual reduction in parasitic absorption would be slightly less than calculated in these simulations. Since the dimensions of typical contact stripes are much larger than the wavelength, the expected reduction in parasitic absorption could be approximated using the fill fraction of removed GaAs

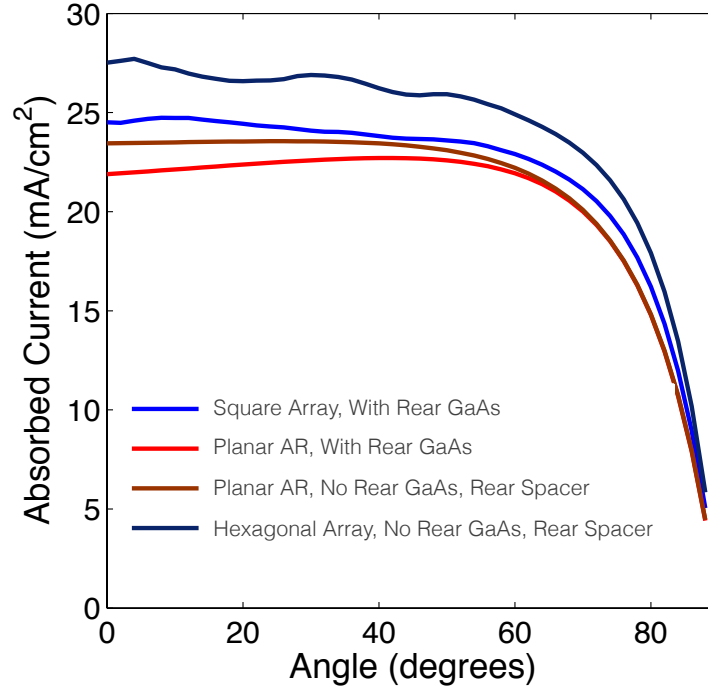


Figure 6.11: Integrated absorbed current for 4 different GaAs solar cell configurations.

contact material.

From these results, it is very clear that there are numerous ways on enhancing the solar absorption of a thin-film GaAs solar cell without compromising the active region of the device.

6.4 Light Trapping in Ultra-thin Film GaAs Using Nanoimprint Lithography

Substrate conformal nanoimprint lithography (SCIL) was performed using in-house fabricated PDMS nanoimprint stamps and SiO_2 based sol-gel. First, electron beam lithography was performed using ZEP resist on a Si wafer over a 1.5 cm x 1.5 cm area. The resulting patterned wafer was then etched in an Oxford Instruments Inductively Coupled Plasma Reactive Ion Etcher (ICP-RIE) using a Bosch process (SF_6 , C_4F_8)

to transfer the pattern into the Si wafer. Following etching and resist removal, this Si “master” wafer was used as a mold to make poly-di-methyl-siloxane (PDMS) stamps. First, a layer of high-density PDMS (X-PDMS) is prepared and spun onto the Si master. This modified PDMS has a Young’s modulus 20-40 times larger than standard PDMS, which prevents adjacent features in the stamps from contacting each other and sticking together [73]. A normal PDMS mixture was then poured over the X-PDMS coated master and cured at 80 °C for 1 hour. An image of the 1.5 cm x 1.5 cm master and resulting PDMS stamp is shown in Figure 12.

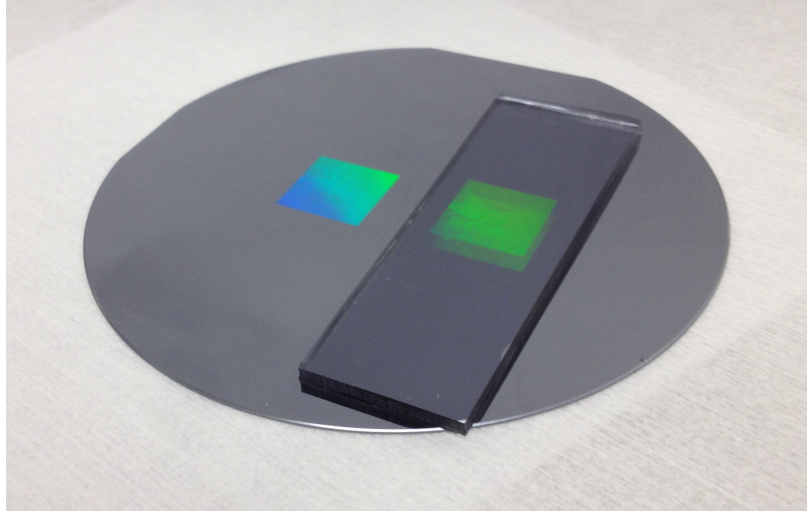


Figure 6.12: 1.5cm² master and resulting PDMS stamp.

The TiO₂ nanopattern deposition process was first tested on a Si wafer. First, a Si wafer was coated with a 300nm PMMA layer followed by a thin ~100nm layer of SiO₂ based sol-gel via spin coating [73]. The PMMA layer serves to increase the height of the patterned holes so taller nanostructures can be deposited through the mask. Immediately after spin coating, the sample was gently put into contact with the PDMS stamp and left to dry for 1-2 hrs.

The SiO₂ patterned wafer was then etched in a 2-step RIE process. First, a C₄F₈ etch was performed to break through any residual SiO₂ layer at the bottom of the

imprinted holes. Then, an O_2 etch was performed to etch through the PMMA layer beneath the SiO_2 .

Following etching, TiO_2 was deposited via ebeam evaporation in an O_2 environment at 1×10^{-5} Torr. The PMMA and SiO_2 layers were then removed in acetone with sonication. Figure 13 shows an optical image of the resulting TiO_2 nanopattern on the Si wafer. Most of the 1 cm x 1 cm area was uniformly covered in the nanopattern as shown in the image. Scanning electron microscope (SEM) images of the same pattern are shown in Figure 14.

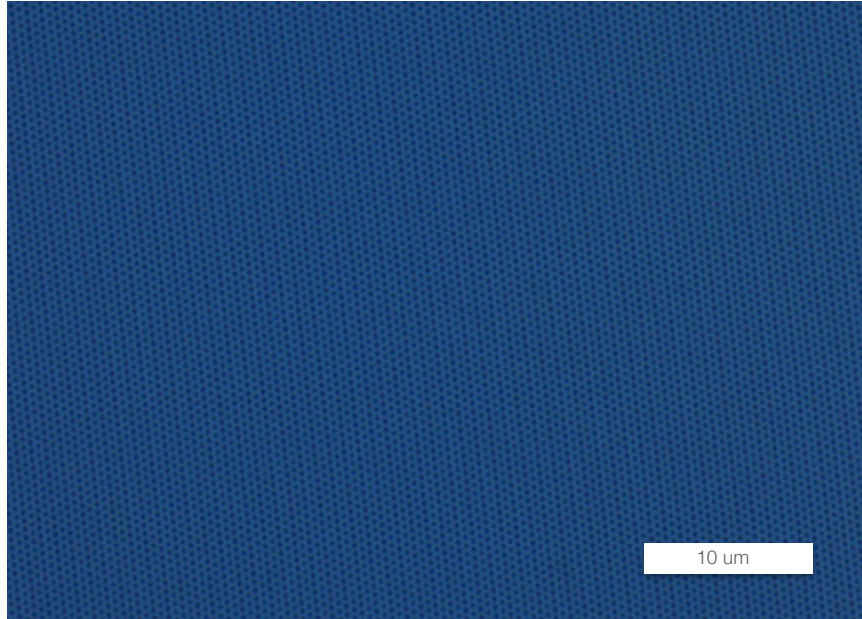


Figure 6.13: Optical image of a hexagonal pattern of TiO_2 nanoparticles on Si with a period of 540 nm and diameter of 260 nm.

Before patterning the GaAs solar cells, they were conformally coated in a 25nm TiO_2 layer before imprinting. This thin TiO_2 both acts as a bottom anti-reflection layer and provides protection for the underlying GaAs during subsequent reactive ion etching. The sample was then coated with a 300nm PMMA layer followed by a thin ~ 100 nm layer of SiO_2 based sol-gel via spin coating [73]. Immediately after spin coating, the sample was gently put into contact with the PDMS stamp and left to

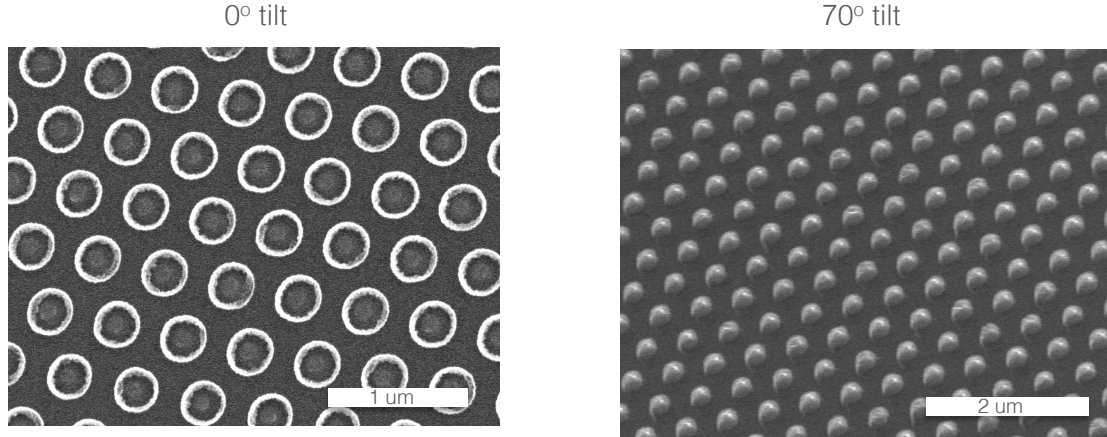


Figure 6.14: SEM images of a hexagonal pattern of TiO_2 nanoparticles on Si with a period of 540 nm and diameter of 260 nm.

dry for 1-2 hrs.

The SiO_2 patterned GaAs solar cells were then etched in a 2-step RIE process. A C_4F_8 etch was performed to break through any residual SiO_2 layer at the bottom of the imprinted holes. Then, an O_2 etch was performed to etch through the PMMA layer beneath the SiO_2 .

Following etching, TiO_2 was deposited via ebeam evaporation in an O_2 environment at 1×10^{-5} Torr. The PMMA and SiO_2 layers were then removed in acetone and sonication. Lastly, a 90nm SiO_2 layer was deposited via ebeam evaporation to complete the patterning. This SiO_2 layer serves as a top anti-reflection layer. In parallel with this patterned sample, a GaAs sample was prepared with a planar anti-reflection coating with the same material thicknesses (25nm TiO_2 , 90nm SiO_2). An image of the final planar and nanopatterned GaAs solar cells are shown in Figure 15.

A 1.5 cm x 1.5 cm square sample was stamped with a 1 cm x 1 cm square stamp. After full processing, this resulted in some devices on the sample having the nanopattern and some devices having a 2-layer anti-reflection coating. This allows for comparison of cells from the same lift-off that were exposed to the exact same processing conditions throughout fabrication. To ensure a fair comparison, many cells from

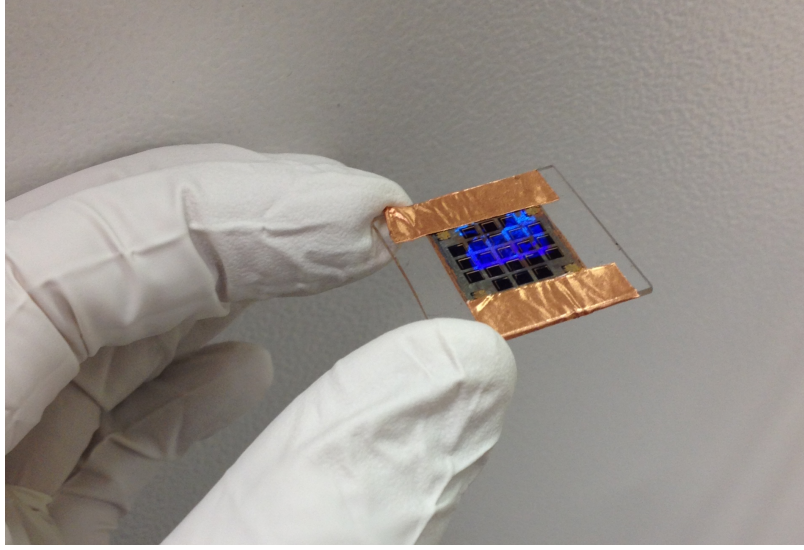


Figure 6.15: GaAs solar cells after TiO_2 nanopatterning and SiO_2 deposition.

the sample are not included in these results that were visibly different from each other. Reasons for the differences in cells despite the same processing conditions are non-uniform contact liftoff, non-uniform PMMA/sol-gel liftoff, misaligned stamping, visible cell damage, etc.

Current-density voltage curves for several cells on a single sample are shown in Figure 16. Only 2 cells on this sample had uniform nanopattern coverage and were free from other damage. Their average photocurrent was measured to be about $1 \frac{\text{mA}}{\text{cm}^2}$ higher than cells on the same sample with only a 2-layer anti-reflection coating. The total energy conversion efficiency of these devices is about $\sim 10\text{-}12\%$.

Because we have observed variation in J_{sc} of up to $1 \frac{\text{mA}}{\text{cm}^2}$ as shown in Figure 3, it is difficult to make a strong conclusion about these current density-voltage curves until more samples have been tested and compared.

To further characterize the cells, external quantum efficiency measurements were made on single cells that were half patterned and half coated with an anti-reflection coating. This was achieved by aligning the edge of the nanoimprint stamp with the center of a 2 mm x 2 mm cell. The cells were illuminated with a focused incident beam

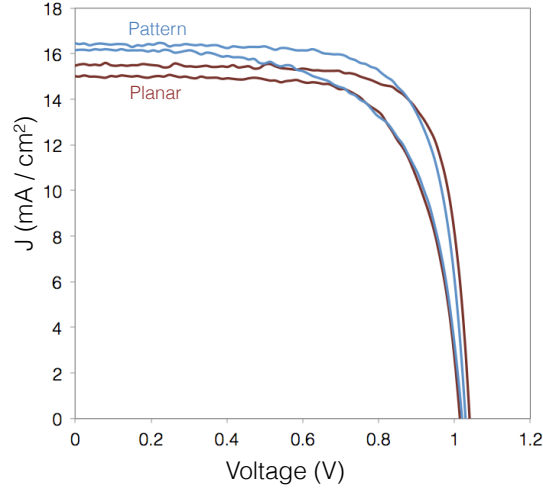


Figure 6.16: Current density-voltage curves for cells with and without a TiO_2 nanoparticle coating.

with a spot size ~ 10 microns in diameter, allowing for measurements of each area of the cell individually. Figure 17 shows external quantum efficiency measurements of each of these areas on 2 different cells.

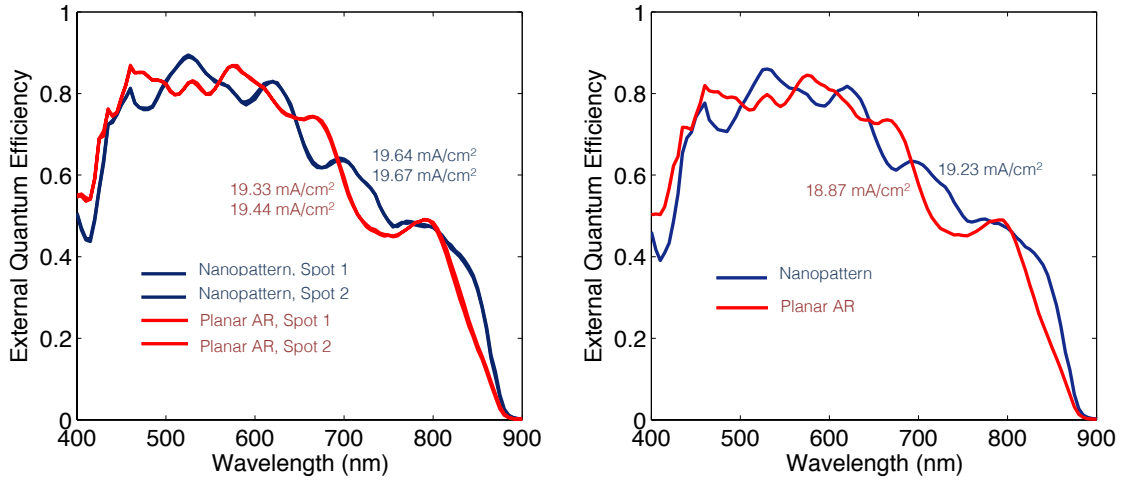


Figure 6.17: External quantum efficiency measurements of different positions of single cells with and without nanopatterning.

These plots show that some regions of the spectrum are absorbed more efficiently with the nanopattern and some are better absorbed with the anti-reflection coating. Also shown in Figure 17 are calculations of short-circuit current obtained by weighting

the EQE spectra with the spectral current in the AM1.5 spectrum and integrating over all wavelengths. It can be seen that there is a slight ($\sim 0.2\text{-}0.4 \frac{\text{mA}}{\text{cm}^2}$) increase in J_{sc} for the nanopatterned areas compared to the areas coated with an anti-reflection coating. This result is qualitatively but not quantitatively the same as obtained from J-V measurements.

The discrepancy in the values for short-circuit current obtained from the J-V curves and EQE measurements could be due to several factors including shadow loss ($\sim 2 \frac{\text{mA}}{\text{cm}^2}$), inhomogenities in surface quality, calibration, etc.

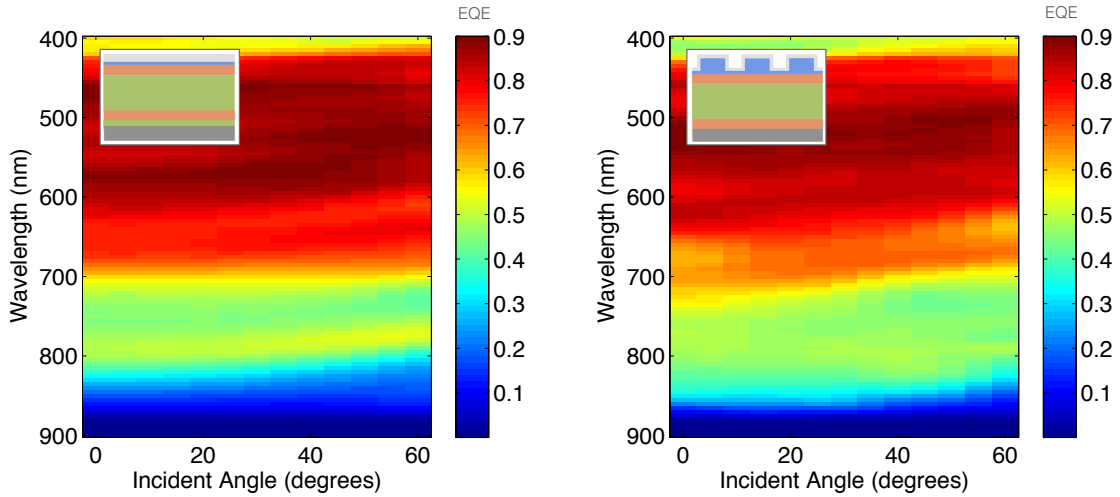


Figure 6.18: Angle-dependent external quantum efficiency measurements of different positions of single cells with and without nanopatterning.

We also measure the angle-dependent EQE for different areas of a single GaAs solar cell and plot the results in Figure 18. There is slightly more absorption in the red region of the spectrum for the area of the cell with the nanopattern for most angles. The planar cell also has a relatively flat response as the angle is changed while the nanopatterned cell is slightly more sensitive to incident angle. To determine which cell operates better under AM1.5G conditions, the EQE is again weighted by the solar spectrum and plotted in Figure 19.

The nanopatterned area performs better at angles close to normal while the AR

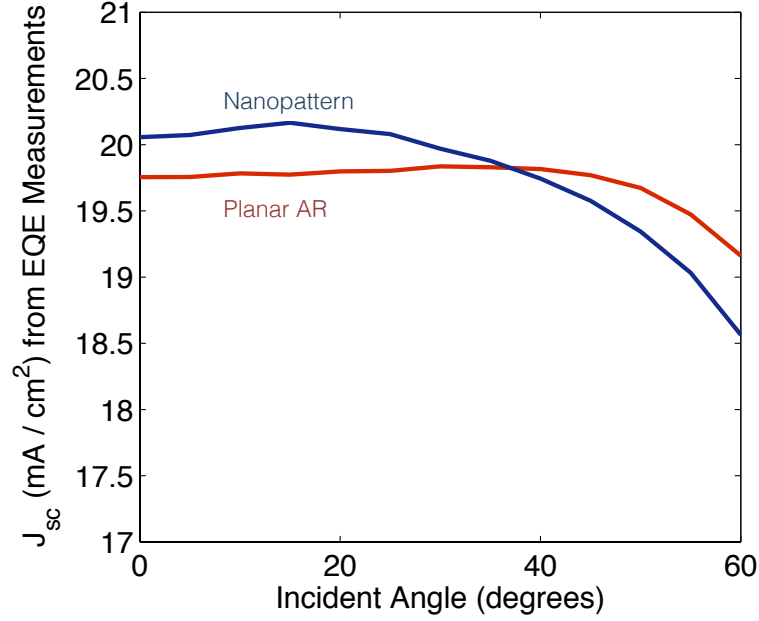


Figure 6.19: Short-circuit current as a function of angle as determined from EQE measurements for nanopatterned and AR coated areas of a single cell.

coated areas have higher short-circuit current at steeper incident angles.

While these results are promising, they are still far from what we believe can be achieved with TiO₂ nanopatterning. Reasons for the inferior performance possibly include non-optimal TiO₂ refractive index, non-optimal SiO₂ coating, non-uniform cell quality, and non-uniform and non-optimal imprinting due to non-ideal flatness of the GaAs solar cell samples. Many of these factors can easily be improved with further study and refinement and we believe that absorption enhancements approaching those observed in simulation will be achievable in the near future using the processing and fabrication schemes we have developed.

Chapter 7

Summary And Outlook

The main subject of this thesis was to examine the possibilities and limits for manipulation of light in thin solar cells using nanophotonics. As state of the art solar cells aim to further increase efficiency and decrease cost and weight, their thicknesses will inevitably decrease as much as can be tolerated. As discussed in Chapter 1, the ultimate solar cell is one that is as thin as possible while also absorbing as much light from the sun as a thick cell. For these reasons, advanced light trapping schemes and understanding the consequences of wavelength-scale features on device performance will be increasingly more important for future solar cell technology. The idea and concepts explored in this thesis open up many interesting avenues for future work, some of which are explained in detail here.

7.1 Exceeding The Ergodic Limit In Si

In Chapter 3, we have shown how the LDOS can be manipulated to enhance light absorption to levels beyond previously defined limits. In practice, this is easier to achieve using absorbing materials that have relatively low refractive indices ($\sim 1.5 - 2.5$), such as the P3HT:PCBM absorber we explored in Chapter 3. To achieve light trapping in higher index, more common solar cell materials like Si, more advanced designs than those featured in this thesis will be required. The photonic crystal

designs explored in Chapter 5 are a good start. To convincingly demonstrate that this approach can be used to exceed the light trapping limit in Si, a more refined effort specifically aimed at designing photonic crystal structures to increase the LDOS over a small bandwidth is needed. This could be done with focused design as was done in Chapter 5, or by more computationally demanding approaches, such as using the maximization of the LDOS as a figure of merit in an advanced electromagnetic optimization [74].

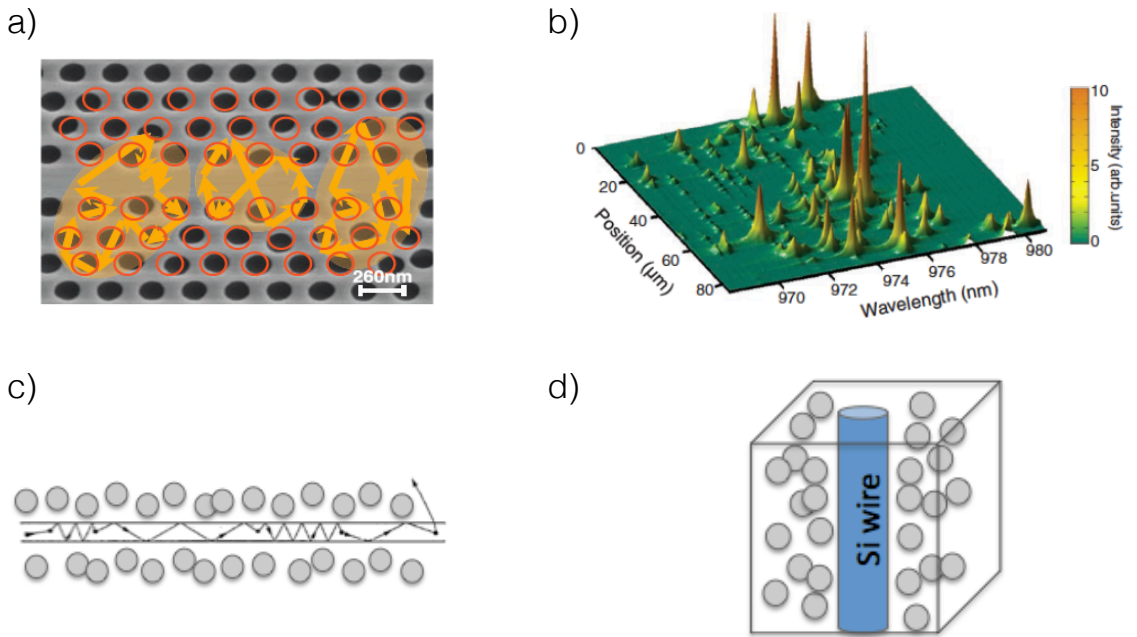


Figure 7.1: a) [from Sapienza et al, 2010] [75] Formation of effective optical cavities within a 1-dimensional photonic crystal waveguide clad with appropriately disordered scatterers. b) [from Sapienza et al, 2010] [75] Spectrally resolved intensity plots as a function of position within the waveguide. Light is localized at different wavelengths along different positions in the waveguide, forming a novel type of broadband optical cavity. c) Potential 2D design that could be used to demonstrate Anderson localization for solar cell applications: Thin film of weakly absorbing material (i.e. Si or a polymer) clad with appropriately designed scattering particles on both sides. d) Potential 1D design: Si wire array filled with dense powder of appropriately designed scattering particles. Light will be localized in the 1-dimensional waveguide formed by the Si wire.

A fundamentally different way of trapping light that has potential to increase the

LDOS in high index materials is Anderson localization of photons [76], caused by multiple scattering on a scale shorter than the wavelength. Under the appropriate conditions, the electric field is scattered multiple times within a single optical cycle, and the photon becomes strongly localized. Surprisingly, this method of light trapping has not been explored much in the context of increasing absorption for solar energy harvesting. When Anderson localization of light occurs, an effective optical cavity is formed, in which the LDOS is increased [75], as shown in Figure 7.1. We also saw in Chapter 3 that besides increasing the LDOS, the other important criterion for achieving optimal light trapping is the full and equal population of the internal modes of the structure, typically achieved with a random, scattering surface. Anderson localization is achieved in certain, special cases of disordered media, and is thus inherently random in nature. Structures that exhibit Anderson localization of photons therefore may be able to achieve both of the criteria for optimal light trapping (increased LDOS and ability to populate the internal modes) at the same time in a single structure. Two examples of potential geometries to explore this idea are shown in Figure 7.1.

7.2 Purcell Enhanced Photovoltaics

In Chapter 3, we explored how increases in the LDOS can be used to increase light trapping. Manipulation of the LDOS could also potentially affect other processes and quantities inside ultrathin solar cells besides absorption and J_{sc} , for example, the V_{oc} .

In a photovoltaic device, at open circuit, no current is collected and the number of recombination events inside the solar cell equals the number of excitation events. In the ideal case, the solar cell will radiate the same number of photons back to the sun as it absorbs. This, of course, means that the external luminescence quantum efficiency (EQE_L) is unity. If this occurs, the V_{oc} will take on its theoretically maximum

value [13, 77, 78]. As soon as the luminescence quantum efficiency decreases, there is an immediate penalty on the V_{oc} as described by the equation [78]:

$$V_{oc} = V_{oc}^{max} + \frac{kT}{q} \ln(EQE_L) \quad (7.1)$$

This penalty will severely limit the new theoretically maximum detailed balance overall efficiency of the solar cell and is why materials with very high intrinsic luminescence QEs like GaAs (QE $\sim 99\%$) have much higher potential conversion efficiencies than Si [72].

The intrinsic luminescence quantum efficiency, IQE, of an emitter can in theory be increased by coupling it to an electromagnetic environment with a modified local density of optical states (LDOS). This will alter the radiative rate, L_{rad} , as well as possibly introduce new non-radiative pathways, L_{nr} and L_{nr}^{abs} . The increase of the rate of emission into a given radiative channel is often termed the Purcell Factor [79], and has been studied extensively in the field of nanophotonics with regard to manipulating light emission. The new rates introduced by a modified LDOS can alter the quantum efficiency of the emitter according to the equation given by Bharadwaj and Novotny [80]:

$$IQE_L = \frac{\frac{\Gamma_{rad}}{\Gamma_{rado}}}{\frac{\Gamma_{rad}}{\Gamma_{rado}} + \frac{\Gamma_{nr}^{abs}}{\Gamma_{rado}} \frac{1-QE_{Lo}}{QE_{Lo}}} \quad (7.2)$$

where L_{rado} is the original, intrinsic radiative rate of the emitter. This will change the rate of conversion of excitation to photons inside the device. To input in the expression for V_{oc} , it must be converted to EQE by multiplying by a conversion factor. This conversion factor depends on outcoupling and the specific device/emitter geometry and in theory could vary from 0 to 1. For simplicity and to arrive at an upper limit, here we take it to be 1. We can now use Eq. 7.1 and Eq. 7.2 to obtain an expression for the V_{oc} in an environment with a modified LDOS.

We can now determine the effect of a modified electromagnetic environment on the maximum obtainable open circuit voltage for a solar cell with an initial value for intrinsic luminescence quantum efficiency. If we make the assumption that our modifying structure adds a negligible amount of non-radiative recombination pathways ($\Gamma_{nr}^{abs} = 0$) we obtain the following plot:

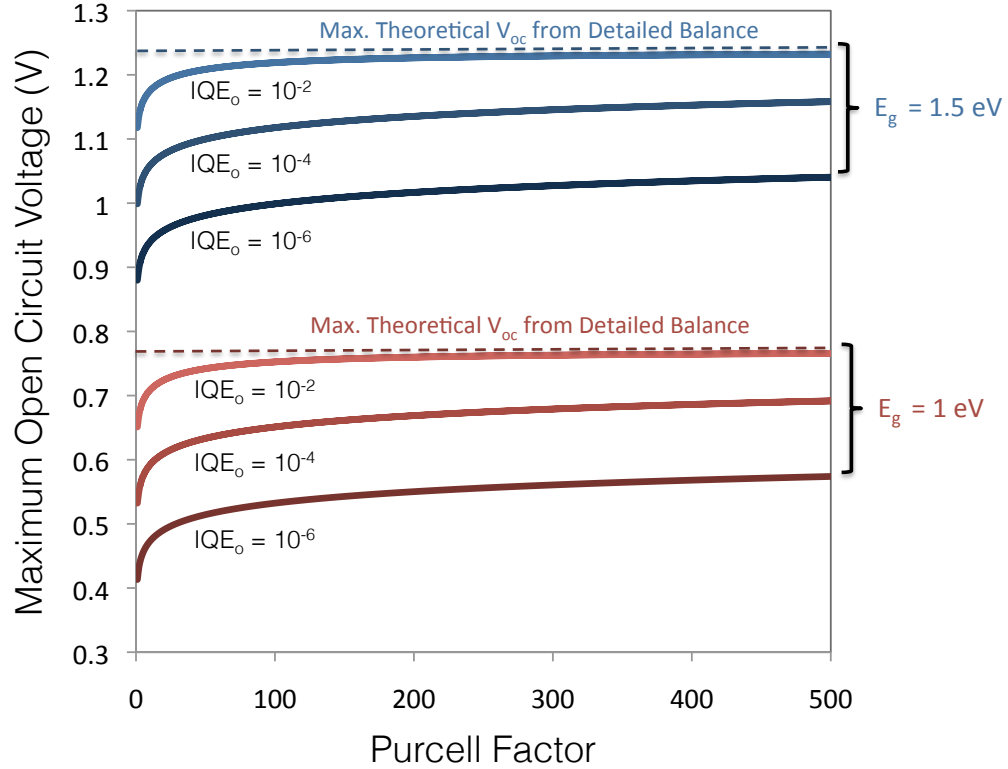


Figure 7.2: Maximum attainable open circuit voltage for different starting materials as a function of radiative emission enhancement, or Purcell Factor.

This plot shows the maximum obtainable open circuit voltages for solar cell material with a given bandgap and initial intrinsic luminescence quantum efficiency. The values for J_{sc} and J_o were obtained in the detailed balance limit (absorptivity = 1) from the following equations:

$$J_{sc} = \int d\Omega \int_{E_g}^{\infty} a(E) \frac{2}{h^3 c^2} \frac{E^2}{e^{\frac{E}{kT_{sun}}} - 1} dE \quad (7.3)$$

$$J_o = \int d\Omega \int_{E_g}^{\infty} a(E) \frac{2}{h^3 c^2} \frac{E^2}{e^{\frac{E}{kT_{cell}}} - 1} dE \quad (7.4)$$

Where Ω is the solid angle subtended by the sun, E_g is the semiconductor bandgap, $a(E)$ is the absorptivity, $T_{sun} = 5780$ K, and $T_{cell} = 300$ K.

The lowest values for V_{oc} at Purcell Factor = 1 are important as they represent the highest obtainable values for open circuit voltage for a given bandgap and intrinsic luminescence quantum efficiency. This value can be regarded as an upper limit, even before any device physics and outcoupling considerations. The only way to exceed this limit is to increase the luminescence quantum efficiency by modifying the solar cells electromagnetic environment and increasing the LDOS. It can be seen that with Purcell Factors of only a few hundred, the obtainable voltages are pushed up to those expected for a material with an intrinsic quantum efficiency 2 orders of magnitude higher than the actual material. This could mean that materials which typically are regarded as having too low quality for solar cell applications could now be considered. Additionally, for relatively high quality materials with intrinsic quantum efficiencies near 1%, their maximum attainable open circuit voltages can now reach the limit imposed by detailed balance, as seen with the saturation of the QE_o curves at high Purcell Factors.

This is a potentially very interesting future research direction to explore and a natural extension to the use of LDOS to increase light absorption that was studied extensively in Chapter 3 of this thesis.

7.3 Photonic Molecules For Light Trapping And Angular Response Engineering

In Chapter 4 we examined the behavior of infinite arrays of dielectric resonators. There has also been extensive work regarding the scattering properties and light trapping potential of single, isolated resonators [11]. An interesting avenue for further exploration is the area between these two extremes, that of a small number of coupled resonators.

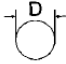
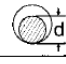
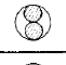
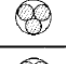
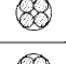
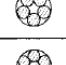
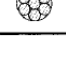


Figure 7.3: Potential configurations for different photonic molecules formed from 4 identical spherical resonators. Each configuration will have a distinct set of coupled resonant modes, radiation patterns and angular responses.

When two resonant optical cavities are placed close enough to each other that the field profiles of their resonant modes overlap, the modes will hybridize, forming what is sometimes called a photonic molecule [81]. The resonant frequencies of the cavities will split, usually into one higher and one lower frequency than the original single cavity resonances (sometimes called bonding and antibonding modes in analogy to molecular orbital theory). There will now be a larger spectral range covered by the coupled resonator system. Additional resonators can then be coupled to the system, adding to the overall resonant bandwidth covered by the interacting resonances. In this way, it should be possible to create photonic molecules with relatively broadband sets of resonances tailored for a specific application. Surprisingly, this concept has not yet been taken advantage of for light trapping in solar cells, where broadband absorption enhancement is a major challenge and highly studied research area. Also, because of their resonant nature, photonic molecules may be a novel route to achieve broadband LDOS enhancements.

Additionally, by coupling optical resonators in different ways, the far field radiation patterns of the system can be tuned [81]. This can potentially be used to tailor the angular response of a solar cell incorporating the coupled resonators, as electromagnetic reciprocity demands that the incoupling or receiving response of an antenna be identical to its radiation pattern. This is a very rich area for research, as there are many different ways to arrange a given number of resonators (see Figure 7.3), with each different configuration potentially having a unique radiation pattern and angular response. The angular response of a solar cell is a very important factor that has received surprisingly little attention in the light trapping literature. Using the engineered radiation patterns of photonic molecules to tailor the angular response of a solar cell would be an original and potentially very insightful direction in this relatively unexplored research area.

Table 1. Control Over the Structure of the Aggregates When Cylindrical Holes Are Used as Templates

Geometric shape of the template	Structures of the cluster	D/d
		1.00-2.00
		2.00-2.15
		2.15-2.41
		2.41-2.70
		2.70-3.00
		3.00-3.30

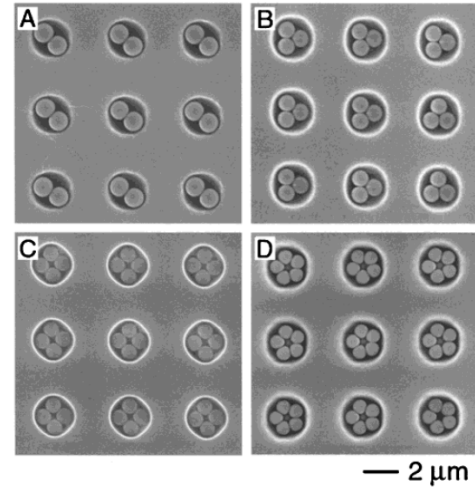


Figure 7.4: [from Yin et al, 2001] [82] Assembly of potential photonic molecules by colloidal self assembly. Trenches are first defined in a photoresist (or potentially an oxide or antireflection layer) and nanospheres of silica (or potentially titania) are assembled via dewetting of an aqueous colloid.

Fabrication of dielectric nanospheres arranged in photonic moleculelike geometries has been demonstrated using colloidal self assembly into photolithographically patterned templates [82], as shown in Figure 7.4. Depending on the geometry of pho-

tolithographically defined trenches, colloidal nanospheres will assemble differently, allowing for a wide range of potential configurations. Many other, more exotic photonic molecules can potentially be fabricated by further tuning the trench geometry. Each configuration corresponds to a different photonic molecule that will have its own distinct optical response. In these previous studies, however, the optical properties of the colloidal assemblies were not investigated.

7.4 Light Absorption Enhancement in Thin Film GaAs

The work of Chapter 6 explored an approach to increase absorption in ultrathin GaAs solar cells. The ultimate goal of this concept is to create a thin film cell that is more efficient than the relatively thick ($\sim 1\text{-}3\text{ }\mu\text{m}$), record GaAs cells. Even though the designs explored in Chapter 6 increased absorption, there was still a significant amount of photons that were not absorbed by the device. In order to approach the record solar cell efficiency, further light trapping enhancement will be needed to bring the J_{sc} close to the record cell's J_{sc} . This could be done with more complicated periodic and quasi-periodic patterns, or more likely by integrating roughened, scattering surfaces to the designs. This could be approached in a way similar to Chapter 5 by adding roughened dielectric surfaces above a thoroughly designed nanopattern, or in a different way that has yet to be extensively explored, such as roughening a dielectric spacer on the rear of the device. It seems likely that the future world record single junction (and possibly multi-junction) solar cells will be thinner versions of the current record cells with added advanced light trapping structures similar to those explored in this thesis.

Appendices

Appendix A

GaAs Epitaxial Liftoff Procedure

1. Start with 1-2 cm² samples, diced from larger wafer.
2. Clean surface by blowing with supercritical CO₂ sno-gun. Immediately dry in N₂ to defrost surface.
3. Sonicate in acetone for 5 min, then sonicate in isopropyl alcohol (IPA) for 5 min. Rinse with DI water, N₂ dry.
4. Dip in hydrochloric acid (HCL) solution (37%, straight from bottle) for 30 s to remove surface oxide to ensure Ohmic contact with deposited metal. Rinse in DI water, N₂ dry.
5. Stick to evaporator sample holder with double sided Cu or carbon tape, device side up. This is to ensure there is no shadowing during metal deposition and a uniform metal layer is deposited over the entire sample surface and edges.
6. Thermally or ebeam deposit 3 nm Ni followed by 100-300 nm Cu with rotation at pressure $< 5 \times 10^{-7}$ Torr.
7. After evaporation, prepare samples for electrodeposition by clipping with alligator clip, being sure there is good contact between the clip and deposited Cu. Attach to the working electrode of the potentiostat.

8. Prepare counter electrode by coiling Cu wire and clipping to the counter electrode alligator clip.
9. Electrodeposit at -20 mA/cm^2 for 5 minutes. Without stopping deposition, change current to -150 mA/cm^2 and deposit for 60 min.
10. Stop deposition, take out samples first and rinse thoroughly in DI water. Take out Cu coil, rinse, and discard. Replace Cu coil with a new coil. Reattach samples being sure to rotate 180 degrees in-plane so that the alligator clips contact the opposite end of the sample. This is just to ensure that the deposited Cu is homogeneous and there isn't a hole in the electrodeposited Cu from where the alligator clips are attached.
11. Electrodeposit for another 60 min at -150 mA/cm^2 .
12. Stop electrodeposition, take out samples first and rinse thoroughly with DI water.
13. There should be significant electrodeposited Cu along the edges of the sample. This has to be removed prior to ELO or it will block access of the etchant to the release layer. Slowly and carefully use a razor blade to cut through the Cu along the corners along the edges of the sample. This should be done along the interface between the top, planar Cu and the 4 edges of the sample. Once the top, planar Cu is isolated from the strips of Cu along the edges, the Cu along the edges can be peeled off or cut and shaved off with the razor blade. If the strips of Cu on the edges that need to be removed are attached to the top, planar Cu at any location, the top, planar Cu may peel off the sample when the edges are removed, which will destroy the rear contact to the device.
14. Cut square of Kapton film (not tape) slightly larger than sample size to use as support during ELO.

15. Add a small amount of trichloroethylene (TCE) / black wax (Apiezon) solution to a beaker or petri dish that has dried black wax in it. Swirl it around for a few minutes and let dry until it is thick and viscous. Once it is viscous and not too thin, apply some of the wax with a swab to the Cu side of sample, being careful not to put too much so that it flows over the edge. Spread the solution around on the sample, covering as much as possible without getting too close to the edge. If at any point the wax solution coats some of the edge of the sample where it would prevent etchant access to the release layer, remove the wax on the edge with a swab dipped in TCE.
16. Press the sample together with the Kapton square, again being careful not to force any wax over the edge of the sample.
17. Bake on a hotplate at 100 °C for ~15 mins to dry out wax by evaporating the solvent.
18. While it is baking, cut up a pipette tip or other small piece of plastic to use as a handle for the sample. Apply a small amount of wax to the piece of pipette tip and stick to the rear of the sample substrate, which should be facing up while it is baking on the hotplate.
19. Take samples off the hotplate and let cool ~5 min.
20. Place samples in 1:1 mixture of 48% HF:EtOH (10% HF solution also works, but takes longer to etch). Leave overnight to etch.
21. Take samples out of HF solution and dip in large beaker of DI water to rinse.
22. Carefully pull on the plastic handle with tweezers while holding down the sample with another set of tweezers on the Kapton film. The substrate with the handle should easily pull right off. If it does not pull off easily, it likely needs more time

to etch, or there could be some wax or Cu connecting the thin device/Kapton to the substrate.

23. Once the substrate is removed from the device layer on Kapton, rinse both thoroughly in DI water and dry with N₂.

Appendix B

Mesa Etching And Contacting Procedure

1. Tape ELO samples on Kapton to a small, square glass slide for rigid support during spin coating.
2. Spin coat PMMA at 3000 rpm for 60 s. Expose to appropriate illumination through appropriate photomask for mesa definition. In Ali's cleanroom, for these spinning conditions, expose for 30 s and develop in MF-319 for 60 s. Rinse thoroughly in DI water. Dry with N_2 .
3. Etch through each of the layers successively using appropriate etchants for each. For the GaAs heterostructure in this thesis, use the following recipe:
 - a) GaAs contact layer (200 nm) - Citric acid: H_2O_2 (10:1) etch for ~ 1 min.
 - b) InAlP window layer (30 nm) 37% HCL etch for ~ 2 -10 s. Will change very quickly from dark to light purple.
 - c) GaAs base and AlGaAs junction/emitter (~ 300 nm) - Citric acid: H_2O_2 (10:1) etch for ~ 2 -5 min. The timing of this etch can vary significantly, especially when it reaches the AlGaAs layers. If it is not progressing, sometimes taking it out and dipping in the 37% HCL solution for a few seconds, rinsing and re-immersing in the citric acid: H_2O_2 can get it going again, presumably because the HCL etches

away oxide buildup.

4. At this point it should be all right to stop the mesa isolation as the etch has proceeded past the junction, though the last 2 layers of the structure can be further etched away by repeating step a), then step b).
5. Following mesa etching, remove the remaining photoresist with acetone and rinse with DI water, N₂ dry.
6. If the samples are no longer on the square glass slides used for support during spincoating, attach to new square glass slides.
7. Spin coat PMMA again at 3000 rpm for 60 s.
8. Perform aligned photolithography to define contact patterns on each of the mesas. Develop, rinse thoroughly with DI water, N₂ dry.
9. Immediately before contact deposition, dip samples again in 37% HCL for 30 s to remove surface oxide.
10. Thermally or ebeam deposit 3 nm Ni followed by 100-300 nm Cu without rotation at pressure $< 5 \times 10^{-7}$ Torr.
11. Let soak in acetone without agitation for ~1 hr. Try to remove resist and metal with acetone from the squeeze bottle instead of sonication if possible. Rinse with IPA, then DI water, N₂ dry.
12. Etch top GaAs contact layer with citric acid:H₂O₂ (10:1) for ~30 s. Be careful not to etch too long as it may cause the contacts to detach. If some of the contacts were partially removed during photoresist liftoff, the inverse contact pattern can be defined with photolithography to protect the contact shape during this etch step.

13. Remove thin sample+Cu film from Kapton by heating at 100 °C and gently pulling off with tweezers once wax is softened.
14. Remove the remaining wax from the back of the Cu film with TCE, being as clean as possible rinsing constantly with TCE from an eyedropper ensuring no TCE/wax solution dries on device side. Once most of the wax has been removed from Cu film, rinse thoroughly with acetone, IPA, and DI water, N₂ dry.
15. Coat glass slide with double sided Cu tape, making as flat a surface as possible.
16. Carefully place the sample, Cu film side down, on the glass slide coated with Cu tape, slowly pressing it down ensuring the sample is as flat as possible and there are no air pockets between the two surfaces.

The sample should now be ready for electrical testing and/or addition of AR coating or nanoimprinting.

Bibliography

- [1] US Energy Information Administration. International energy outlook 2013. Technical report, US Energy Information Administration, 2013.
- [2] World Energy Council. World energy resources: Solar. Technical report, World Energy Council, 2013.
- [3] International Energy Agency. Technology roadmap: Solar photovoltaic energy. Technical report, International Energy Agency, 2010.
- [4] Craig Winneker. Global pv market outlook. Technical report, European Photovoltaic Industry Association, 2013.
- [5] J. D. Joannopoulos, P. R. Villeneuve, and S. H. Fan. Photonic crystals: Putting a new twist on light. *Nature*, 386(6621):143–149, 1997.
- [6] Harry A Atwater. The promise of plasmonics. *Scientific American*, 296(4):56–62, 2007.
- [7] Vladimir M Shalaev. Optical negative-index metamaterials. *Nature photonics*, 1(1):41–48, 2007.
- [8] JL O’Brien, A Furusawa, and J Vuckovic. Photonic quantum technologies. *Nature Photonics*, 3:687 – 695, 2009.

- [9] Ren-Min Ma, Rupert F. Oulton, Volker J. Sorger, and Xiang Zhang. Plasmon lasers: coherent light source at molecular scales. *Laser And Photonics Reviews*, 7(1):1–21, 2013.
- [10] Lukas Novotny and Bert Hecht. Principles of nano-optics, 2006.
- [11] Harry A. Atwater and Albert Polman. Plasmonics for improved photovoltaic devices. *Nature Materials*, 9(3):205–213, 2010.
- [12] Mark L Brongersma, Yi Cui, and Shanhui Fan. Light management for photovoltaics using high-index nanostructures. *Nat Mater*, 13(5):451–60, 2014.
- [13] William Shockley and Hans J. Queisser. Detailed balance limit of efficiency of pn junction solar cells. *Journal of Applied Physics*, 32(3):510–519, 1961.
- [14] Martin A. Green, Keith Emery, Yoshihiro Hishikawa, Wilhelm Warta, and Ewan D. Dunlop. Solar cell efficiency tables (version 43). *Progress in Photovoltaics: Research and Applications*, 22(1):1–9, 2014.
- [15] B.M. Kayes, Hui Nie, R. Twist, S.G. Spruytte, F. Reinhardt, I.C. Kizilyalli, and G.S. Hignashi. 27.6cells under 1 sun illumination. In *Photovoltaic Specialists Conference (PVSC), 2011 37th IEEE*, pages 000004–000008, June 2011.
- [16] et al. Margolis, Robert. Nrel sunshot vision study. Technical report, National Renewable Energy Laboratory, 2012.
- [17] A. Yariv and P. Yeh. *Photonics: Optical Electronics in Modern Communications*. The Oxford Series in Electrical and Computer Engineering. Oxford University Press, Incorporated, 2007.
- [18] Barnes W. L. Fluorescence near interfaces: the role of photonic mode density. *J. Mod. Opt.*, 45:661, 1998.

- [19] Yablonovitch E. Statistical ray optics. *J. Opt. Soc. Am.*, 72:899, 1982.
- [20] Erik Garnett and Peidong Yang. Light trapping in silicon nanowire solar cells. *Nano Letters*, 10(3):1082–1087, 2010.
- [21] Michael D. Kelzenberg, Shannon W. Boettcher, Jan A. Petykiewicz, Daniel B. Turner-Evans, Morgan C. Putnam, Emily L. Warren, Joshua M. Spurgeon, Ryan M. Briggs, Nathan S. Lewis, and Harry A. Atwater. Enhanced absorption and carrier collection in si wire arrays for photovoltaic applications. *Nature Materials*, 9(3):239–244, 2010.
- [22] Han S. E. Toward the lambertian limit of light trapping in thin nanostructured silicon solar cells. *Nano Lett.*, 10:4692, 2010.
- [23] Chutinan A. High-efficiency photonic crystal solar cell architecture. *Opt. Express*, 17:8871, 2009.
- [24] Peter N. Saeta, Vivian E. Ferry, Domenico Pacifici, Jeremy N. Munday, and Harry A. Atwater. How much can guided modes enhance absorption in thin solar cells? *Optics Express*, 17(23):20975–20990, 2009.
- [25] Yu Z. F. Fundamental limit of nanophotonic light trapping in solar cells. *Proc. Natl. Acad. Sci. U. S. A.*, 107:17491, 2010.
- [26] Green M. A. Enhanced evanescent mode light trapping in organic solar cells and other low index optoelectronic devices. *Prog. Photovoltaics*, 2011.
- [27] Zhu J. Nanostructured photon management for high performance solar cells. *Mater. Sci. Eng. R*, 70:330, 2010.
- [28] Gee J. M. Optically enhanced absorption in thin silicon layers using photonic crystals. *29th IEEE PVSC Proc.*, page 150, 2002.

- [29] Sheng P. Wavelength-selective absorption enhancement in thin-film solar cells. *Appl. Phys. Lett.*, 43:579, 1983.
- [30] Stuart H. R. Thermodynamic limit to light trapping in thin planar structures. *J. Opt. Soc. Am. A*, 14:3001, 1997.
- [31] I. M. Bassett. Limits to concentration by passive means. *Phys. Rev. Lett.*, 54:2014–2017, May 1985.
- [32] Ford G. W. Electromagnetic-interactions of molecules with metal-surfaces. *Phys. Rep.*, 113:195, 1984.
- [33] Almeida V. R. Guiding and confining light in void nanostructure. *Opt. Lett.*, 29:1209, 2004.
- [34] Yablonovitch E. Inhibited spontaneous emission in solid-state physics and electronics. *Phys. Rev. Lett.*, 58:2059, 1987.
- [35] E. Yablonovitch, D. L. Allara, C. C. Chang, T. Gmitter, and T. B. Bright. Unusually low surface-recombination velocity on silicon and germanium surfaces. *Phys. Rev. Lett.*, 57:249–252, Jul 1986.
- [36] Barnett S. Sum rule for modified spontaneous emission rates. *Phys. Rev. Lett.*, 77:2444, 1996.
- [37] Scheel S. Sum rule for local densities of states in absorbing dielectrics. *Phys. Rev. A*, 78:013841, 2008.
- [38] Dayu Zhou and Rana Biswas. Photonic crystal enhanced light-trapping in thin film solar cells. *Journal of Applied Physics*, 103(9):–, 2008.
- [39] E. A. Schiff. Thermodynamic limit to photonic-plasmonic light-trapping in thin films on metals. *Journal of Applied Physics*, 110(10):–, 2011.

- [40] Dennis M. Callahan, Jeremy N. Munday, and Harry A. Atwater. Solar cell light trapping beyond the ray optic limit. *Nano Letters*, 12(1):214–218, 2012.
- [41] T. Tiedje, E. Yablonovitch, G.D. Cody, and B.G. Brooks. Limiting efficiency of silicon solar cells. *Electron Devices, IEEE Transactions on*, 31(5):711–716, May 1984.
- [42] Matthias Kroll, Stephan Fahr, Christian Helgert, Carsten Rockstuhl, Falk Lederer, and Thomas Pertsch. Employing dielectric diffractive structures in solar cells - a numerical study. *Physica Status Solidi a-Applications and Materials Science*, 205(12):2777–2795, 2008.
- [43] Y. N. Xia, B. Gates, Y. D. Yin, and Y. Lu. Monodispersed colloidal spheres: Old materials with new applications. *Advanced Materials*, 12(10):693–713, 2000.
- [44] A. Yariv, Y. Xu, R. K. Lee, and A. Scherer. Coupled-resonator optical waveguide: a proposal and analysis. *Optics Letters*, 24(11):711–713, 1999.
- [45] R. M. Cole, Y. Sugawara, J. J. Baumberg, S. Mahajan, M. Abdelsalam, and P. N. Bartlett. Easily coupled whispering gallery plasmons in dielectric nanospheres embedded in gold films. *Physical Review Letters*, 97(13), 2006.
- [46] Xindi Yu, Lei Shi, Dezhuan Han, Jian Zi, and Paul V. Braun. High quality factor metallodielectric hybrid plasmonic-photonic crystals. *Advanced Functional Materials*, 20(12):1910–1916, 2010.
- [47] Vivian E. Ferry, Marc A. Verschuuren, Hongbo B. T. Li, Ewold Verhagen, Robert J. Walters, Ruud E. I. Schropp, Harry A. Atwater, and Albert Polman. Light trapping in ultrathin plasmonic solar cells. *Optics Express*, 18(13):A237–A245, 2010.

- [48] Vivian E. Ferry, Jeremy N. Munday, and Harry A. Atwater. Design considerations for plasmonic photovoltaics. *Advanced Materials*, 22(43):4794–4808, 2010.
- [49] Arthur D. Yaghjian. Internal energy, q-energy, poynting’s theorem, and the stress dyadic in dispersive material. *Ieee Transactions on Antennas and Propagation*, 55(6):1495–1505, 2007. 1.
- [50] Z. G. Chen, A. Taflove, and V. Backman. Highly efficient optical coupling and transport phenomena in chains of dielectric microspheres. *Optics Letters*, 31(3):389–391, 2006.
- [51] Y. D. Yin, Y. Lu, B. Gates, and Y. N. Xia. Template-assisted self-assembly: A practical route to complex aggregates of monodispersed colloids with well-defined sizes, shapes, and structures. *Journal of the American Chemical Society*, 123(36):8718–8729, 2001.
- [52] V. Kitaev and G. A. Ozin. Self-assembled surface patterns of binary colloidal crystals. *Advanced Materials*, 15(1):75–+, 2003.
- [53] Jonathan Grandidier, Dennis M. Callahan, Jeremy N. Munday, and Harry A. Atwater. Light absorption enhancement in thin-film solar cells using whispering gallery modes in dielectric nanospheres. *Advanced Materials*, 23(10):1272–1276, 2011.
- [54] C. H. Henry. Limiting efficiencies of ideal single and multiple energy-gap terrestrial solar-cells. *Journal of Applied Physics*, 51(8):4494–4500, 1980.
- [55] Keisuke Nakayama, Katsuaki Tanabe, and Harry A. Atwater. Plasmonic nanoparticle enhanced light absorption in gaas solar cells. *Applied Physics Letters*, 93(12), 2008.

- [56] C. Colombo, M. Hei, M. Grtzel, and A. Fontcuberta i Morral. Gallium arsenide p-i-n radial structures for photovoltaic applications. *Applied Physics Letters*, 94(17):–, 2009.
- [57] Jia Zhu, Ching-Mei Hsu, Zongfu Yu, Shanhui Fan, and Yi Cui. Nanodome solar cells with efficient light management and self-cleaning. *Nano Letters*, 10(6):1979–1984, 2010.
- [58] Peter Bermel, Chiyan Luo, Lirong Zeng, Lionel C. Kimerling, and John D. Joannopoulos. Improving thin-film crystalline silicon solar cell efficiencies with photonic crystals. *Optics Express*, 15(25):16986–17000, 2007.
- [59] Alongkarn Chutinan and Sajeev John. Light trapping and absorption optimization in certain thin-film photonic crystal architectures. *Phys. Rev. A*, 78:023825, Aug 2008.
- [60] Corsin Battaglia, Ching-Mei Hsu, Karin Sderstrm, Jordi Escarr, Franz-Josef Haug, Mathieu Charrre, Mathieu Boccard, Matthieu Despeisse, Duncan T. L. Alexander, Marco Cantoni, Yi Cui, and Christophe Ballif. Light trapping in solar cells: Can periodic beat random? *ACS Nano*, 6(3):2790–2797, 2012.
- [61] Vivian E. Ferry, Marc A. Verschuuren, M. Claire van Lare, Ruud E. I. Schropp, Harry A. Atwater, and Albert Polman. Optimized spatial correlations for broadband light trapping nanopatterns in high efficiency ultrathin film a-si:h solar cells. *Nano Letters*, 11(10):4239–4245, 2011.
- [62] M. Peters, K. Forberich, C. Battaglia, A. G. Aberle, and B. Blsi. Comparison of periodic and random structures for scattering in thin-film microcrystalline silicon solar cells. *Proc. SPIE*, 8438:84380F–84380F–9, 2012.

- [63] Chenxi Lin and Michelle L. Povinelli. Optimal design of aperiodic, vertical silicon nanowire structures for photovoltaics. *Opt. Express*, 19(S5):A1148–A1154, Sep 2011.
- [64] Chenxi Lin, Ningfeng Huang, and Michelle L. Povinelli. Effect of aperiodicity on the broadband reflection of silicon nanorod structures for photovoltaics. *Opt. Express*, 20(S1):A125–A132, Jan 2012.
- [65] Kevin Vynck, Matteo Burrelli, Francesco Riboli, and Diederik S. Wiersma. Photon management in two-dimensional disordered media. *Nature Materials*, 11(12):1017–1022, 2012.
- [66] Hatice Altug and Jelena Vukovi. Two-dimensional coupled photonic crystal resonator arrays. *Applied Physics Letters*, 84(2):161–163, 2004.
- [67] Hatice Altug, Dirk Englund, and Jelena Vuckovic. Ultrafast photonic crystal nanocavity laser. *Nat Phys*, 2(7):484–488, 2006.
- [68] Jing Ma, Luis Javier Martínez, and Michelle L. Povinelli. Optical trapping via guided resonance modes in a slot-suzuki-phase photonic crystal lattice. *Opt. Express*, 20(6):6816–6824, Mar 2012.
- [69] Ken Xingze Wang, Zongfu Yu, Victor Liu, Yi Cui, and Shanhui Fan. Absorption enhancement in ultrathin crystalline silicon solar cells with antireflection and light-trapping nanocone gratings. *Nano Letters*, 12(3):1616–1619, 2012.
- [70] Makoto Konagai, Mitsunori Sugimoto, and Kiyoshi Takahashi. High efficiency gaas thin film solar cells by peeled film technology. *Journal of Crystal Growth*, 45(0):277 – 280, 1978.

- [71] Eli Yablonovitch, T. Gmitter, J. P. Harbison, and R. Bhat. Extreme selectivity in the liftoff of epitaxial gaas films. *Applied Physics Letters*, 51(26):2222–2224, 1987.
- [72] O. D. Miller, E. Yablonovitch, and S. R. Kurtz. Strong internal and external luminescence as solar cells approach the shockley queisser limit. *Photovoltaics, IEEE Journal of*, 2(3):303–311, July 2012.
- [73] Marc A Verschuuren. *Substrate Conformal Imprint Lithography for Nanophotonics*. PhD thesis, 2009.
- [74] V. Ganapati, O.D. Miller, and E. Yablonovitch. Light trapping textures designed by electromagnetic optimization for subwavelength thick solar cells. *Photovoltaics, IEEE Journal of*, 4(1):175–182, Jan 2014.
- [75] Luca Sapienza, Henri Thyrestrup, Sren Stobbe, Pedro David Garcia, Stephan Smolka, and Peter Lodahl. Cavity quantum electrodynamics with anderson-localized modes. *Science*, 327(5971):1352–1355, 2010.
- [76] Mordechai Segev, Yaron Silberberg, and Demetrios N. Christodoulides. Anderson localization of light. *Nature Photonics*, 7(3):197–204, March 2013.
- [77] G. Smestad and H. Ries. Luminescence and current-voltage characteristics of solar cells and optoelectronic devices. *Solar Energy Materials and Solar Cells*, 25(12):51 – 71, 1992.
- [78] Uwe Rau. Reciprocity relation between photovoltaic quantum efficiency and electroluminescent emission of solar cells. *Phys. Rev. B*, 76:085303, Aug 2007.
- [79] M. Agio. Nano-optics: The purcell factor of nanoresonators. *Nature Photonics*, (9):674675, 2013.

- [80] Palash Bharadwaj and Lukas Novotny. Spectral dependence of single molecule fluorescence enhancement. *Opt. Express*, 15(21):14266–14274, Oct 2007.
- [81] SvetlanaV. Boriskina. Photonic molecules and spectral engineering. In Ioannis Chremmos, Otto Schwelb, and Nikolaos Uzunoglu, editors, *Photonic Microresonator Research and Applications*, volume 156 of *Springer Series in Optical Sciences*, pages 393–421. Springer US, 2010.
- [82] Yadong Yin, Yu Lu, Byron Gates, and Younan Xia. Template-assisted self-assembly: a practical route to complex aggregates of monodispersed colloids with well-defined sizes, shapes, and structures. *Journal of the American Chemical Society*, 123(36):8718–8729, 2001. PMID: 11535076.